Zagazig University
Faculty of Engineering
Construction Eng. & Utilities Dep.

GNSS Radio Occultation for Studying Troposphere Delay in Egypt

By

Ibrahim Fouad Ibrahim Ahmed

Assistant Lecturer, Construction Eng. and Utilities Department
Faculty of Eng., Zagazig University

A Thesis

Submitted in Partial Fulfillment of the Requirements to Faculty of Engineering, Zagazig University for the Degree of PhD in Construction Eng. and Utilities

Advisory Committee

Prof. Dr. Gamal El-Fiky
Prof. of Surveying and Geodesy,
Construction Eng. and Utilities Department,
Faculty of Eng., Zagazig University

Prof. Dr. Ashraf El-Kutb Mousa
Prof. of Surveying and Geodesy,
National Research Institute of Astronomy and Geophysics, Helwan, Cairo

Dr. Mohamed Amin Abd-Elfatah
Lecturer, Construction Eng. and Utilities Dept.
Faculty of Eng., Zagazig University

2022

Table of Contents

List of Tables III
List of Figures V
List of Abbreviations VII
List of Symbols XI
Abstract XIII
Acknowledgements XVII

Chapter 1 : Introduction 1
1.1 Concept of GNSS-RO 1
1.2 RS Method for Atmosphere Profiling 7
1.3 Statement of the Problem 8
1.4 Research Methodology 9
1.5 Research Objectives 10
1.6 Thesis Organization 10
1.7 Research Outlines 11

Chapter 2 : Data Acquisition 13
2.1 RO and RS Profiles Comparison Previous Studies 14
2.2 ZHD and ZWD Models Previous Studies 14
2.3 RO Data Used in Analysis 15
2.4 RS Data Used in Analysis 24
2.5 GPS Observations 27
2.6 ECMWF Model Data 28

Chapter 3 : Data Analysis 31
3.1 Abel Transform Inversion 31
3.2 Analysis of the Differences between RO and RS Profiles 34
3.3 Zenith Delay Calculation 36
3.4 Differences in ZPD between RO, RS and GPS-PPP 37

3.4.1 RO ZPD 37
3.4.2 RS ZPD 38
3.4.3 GPS CSRS-PPP ZPD 39
3.5 ZPD Relations with Time and Other Meteorological Parameters 44

Chapter 4 : Results and Discussion 47
4.1 RO-RS Single Profile Comparison 47
4.2 RO-RS Data Difference Analysis 51
4.3 LEO Satellites Difference Analysis 57
4.4 Upper Air Stations Difference Analysis 59
4.5 ZPD Differences between RO, RS and PPP Data 60
4.6 ZPD Differences between RO and PPP Data 64
4.7 Relation between ZPD and Meteorological Parameters 66
4.8 Relation between ZPD and Latitude and Longitude 71
4.9 Delay Time Series 74
4.10 ZHD and ZWD Models 77
4.11 ZPD and Meteorological Parameters Spatial Distribution Maps 78

Chapter 5 : Conclusions and Recommendations 83
5.1 Summary 83
5.2 Conclusions 85
5.3 Recommendations 88

References 91

الملخص العربي ..... أ

List of Tables

Table (2.1): Upper air stations number, latitude, and longitude.....26

Table (4.1): Mean absolute difference and St. Dev. for the three RO-RS check points.....49

Table (4.2): T-test results for the three RO-RS check points.....50

Table (4.3): Mean absolute difference, SD, and number of check points for each group.....54

Table (4.4): Mean absolute difference, RMS, SD, and number of check points for each group.....56

Table (4.5): ZPD differences and T-test results for RS, PPP, and RO data.....63

Table (4.6): ZPD differences and T-test results for PPP, and RO data.....66

List of Figures

Fig. (1.1): Demonstration of COSMIC Mission 2
Fig. (1.2): Concept of atmosphere profiling using the GPS radio occultation technique 5
Fig. (2.1): Number of Observations for Each LEO satellite.....21
Fig. (2.2): Number of observations for each LEO satellite in each year 21
Fig. (2.3): Distribution of ROE over Egypt in 2011 23
Fig. (2.4): Distribution of ROE over Egypt in 2015 23
Fig. (2.5): Distribution of ROE over Egypt in 2011-2021 24
Fig. (2.6): Distribution of RS stations in Egypt 27
Fig. (3.1): The geometry of an RO measurement with a receiver on board a LEO satellite 32
Fig. (3.2): Research methodology flow chart 35
Fig. (3.3): Distribution of RS stations and ROEs in Egypt on JD=2456940 36
Fig. (4.1): Comparison profiles between RO and RS data. 48
Fig. (4.2): RO-RS observations difference. 52
Fig. (4.3): RO-RS observations RMS and mean absolute Difference 55
Fig. (4.4): RO-LEO mission observations difference 58
Fig. (4.5): RS stations observations difference 59
Fig. (4.6): ZHD for RS, RO, and PPP 61
Fig. (4.7): ZWD for RS, RO, and PPP 62
Fig. (4.8): ZHD for RO and PPP 64
Fig. (4.9): ZWD for RO and PPP 65
Fig. (4.10): Surface Pressure with ZHD 67
Fig. (4.11): Surface Pressure with ZWD 68
Fig. (4.12): Surface temperature with ZHD 69
Fig. (4.13): Surface temperature with ZWD 70
Fig. (4.14): Surface WVP with ZHD 70
Fig. (4.15): Surface WVP with ZWD 71

Fig. (4.16): ZHD change with latitude 72
Fig. (4.17): ZWD change with latitude 72
Fig. (4.18): ZHD change with longitude 73
Fig. (4.19): ZWD change with longitude 74
Fig. (4.20): ZHD time series through the study period 75
Fig. (4.21): ZHD time series through the years 75
Fig. (4.22): ZWD time series through the study period 76
Fig. (4.23): ZWD time series through the years 76
Fig. (4.24): ZHD distribution on Egypt map 79
Fig. (4.25): ZWD distribution on Egypt map 80
Fig. (4.26): Pressure distribution on Egypt map 81
Fig. (4.27): WVP distribution on Egypt map 81
Fig. (4.28): Temperature distribution on Egypt map 82

List of Abbreviations

Abbreviations	Meanings
ALAM	Marsa Alam station.
APPS	Automatic Precise Point Positioning.
ASUT	Assiut station.
ASWN	Aswan station.
BMBF	German Ministry of Education and Science.
C/NOFS	Communication/Navigation Outage Forecast System.
CDAAC	Data Analysis and Archive Center.
CNES	Centre National d'Etudes Spatiales or the French Space Agency.
CONAE	Argentine Commission on Space Activities.
CORS	Continuously Operating Reference Stations.
COSMIC	Constellation Observing System for Meteorology, Ionosphere and Climate.
CSRS	Canadian Spatial Reference System.
DCB	Differential Code Biases.
DLR	German Aerospace Center.
DMIT	Damietta station.
DOD	U.S. Department of Defense.
DOY	Day Of Year.
ECMWF	European Centre for Medium-Range Weather Forecasts.
EDP	Electron Density Profile.
ESA	European Space Agency.
EUMETSAT	European Organization for the Exploitation of Meteorological Satellites.
GAPS	Online PPP solution by the University of New Brunswick.
GIM	Global Ionospheric Maps.
GIS	Geographical Information Systems.
GMF	Global Mapping Function.
GNSS	Global Navigation Satellite Systems.
GPS	Global Positioning System.

GPS/MET	Global Positioning System/Meteorology.
GRACE	The Gravity Recovery and Climate Experiment.
Hisdesat	Spanish company provides satellite services to government organizations focused on defense, safety, intelligence, and external affairs.
HURG	Hurghada station.
IGRA	Integrated Global Radiosonde Archive.
IGS	International GNSS Services.
ITRF	International Terrestrial Reference Frame.
IWV	Integrated Water Vapor.
JD	Julian Date.
JPL	Jet Propulsion Laboratory.
KOMPSAT-5	Korean Multi-purpose Satellite 5.
LEO	Low Earth Orbiter.
Mb	millibar.
MetOp	Meteorological Operational satellite
MF	Mapping Function.
MNSR	Mansoura station.
MRSA	Marsa Matrouh station.
mh(E)	Hydrostatic Mapping Function.
mw(E)	Wet Mapping Function.
NASA	National Aeronautics and Space Administration.
NetCDF	Network Common Data Form.
NMF	New Mapping Function.
NOAA	National Oceanic and Atmospheric Administration.
NRIAG	National Research Institute of Astronomy and Geophysics.
NWP	Numerical Weather Prediction.
PHLW	Helwan station.
PPP	Precise Point Positioning.
RINEX	Receiver Independent Exchange.
RO	Radio Occultation.
ROE	Radio Occultation Event.
RS	Radiosonde.
SAR	Synthetic Aperture Radar.

SNR	Signal to Noise Ratio.
SUEZ	Suez station.
TEC	Total Electron Content.
U.S.	United States.
UCAR	University Corporation for Atmospheric Research
UTM	Universal Transverse Mercator.
VMF	Vienna Mapping Function.
WVP	Water Vapor Pressure.
ZHD	Zenith Hydrostatic Delay.
ZPD	Zenith Path Delay.
ZTD	Zenith Total Delay.
ZWD	Zenith Wet Delay.

List of Symbols

Symbols	Meanings
α	Bending Angel.
ϕ	Angel between Ray and Radii Vectors.
Δ^{PD}	Total Troposphere Signal Delay.
λ	Longitude Angel.
$\boldsymbol{a}$	Impact Parameter.
$\boldsymbol{D_{pd}}$	Dew Point Depression.
$\boldsymbol{e}$	Water Vapor Pressure.
$\boldsymbol{n}$	Refractive Index.
$\boldsymbol{N}$	Refractivity.
$\boldsymbol{N_{dry}}$	Dry Refractivity.
$\boldsymbol{N_{wet}}$	Wet Refractivity.
$\boldsymbol{P_d}$	Dry Atmosphere Pressure.
$\boldsymbol{R}$	Radius of Symmetric Sphere.
$\boldsymbol{r}$	Receiver.
$\boldsymbol{S_4}$	Amplitude Scintillation.
$\boldsymbol{T}$	Temperature.
$\boldsymbol{T_{dp}}$	Dew Point Temperature.
$\boldsymbol{w}$	Satellite (Transmitter).

Abstract

Improving position determination using Global Navigation Satellite Systems (GNSS) is an important research field in civil engineering. Position accuracy depends mainly on GNSS errors reduction. Troposphere signal delay is a paramount error as there is no way to vanish it utterly. Troposphere signal delay accuracy relies on meteorological parameters accuracy. Also, ameliorate the troposphere delay model positively affects positioning accuracy.

Radio occultation (RO) method defines atmosphere accurately. Data availability for all Low Earth Orbiter (LEO) satellites eases method applicability. Besides product accuracy and data availability, RO data gives an adequate number with well spatial and temporal random distribution. Pressure, temperature Water Vapor Pressure (WVP) and refractivity are parameters we care about to hook up our research objectives.

RO meteorological data are downloaded using University Corporation for Atmospheric Research (UCAR) web site. UCAR web site offer data for all LEO satellites in Network Common Data Form (NetCDF) format. NetCDF format lets outputting data in several dimensions which ease dealing with it. Pressure, temperature, WVP and refractivity are downloaded for the period from 2010 to 2020 in Egypt. Radiosonde (RS) data are downloaded for the same period and region in NetCDF format to compare it with the RO data and the resulted signal delay. Also, Global Positioning System (GPS) observations trough the same period are used in signal delay comparison.

Bash scripts and FORTRAN subroutines are used in RO and RS data reading, processing and analysis. Canadian Spatial Reference System Precise Point Positioning (CSRS-PPP) method is used in GPS data processing to get Zenith Path

Delay (ZPD). RO and RS meteorological parameters are compared to insure the validity of RO and RS data integration. RO and RS ZPD are compared to each other and to the PPP processing results to validate the RO data in ZPD calculation.

At first, Difference values between RO and RS profiles are analyzed to assess the integration applicability between them for Egypt. Compared profiles which have altitudes ranged from 3.0 to 25 km are used in analysis of RO and RS data. According to single profile comparison and T-test, all difference values are not significant except for WVP.

Pressure, temperature, WVP and refractivity mean difference values are estimated to be 0.6 mb, 0.79 deg, 0.1 mb, 0.48 with relative error of 0.3%, 1.7%, 62% and 0.7%, respectively. However, refractivity values are significantly affected by small difference in the other parameters as changing pressure, temperature or WVP by small values, changes the refractivity significantly. According to LEO satellites difference analysis, GRACE2 gave maximum difference values of 4.3±0.15 mb in pressure and 7.8±0.35 deg in temperature with a relative error of 1.96% and 16.26% for them, respectively. COSMIC 3 & 6 and GRACE1 gave minimum difference values and the other missions gave small difference values but all of these differences are considered statistically significant. Satellite signal tracking and processing in LEO receiver and the mathematical inversion are key parameters in LEO satellite error disparity. According to upper air stations difference analysis, station Benina gave big difference values of 5.1±0.23 mb in pressure and 6±0.3 deg in temperature with a relative error of 2.3% and 12.58% for them, respectively. Stations Mersa Matruh, Athalasa and South of Valley gave a smaller difference value, and the other stations gave small difference values. However, all of stations differences are statistically significant.

Zenith Hydrostatic Delay (ZHD) and Zenith Wet Delay (ZWD) are estimated based on RO and RS profiles and compared with each other and with PPP processing results. ZHD and ZWD resulted from the different techniques are compatible with each other except for the RS and PPP ZHD.

Relations between each of ZHD and ZWD and the meteorological parameters, spatial and temporal changes are studied. ZHD is impacted by pressure, temperature, and longitude change. ZWD is impacted by pressure, temperature, WVP and Day of Year (DOY). A statistical model based on multi-linear regression is constructed for each of ZPD components. The models average errors in ZHD and ZWD estimated values, based on out-layer observations equal to 20% of observations not involved in model creation, are 1.0 cm and 3.7 cm, respectively and these differences are considered good enough comparing by the other models.

Acknowledgements

First and foremost, I would like to thank Allah for all of his donations and grants. All that I have is due to his grace and I would glorify him for all his blessings.

Sincere and profound appreciation is expressed to Prof. Dr. Gamal El-Fiky for his continues full support, invaluable advice, numerous suggestions and reliable confidence. Sincere and profound appreciation is expressed to Prof. Dr. Ashraf Mousa for putted his trusts in me, guidance, invaluable advice and numerous suggestions. Sincere and profound appreciation is expressed to Dr. Mohamed Amin, for invaluable advice and numerous suggestions during the preparation of the present work. Their cooperation and understanding deserve unbounded appreciation. It was my great pleasure working under their supervision.

I would like also thank to my teachers, Dr. Ibrahim Salama, Mohamed El-Ashquer, Heba Samir, my colleagues, Eng. Ahmed Gamal, Reham Nagib, Ahmed Nabil, Ragab, Ahmed Saadon, Mohamed Ashraf, Ibrahim Bakry and Ahmed Salah for their encouragement as study companions and Mr mamdouh El-Nadi and Ms. Nemat for their continues aid.

Very special thanks go to my family especially my lovely mother, who always wished to see this day, my father, who always encourages me, my sisters Ghada and Nada, my brother Ahmed, my nephew Ahmed and Yousif and my niece Reem, Mariam, Farida and Khadiga.

Last but not least, an endless thank goes to my wife Nahla for her support in pursuing my goals, her encouragement, and her patience with me during the hard

days and also to my lovely son Yahia and my daughter Zahra for the lovely smiles that could mitigate any sort of tiredness. The helpful suggestions of many others who have somehow contributed to the successful completion of this work are gratefully acknowledged.

CHAPTER 1

INTRODUCTION

Chapter 1 : Introduction

Accurate atmosphere parameters measuring became one of the most leading fields of research in Earth sciences. Owning an accurate and easy system to measure atmosphere parameters is an important matter as the traditional methods are not coping with the modern era requirements. The space-based Global Navigation Satellite Systems Radio Occultation (GNSS-RO) technique is a promising tool for monitoring the Earth's atmosphere and ionosphere (e.g., Kursinski et al., 1997). RO method depends on receiving GNSS signal by an occultation antenna on-board a Low Earth Orbiter (LEO) satellite. The signal delays due to passing through any planet (e.g., Earth) atmosphere (e.g., Ahmed et al., 2022). Signal delay analysis enables producing a complete atmosphere model in a certain point that called "Radio Occultation Event" (ROE) or an observation on the Earth surface.

To understand the present research procedures, the two main methods in atmosphere identification, RO, and RadioSonde (RS), should be elucidated. The following sections will give a brief background about the RO and RS methods then the research methodology, objectives and outlines.

1.1 Concept of GNSS-RO

The story of RO began at the dawn of interplanetary space exploration in the 1960s when a team of scientists from Stanford University and the Jet Propulsion Laboratory (JPL) used the Mariner 3 and 4 satellites to probe the atmosphere of Mars using the RO technique. In 1990s, when the constellation of Global Position System (GPS) was nearly accomplished, it was realized by the community that RO technique could

be used to sound the Earth's atmosphere based on the GPS signals. This concept was soon after demonstrated by the proof-of-concept GPS/Meteorology (GPS/MET) experiment in 1995. This led to several successful additional missions hereafter, including CHAMP, GRACE, SAC-C/D, COSMIC, C/NOFS, MetOp-A/B, TerraSAR-X/TanDEMX (Anthes, 2011). Of these missions, COSMIC was the first constellation of satellites dedicated primarily to RO and delivering RO data in near real-time (Rocken et al., 2000). Fig. (1.1) shows the demonstration of COSMIC constellations. Please note that only 2 of 6 LEOs are shown in the picture (e.g., Yue et al., 2013).

Fig. (1.1): Demonstration of COSMIC Satellites and Orbits (UCAR, 2022).

When the GNSS signals passing through the lower atmosphere, the GNSS ray will significantly bend due to the dense water vapor and neutral

gas. Using the bending information, the profiles of neutral density, temperature, and water vapor can be derived under certain assumptions (e.g., Ghoniem et al., 2020). These parameters have very high precision and accuracy and have been widely used in numerical weather prediction (NWP), climate, and meteorology studies. When the GNSS signals transferring through the ionosphere, the bending effects due to ionized ions are usually hard accurately derived and can be ignored using frequency combinations. Since the effects of ionized ions on the radio wave are frequency dependent, the Total Electron Content (TEC) along the GNSS ray can be calculated by dual-frequency receiver (Yue et al., 2011). Under some certain assumptions, the Electron Density Profile (EDP) along the tangent points could be retrieved. In addition, the irregularities in the ionosphere could disturb the amplitude of the signals. By analyzing the Signal-to-Noise Ratio (SNR) of the RO signal, the parameters characterizing the ionospheric irregularities including sporadic E layer, amplitude scintillation (S4) can be derived. In comparison with other LEO based remote sensing method; RO has the following advantages (e.g., Yue et al., 2013)

- Limb sounding geometry complementary to ground and space nadir viewing instruments.
- Global 3-D atmospheric weather coverage from 40 km to sea level surface.
- Long term stability.
- High accuracy temperature measurement (equivalent to <1 K; average accuracy <0.1 K).
- High precision temperature measurement (0.02-0.05 K).
- High vertical resolution (0.1 km surface - 0.1 km tropopause).
- All weather-minimally affected by aerosols, clouds, or precipitation.

- Independent height and pressure.
- Independent of RS calibration.
- No instrument drifts.
- No satellite-to-satellite bias.
- A typical RO sounding showing very sharp tropopause.
- No other instrument from space provides such high vertical resolution profile.

RO technique uses opportunistic GNSS signals to sound the atmosphere. The signal trajectory, travelling from GNSS satellites to LEO, is bent due to the index of refraction gradients of the atmosphere. Such bending can be inferred using the phase derivative observable (Doppler shift) obtained by dedicated receivers in the LEOs (e.g., Padullés et al., 2018).

Any electromagnetic signal is refracted when passing through the atmosphere. Refractivity index depends on the density and water vapor of the neutral medium and the TEC of the ionized one. Thus, measurements of refraction will contain information on the density in the neutral atmosphere (and hence temperature and water vapor) and the electron density along the path (e.g., Kursinski et al., 1997). A series of electromagnetic wave rays at different heights (Fig. 1.2) yields observations containing information on the atmosphere profile of refractivity. If the tangent heights lay within the neutral atmosphere, the refractivity can be converted to a profile of temperature and/or water vapor (e.g., Eyre, 1994). On the other hand, if tangent heights lay within the ionized one, the refractivity profile is converted to an electron density profile (e.g., Ghoniem et al., 2017).

At radio frequencies, it is not possible to make direct geometric

measurements of the refracted angle precisely. However, if the transmitter and receiver are in relative motion, the refraction introduces a change in the Doppler shift of the received signal, and this can be related to the refracted angle. Space-based RO measurements using GNSS receivers on a LEO satellite provides accurate atmospheric refractivity profiles (e.g., Kursinski et al., 1997).

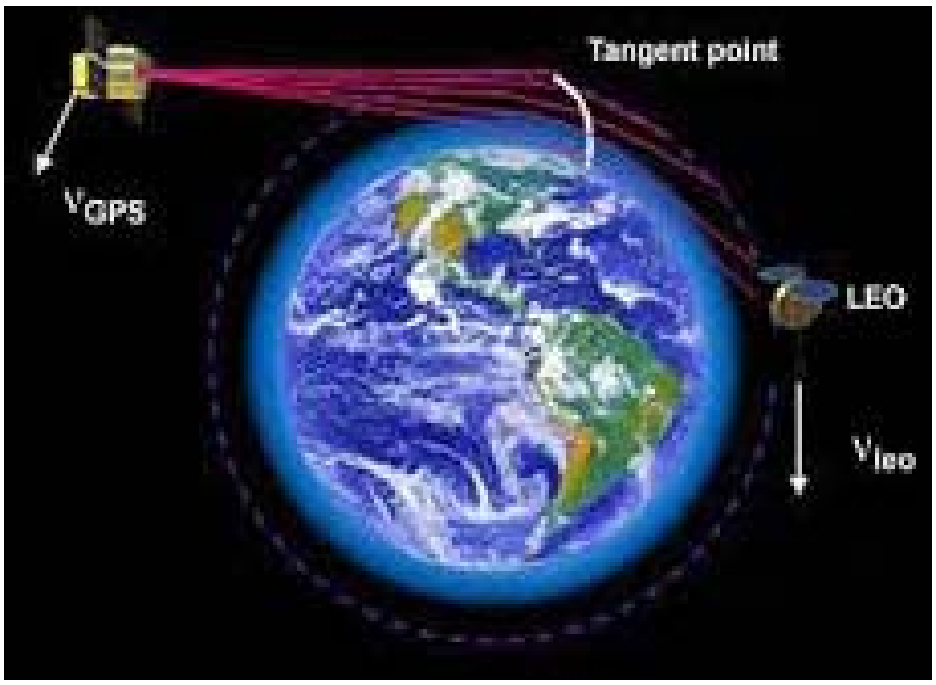

Fig. (1.2): Concept of atmosphere profiling using the GPS radio occultation technique, the velocity vector for GPS and LEO satellites vGPS and vLEO, respectively (Ghoniem et al., 2020).

The occultation technique uses GNSS navigation signals that LEO satellite receives. The success of the GPS/MET experiment motivated the scientific community to launch many other LEO satellites to study the Earth's atmosphere and ionosphere (Mousa et al., 2006). The GNSS occultation technique is based on precise dual-frequency phase measurements (L-band) of a GNSS receiver in a Low-Earth-Orbit tracking the signals of setting or rising GPS satellites. Combining these measurements with the satellites' position and velocity information, a

series (e.g. 50 Hz in case of CHAMP) of small atmospheric induced excess phases (up to ~ 1 km in the vicinity of the Earth's surface) during the occultation event can be derived with very high accuracy (XU and Zou, 2020). The temporal variation of this series (atmospheric induced Doppler shift) together with the signal's amplitude can be converted to a vertical profile of bending angles. Assuming spherical symmetric distribution of the atmospheric refractive index, vertical profiles of the refractivity can be derived and then converted to vertical profiles of atmospheric parameters as pressure, temperature and, using independent knowledge of temperature, also of water vapor partial pressure (Wickert et al., 2005).

A notable limitation of the RO technique is the assumption of spherical symmetry. The application of Bouguer's rule - and subsequently the Abel transform - enforces this assumption. In reality, the Earth and its atmosphere are not spherical, nor is the atmosphere spherically symmetric. This means that the bending angle profile is actually more of an averaged profile for a vertical cross section of the atmosphere, and refractive properties in any horizontal direction can disturb the measurements. Additionally, when the refractive gradient gets so sharp that the curvature of a ray matches or exceeds the curvature of the Earth, super-refraction (SR) occurs. This means that no ray will have its tangent point in a SR layer of the atmosphere, and we experience a corresponding gap in the received signal. The inverse Abel transform cannot uniquely map a bending angle profile with SR to just one refractivity profile.

Another complication comes from the ionosphere, which introduces a bias in bending angle retrievals. The standard way of correcting this bias is with a linear combination of the bending angles retrieved from the two

carrier frequencies of the GNSS transmitter. This is effective in most cases, although there will still be some residual ionospheric error. Additionally, occasional fluctuations in the ionosphere can greatly affect the quality of the signal (Sievert, 2019).

1.2 RS Method for Atmosphere Profiling

RSs are atmospheric sensors that provide an accurate, high-resolution description of the Earth's atmosphere from the ground to 30 km. RSs are carried into the air by latex weather balloons filled with helium or hydrogen (Abdelfatah et al., 2015). RSs measure atmospheric pressure, air temperature, water vapor (humidity) and winds (speed and direction). Modern RSs contain a GPS receiver to calculate wind speed and direction, and a radio transmitter to send the data back to the ground. Since they were first developed in the 1930s, RSs have become smaller, lighter, more accurate and less expensive (https://www.weather.gov/jetstream/radiosondes).

The most common use of RSs is for synoptic soundings, which are released once or twice a day (at 00hr and 12hr) from fixed locations around the globe. These soundings are carried out simultaneously by national weather services around the world to create a three-dimensional picture of the Earth's atmosphere at one point in time. Data from approximately 600 sites is transmitted to data centers for use in NWP models maintained by major governments and research institutions. These models produce the two to seven-day weather forecasts that everyone relies on for daily activities (https://www.weather.gov/jetstream/radio-sondes), (JetStream, 2022).

The first thing to understand about weather forecast models is that you need

data from many points on the globe. Some NWP models only simulate a region of the atmosphere, but global models (GFS, ECMWF) provide the boundary conditions for these regional models (ECMWF, 2022). As winds circle the globe, the weather you experienced today will become someone else's tomorrow. RSs are the backbone of NWP models, but vast amounts of data from other sources, such as surface stations, radars, and satellites, also are used to predict the weather (www.intermet-systems.com/products/Introduction-to-Radiosondes-and-AtmosphericSoundings/) (InterMet, 2022). So, depending on RO method in Egypt atmosphere identification will -with no doubt- increase the accuracy of weather identification besides the direct methods.

1.3 Statement of the Problem

RO meteorological profiles like pressure, temperature and Water Vapor Pressure (WVP) are not assessed in Egypt till now. No check for the applicability of using RO method in atmosphere identification and as a NWP model reliable input in Egypt till now. Also, GNSS signal zenith path delay (ZPD) based on the RO meteorology is not studied, assessed, and compared with other methods outputs in Egypt. The relation between the GNSS zenith path delay and its explanatory variables are not ever defined based on RO meteorological data before.

To assess RO observations, a reliable atmosphere identifier must be used to compare with. RS method is the reliable and spontaneous atmosphere identifier, so, it is axiomatic to compare with. After RO profiles assessment, ZPD must be assessed using another meteorological identifier and compared with GNSS-Precise Point Positioning (PPP) post processing ZPD. Also, linear regression is used to find the relation between ZPD by its dry and wet components and its predictors.

1.4 Research Methodology

RO data is downloaded for the study period years (2010 to 2020) from the web site: www.cosmic.ucar.edu/cdaac/ which is known as COSMIC Data Analysis and Archive Center (CDAAC) web site. Only the atmosphere profiles located in Egypt are included to be studied for all available LEO satellites in the study period. Shortage in each profile data was interpolated using LAGRANGE method to find the missed observations in each profile. CDAAC provides various netcdf files types containing different types of data. The file used in our research is called "wetprf" netcdf file which provides complete atmosphere profile containing observation altitude, pressure, temperature, WVP, analyzed and observed refractivity besides other parameters which not used in our research like wind speed and vectors.

RS data also is downloaded for the years 2010 to 2019 in netcdf files to study the differences between the RO and RS profiles. Year 2020 is excluded due to RO data shortage. Processing is executed using bash scripts and FORTRAN subroutines. RO and RS netcdf files are read using a FORTRAN program constructed for data reading and preprocessing preparation.

RO-RS single profile comparison is done to check the rapprochement between the two profiles. A T-test is made to check the similarity between the meteorological profiles. Multi-profiles statistical differences are studied to compare the RO profiles and to check the integration of the two techniques observations. The height from 3 to 40km is used in RO and RS data comparison as beneath the 3km altitude there are many data shortages in RO and RS profiles.

Zenith Hydrostatic Delay (ZHD) and Zenith Wet Delay (ZWD) are estimated based on RO and RS and compared with each other and with PPP online processing results. Check points that has RO, RS and GPS observations in the same time and location are used to compare ZPD for the three methods. A T-test is done to check the compatibility between the three methods.

To find the relation between the ZPD and its predictors, linear regressions are executed for each of ZHD and ZWD with the meteorological parameters, time, and spatial changes. A linear model is constructed based on the linear regression to find the constants and each variable parameter for each of ZHD and ZWD with their predictors.

1.5 Research Objectives

One of the main research objectives is studying the applicability of RO method in Egypt. The first sub objective is to assess the RO meteorological profiles in Egypt with a reliable method like RS. The second one is to assess the ZPD derived from the RO with it for the RS and with PPP processing results to find the confidence degree in ZPD derived from the RO and to recommend about using it for ZPD calculation in Egypt. Finally, ZHD and ZWD models are to be constructed based on RO data and as a result, PPP processing models will be advised to use them in their processing steps.

1.6 Thesis Organization

A general background for RO and RS techniques, problem statement, research methodology, objectives and outlines are presented in chapter 1. Previous researches in RO and RS comparison and in ZPD estimation models are reviewed to show the general thoughts about the

research strides in chapter 2. Besides in the same chapter, data download web sites, data format, case study time and regions are demonstrated. Chapter 3 shows the RO and RS data processing, analysis procedures for RO and RS profiles and delay comparisons and the linear regression models construction details for the ZPD components. Chapter 4 shows the research results and its discussions. Finally, chapter 5 shows the conclusions, summary, and recommendations.

1.7 Research Outlines

The main research outlines are abridged as follows:

- Analysis of the differences between the RO and RS profiles.
- Analysis of the differences between the RO and RS based on LEO satellites.
- Analysis of the differences between the RO and RS based on RS stations.
- Analysis of the differences between the ZPD components estimated based on the RO, RS and PPP processing results.
- Studying the relations between the ZHD and ZWD with their predictors.
- Construct ZHD and ZWD models based on their explanatory variables.

CHAPTER 2

DATA AQUICITION

Chapter 2 : Data Acquisition

Several previous researches did the comparison between the RO and RS profiles. All available LEO satellites are assessed in the present research. All LEO satellites assessment is considered from our research added values as most of the previous researches assessed only one LEO satellite profiles and section (2.1) reviews these researches. Concerning to ZPD models, the present research added value lies in using a big number of RO data which distributed randomly over the study period and region. Section (2.2) reviews the researches done to find the ZPD components predictors and their weights.

Concerning to data used in the present research, four types of data were used in the present research: RO, RS, GPS observations and European Centre for Medium-Range Weather Forecasts (ECMWF) model data. RO data is considered the main data source in our research. Our main research objective is to make sure of the ability of integrating the RO data with the other atmosphere identifier methods. RS data is used to analyze the RO-RS differences in atmosphere profiles. GPS observations PPP processing ZPD is used to check the differences in delay values between GPS-PPP analysis and delay values based on RO and RS profiles. ECMWF model data is used to assess the impact of temporal and spatial changes on meteorological parameters and then on the zenith path delay values.

In this chapter, previous studies in each of research sectors are reviewed. Also, RO and RS data acquisition are discussed and data file download, availability, type, shape, format, contents, and interpolation methods are identified. Accordingly, research algorithm and logical

context are cleared.

2.1 RO and RS Profiles Comparison Previous Studies

Kuo et al., (2005) compared the GPS RO and RS data in CHAMP soundings in the primary stage of RO method. Their results indicated that the RO soundings were of sufficiently high accuracy to differentiate performance of various types of RSs. Norman et al., (2014) also compared the GPS RO and RS data in the Australian region. Their study is based on the six COSMIC satellites data assessment. Also, they got enough data to compare temperature and pressure profiles only. They concluded reasonable and accepted differences between the COSMIC GPS-RO profiles and the RS profiles and reasoned all differences source and value. Chang et al., (2018) also did the comparison in COSMIC data and found a big similarity between the different profiles. They indicated that the RO data could compensate for the low spatial resolution in RS data.

2.2 ZHD and ZWD Models Previous Studies

The GNSS have been used widely for navigation, positioning, and atmospheric science research applications because of its high precision, high temporal resolution, all-weather capabilities, and low cost. However, when passing through the atmospheric layer, GNSS signal is delayed by the effect of the atmosphere, including the ionosphere and troposphere (e.g., Bohm et al., 2015). Ionospheric delay can be eliminated by ionosphere-free linear combination formed from dual frequency observables. Therefore, tropospheric delay is considered as the main error budget in measurements at neutral atmosphere. This type of delay cannot be corrected easily because of the non-dispersive behavior of the troposphere. Studies have shown that GNSS signal transmission delay caused by the troposphere can vary from over 2 m at the zenith to over 20

m at elevation angles of 10° between the receiver and satellite (Penna et al., 2001), thus a good way to model the tropospheric delay is to express it as the product between the Zenith Total Delay (ZTD) and a mapping function (MF) depending on the sin of elevation angles. Currently, the famous MF includes New Mapping Function (NMF) (Niell, 1996), Global Mapping Function (GMF) (Boehm et al., 2006), Vienna Mapping Function (VMF1) (Boehm et al., 2009) and so on. Meanwhile, many ZTD empirical correction models have been developed to mitigate the effects of tropospheric delay and these can be divided into two categories according to parameter type. In the first configuration, all the models require meteorological parameters, such as the conventional Hopfield model (Hopfield, 1963; 1969), Saastamoinen model (Saastamoinen, 1972), and Black model (Black, 1978). The application of such models in real-time navigation would be compromised if restricted to using standard reference atmospheric parameters because this information would greatly reduce their accuracy. The second type of models comprises those that do not require meteorological parameters, such as the UNB series (UNB3, UNB3m, and UNB4) models (Collins and Langley, 1997), EGNOS model (e.g., Penna et al., 2001), IGGtrop model (Li et al., 2012), GZTD model (Yao et al., 2013), ITG model (Yao et al., 2015) and GPT2w (Bohm et al., 2015).

2.3 RO Data Used in Analysis

Seventeen LEO satellites which data is available online in CDAAC web site through the study period and region: COSMIC1-6 MetOpA, B, C, SAC-C, TerraSAR-X1, TSX/TanDEM-X, PAZ, KOMPSAT5, GRACE1, 2 and C/NOFS are the LEO satellites used in the present research. Only observations for nine of them are used in meteorological profiles comparison as being located near upper

air stations observations. The following paragraphs will briefly review each of the LEO satellites used in the study with its abbreviation mean.

Constellation Observing System for Meteorology, Ionosphere, and Climate (COSMIC) is consisted of six satellites designed to enhance the meteorological observations accuracy and ionospheric research. The constellation is a joint United States (U.S.)-Taiwanese project with major participants including the University Corporation for Atmospheric Research (UCAR). The constellation is circularly orbiting in an altitude of 700-800 km with inclination 72° with the Equator (www.cosmic.ucar.edu). The UCAR COSMIC Program has been a leader in the retrieval and scientific application of GNSS (e.g., GPS), data since UCAR led the GPS/MET GPS-RO mission in the mid 1990s. It contributed to the design, management, and operation of the FORMOSAT-3/COSMIC-1 mission since 2006 (data available from 2006.112 to 2014.120). The mission is still providing high-quality RO profiles that are having a significant positive impact on weather and space weather forecasting and research. The success of COSMIC has prompted U.S. agencies (led by National Oceanic and Atmospheric Administration NOAA) and Taiwan's National Space Organization to execute a COSMIC follow-on operational mission called FORMOSAT-7/COSMIC-2 that has put six satellites with next generation GNSS RO payloads into low Earth orbit (data available from 2014.121 to 2020.116). In 2018 U.S. agencies decided to launch the third generation called COSMICRT (data available from 2019.001 to 2020.116) (www.cosmic.ucar.edu).

MetOp (Meteorological Operational satellite) is a series of three polar-orbiting meteorological satellites (MetOpA, B, SG) developed by the European Space Agency (ESA) and operated by the European

Organization for the Exploitation of Meteorological Satellites (EUMETSAT). In the present research, only MetOp A, B are used in processing because of their data availability, (ESA, 2022).

SAC-C is an international cooperative mission between National Aeronautics and Space Administration (NASA), the Argentine Commission on Space Activities (CONAE), Centre National d'Etudes Spatiales (CNES or the French Space Agency), Instituto Nacional De Pesquisas Espaciais (Brazilian Space Agency), Danish Space Research Institute, and Agenzia Spaziale Italiana (Italian Space Agency). SAC-C was developed through the partnership of its senior partners, CONAE and NASA with contributions from Brazil, Denmark, France, and Italy. SAC-C provides multispectral imaging of terrestrial and coastal environments. The spacecraft will study the structure and dynamics of the Earth's atmosphere, ionosphere and geomagnetic field. SAC-C will seek to measure the space radiation in the environment and its influence on advanced electronic components. The satellite will determine the migration route of the Franca whale and verify autonomous methods of attitude and orbit determination (nasa.gov/centers/goddard/pdf/110896-main_FS-2000-11-012-GSFC-SAS-C).

TerraSAR-X1 is a German satellite mission for scientific and commercial applications. The project is supported by German Ministry of Education and Science (BMBF) and managed by German Aerospace Center (DLR). The satellite is owned and operated by DLR, and the scientific data rights remain with DLR. The satellite has a design life of at least five years. The science objectives are to make multi-mode and high-resolution X-band data available for a wide spectrum of scientific applications in such fields as: hydrology, geology, climatology, oceanography, environmental and disaster monitoring, and cartography (earth.esa.int/web/eoportal/satellite-missions/) (EOPortal, 2022).

TSX/TanDEM-X is a high-resolution interferometric mission of DLR, together with other partners. The mission concept and goals is based on a second TerraSAR-X radar satellite flying in close formation to achieve the desired interferometric baselines in a highly reconfigurable constellation (earth.esa.int/web/eoportal/satelli-te-missions/).

The PAZ (Spanish for "peace") satellite, launched on 22 February 2018, is owned and operated by Spanish company provides satellite services to government organizations focused on defense, safety, intelligence, and external affairs (Hisdesat), and is based on the use of a high resolution X-band Synthetic Aperture Radar (SAR). PAZ operates in the same orbit of the twin satellites TerraSAR-X and TanDEM-X, and the three satellites work together as a constellation. PAZ flies in a polar dawn-dusk sun-synchronous orbit, which allows it to cover all of Earth with a mean revisit time of 24 hours (earth.esa.int/eogateway/missions/paz).

KOMPSAT5 (Korean Multi-purpose Satellite 5) or Arirang 5 project and its goal is to lead the development of the first Korean SAR Satellite using manpower and facilities from the KOMPSAT-3 program. It aims to support the national SAR satellite demand and form a technology infrastructure to make inroads into the world space industry. KOMPSAT-5, which was developed since in the middle of 2005, was launched in 2014 and its payload is a X-band SAR a, which operates at Dawn-Dusk orbit between an altitude of 500 km to 600 km. It executes all weather and all day observations of the Korean peninsula during its five year mission using the SAR payload. And in order to meet the urgent national needs for various SAR image information, the KOMPSAT-5 GOLDEN Mission will provide Geographical Information Systems (GIS), Ocean monitoring, Land management, Disaster monitoring, and Environment monitoring (earth.esa.int/web/eoportal/-satellite-missions/).

The Gravity Recovery and Climate Experiment (GRACE) was a joint mission of NASA and the DLR includes two satellites (GRACE1, 2) to improve gravity and climate research (data available from 2007.059 to 2017.334). The satellites were launched in an altitude of 500km with inclination of 89° and with an orbital distance 220km between them (podaac.jpl.nasa.gov/GRACE) (NASA, 2022; PODAAC, 2022).

Communication/Navigation Outage Forecast System (C/NOFS) is a collaborative U.S. satellite mission undertaken by U.S. Department of Defense (DoD) with other participants. It orbits with an altitude of 405 km x 800 km, inclination of 13º and a period of 97.3 minutes (data available from 2010.060 to 2011.365) (earth.esa.int/web/eoportal/satellite-missions).

All observations data are available to be downloaded through UCAR-CDAAC website for free (cdaac-www.cosmic.ucar.edu/cdaac/). UCAR-CDAAC provides us by continuous data for all RO-LEO missions since 2006. Data available in UCAR-CDAAC are: Ionosphere TEC, troposphere pressure, temperature and WVP and other data types for COSMIC and the other LEO missions. Only GPS constellation signals data are available in UCAR-CDAAC website. As a result, all comparison analysis is based on GPS constellation data only.

Almost all RO-LEO satellites locate ROEs in Egypt. Goniem et al., (2017) found the number and the distribution of ROEs located in Egypt to be about 70 ROE due to all LEO missions using simulations analysis. Simulation analysis assumed the full operating and data access for all satellites, and this is not happening at any time. The number and the distribution of ROEs vary from satellite to another. Actually, the number of ROEs at any time may not exceed the half of the number indicated above.

In RO-RS data comparison, our study is based on the ROEs located near the RS stations and approximately in the same mission time as check points. COSMIC1-6, GRACE1,2 and C/NOFS are only the missions which located ROEs near the RS stations and near its mission time. COSMIC by its six satellites have the big share of check points in Egypt.

Due to the geometry of the GPS and LEO satellite in the space, the number, distribution, and time of ROEs are determined. The ROEs that match the position and the mission time of upper air missions are exploited to assess the RO profiles in Egypt. Data could be downloaded by setting the LEO satellite name and mission and type of file. A "netcdf" file is downloaded including the meteorological data you requested. A FORTRAN subroutine is made to extract data in matrices to deal with.

There are many types of data files available at UCAR-CDAAC (UCAR, 2022). "atmprf" contains atmospheric profile without moisture information. "Wetprf" contains atmospheric occultation profile with moisture information included. "ionprf" contains ionospheric data profile for a single occultation. "sonprf" contains temperature, pressure and moisture profiles generated from RS data and collocated with occultation profiles. Almost all the main RO data files are presented in "netcdf" format.

"Wetprf" file gives us a complete profile of pressure, temperature, WVP and refractivity except at low altitudes. All of these parameters are calculated from the signal path excess and bending angle. Various methods were tested to choose the best one for interpolation. Lagrange polynomial is used in interpolating pressure, vapor pressure and refractivity as it gave the best fitting curve in testing. Temperature is interpolated linearly as it is the best for it.

Fig. (2.1) shows the number of RO observations for each LEO

satellite in Egypt through the study period. MetOpA has the maximum number of RO events through the study period. MetOpB comes in the second order then COSMIC 1, 6, 5, TSRX, KOMPSAT5, COSMIC2, 4, GRACE1, MetOpC and GRACE2, respectively, which have an effective number of RO observations.

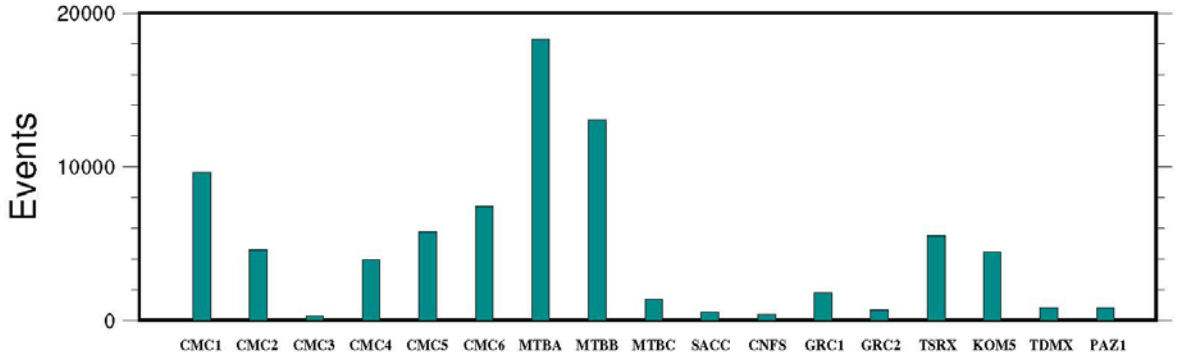

Fig. (2.1): Number of Observations for Each LEO satellite.

Fig. (2.2) shows the distribution of each LEO observations through the study period years. MetOpA comes in the first order in data amount and stability through the study period. It gives a good number of observations through each year from 2010 to 2020 by more than 1500 ROE/year in most of years. As a result, MetOpA is considered the ideal atmosphere LEO satellite identifier for Egypt in the last decade. MetOpB started providing data in 2013.

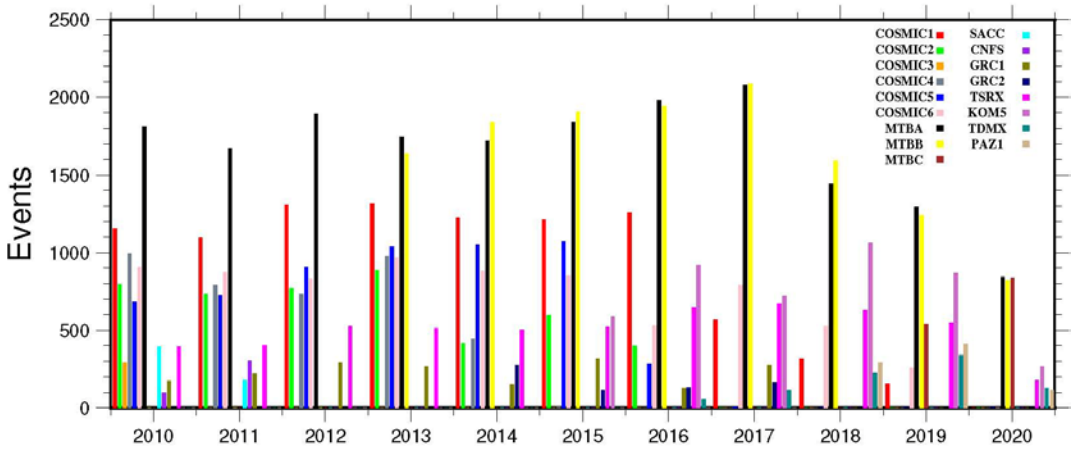

Fig. (2.2): Number of observations for each LEO satellite in each year.

Till now MetOpA, B are providing the world by atmosphere data. Also, TSRX provided Egypt by about 500 ROE/year give or take in uniform manner over the study period. COSMIC1, 6 provides Egypt by data from 2010 to 2019 by a number reaches 1000 and 800 ROE/year give or take in most of years, respectively.

Figs. (2.3 and 2.4) show the distribution of ROE over Egypt in 2011 and 2015, respectively, using the color indication for each LEO satellite. COSMIC2 provides Egypt by data from 2010 to 2016 by about 500 ROE/year give or take in most of years. COSMIC3 provides Egypt by data in 2010 only by about 300 ROE/year. COSMIC4 provides Egypt by data from 2010 to 2014 by a number reaches 1000 ROE/year in most of years. COSMIC5 provides Egypt by data from 2010 to 2016 by a number reaches 1000 ROE/year in most of years. GRACE1, 2 provides Egypt by data through 2010 to 2017 and 2014 to 2017 periods, respectively, by about 300 ROE/year. KOMPSAT5 provides Egypt by data from 2015 to 2020 by a number reaches 1000 ROE/year. PAZ1 and TDMX provide EGYPT by a number reaches 300 ROE/year in the last 3 and 5 years, respectively.

The difference in LEO satellite missions that cover Egypt through the two years is obvious in the figures. 2011 and 2015 are covered by ten LEO satellites; however, MetOpB effect is obvious in 2015 by a big number of observations with a uniform distribution over Egypt. KOMPSAT5 also appear obviously in 2015 and not in 2011. COSMIC4 observations are clear in 2011 and not in 2015. Also, SACC and CNFS appear cover Egypt in 2011 and not in 2015.

Fig. (2.5) shows the distribution of ROE through the whole study period and for all LEO satellites. The figure is just for overall indication for the distribution and the number of observations for all LEO satellites in Egypt.

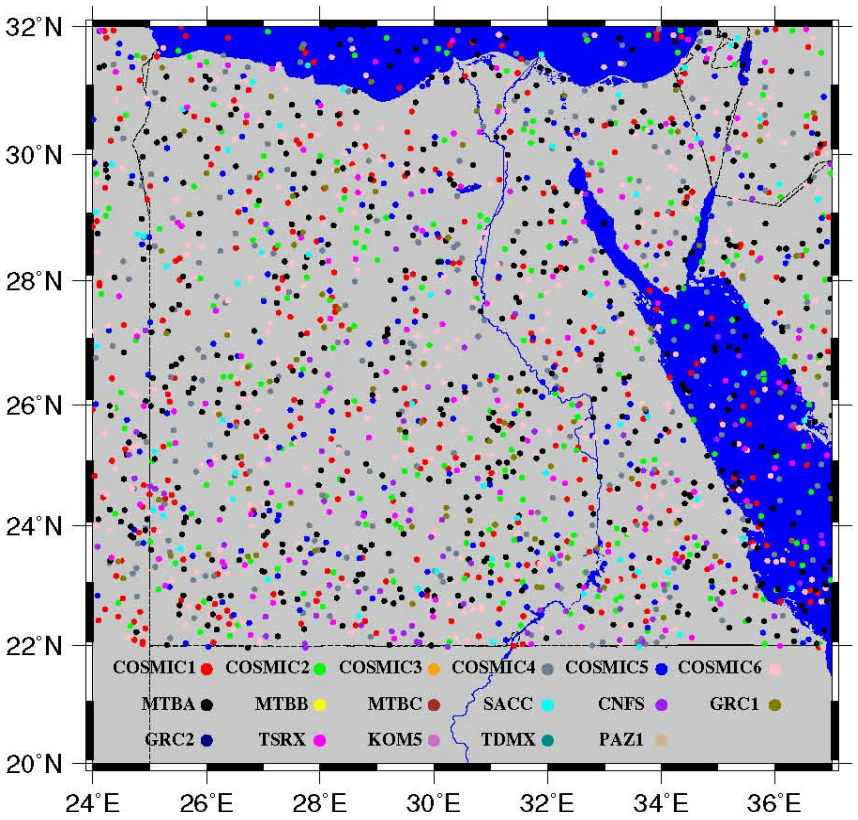

Fig. (2.3): Distribution of ROE over Egypt in 2011.

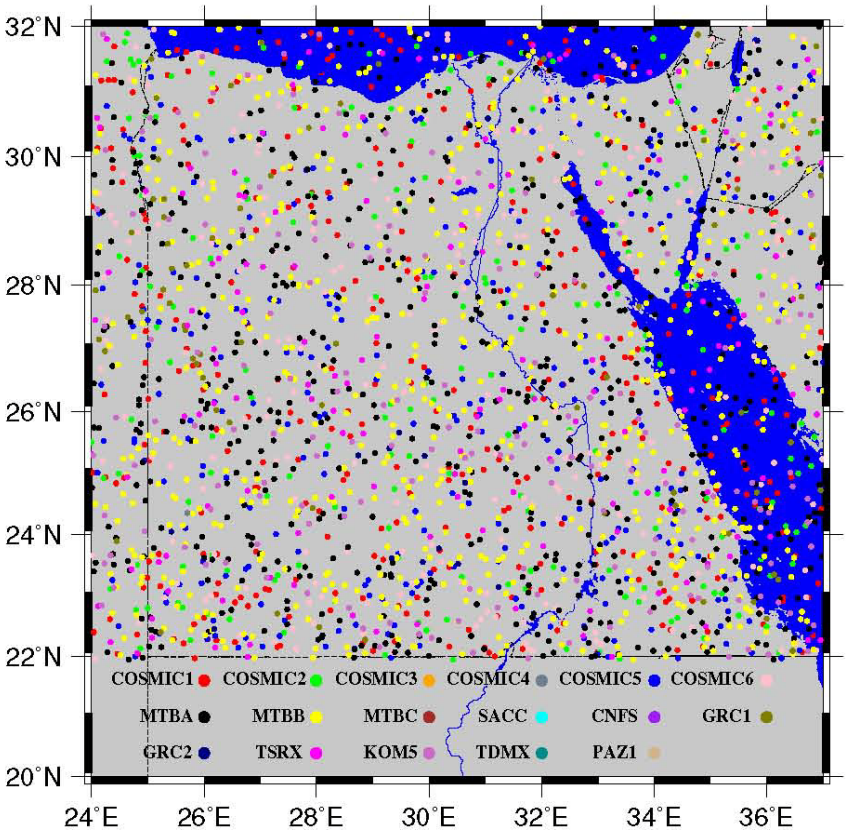

Fig. (2.4): Distribution of ROE over Egypt in 2015.

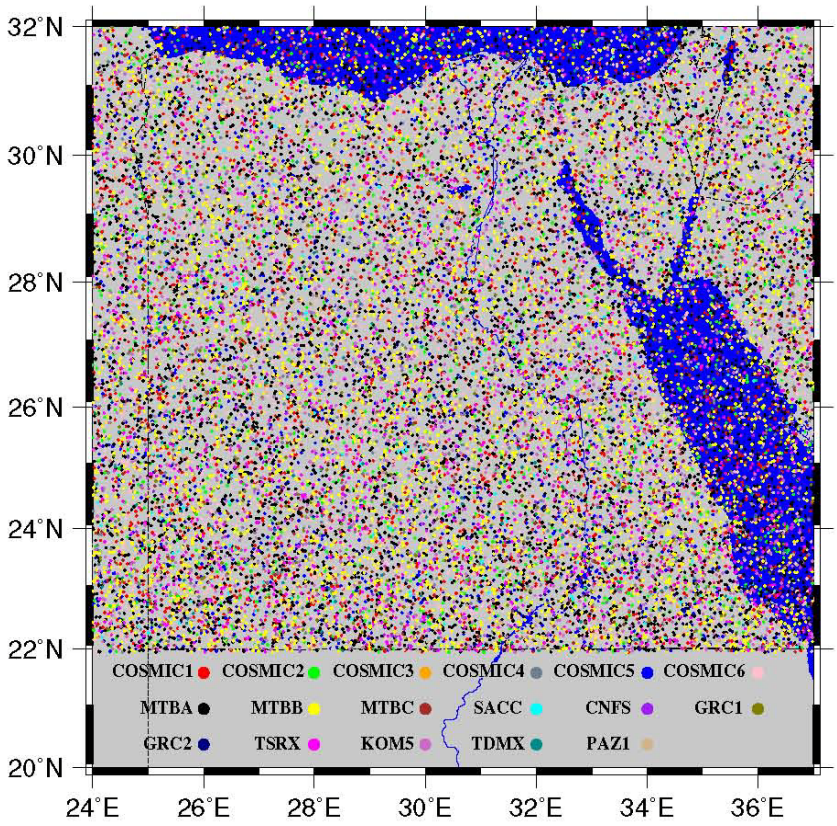

Fig. (2.5): Distribution of ROE over Egypt in 2011-2021.

Although the number of observations exceed 50000 observations, the number of observations used in processing is not exceeding 15000 observations. This data reduction is caused by putting rules and specifications in the profiles chosen used in processing. The profiles chosen in processing must not have any shortage of data for any variable for 4 consecutive observations. Also, profiles that have any data shortage for a distance exceeds 3 km from the Earth surface were enslaved.

2.4 RS Data Used in Analysis

Atmospheric parameters could be measured nowadays using several sophisticated and convoluted methods. However, upper air sounding method still owns the bookmark and reliability. Also, for directly studying the troposphere to stratosphere regions, weather balloons remain one of our most powerful tools. In particular, the Integrated Global RS Archive (IGRA) dataset currently provides more than half a century of archived

weather balloon soundings from more than 1000 stations (Connolly et al., 2021). Although RS observations have traditionally been taken primarily for the purpose of operational weather forecasting, they are critical to other applications, including model verification, climate research, and the verification of satellite measurements (Durre et al., 2006).

IGRA includes more than 2700 RS stations all over the world. Observations are available in different types of levels like pressure, wind and altitude levels. Observations include pressure, temperature, geopotential height, relative humidity, dew point depression, wind direction and speed, and elapsed time since launch (www.ncdc.noaa.-gov). All upper air RS stations located in or around Egypt are used for assessment. Atmosphere profiles measured by RS method are available in many international organization's websites. Data used for assessment are downloaded from NOAA website for free (ruc.noaa.gov/raobs/). NOAA is an organization affiliated to the U.S. government targeting to enhance the Earth sciences generally. Table (2.1) shows the number and locations of each station used for assessment in the present research. Some of the RS profiles are not complete. There are many data shortages especially in the lower and the upper zone of each profile. Data extrapolation and interpolation are used to cover the shortage in data and uniform the data with fixed altitude spacing. The same methods of interpolation in RO data were used in RS data interpolating. Pressure, temperature, and dew point depression are the raw data available at NOAA website (NOAA, 2022). Data could be downloaded by setting the region borders and type of data. A "netcdf" file is downloaded including the meteorological observations you requested.

Table (2.1): Upper air stations number, latitude and longitude.

St. Num.	St. Name	Lat. (deg.)	Lon. (deg.)
62378	Helwan	29.86	31.33
62414	Asswan	23.96	32.78
62403	South Of Valley Univ.	26.20	32.75
62423	Farafra	27.05	29.96
16754	Heraklion	35.33	25.18
17607	Athalassa	35.15	33.40
40179	Bet Dagan	32.00	34.81
40265	Mafraq	32.37	36.25
40375	Tabuk	28.38	36.60
40430	Al-Madinah	24.55	39.37
41024	Jeddah (King Abdul Aziz Int. Airport)	21.70	39.18
62053	Benina	32.10	20.27
62306	Mersa Matruh	31.33	27.21

A FORTRAN subroutine was made to extract data in matrices to deal with. From the dew point depression, WVP is calculated as indicated in equation (2.1 and 2.2).

$$\mathrm{Tdp(°c)} = \mathrm{T(°c)} - \mathrm{Dpd(°c)} \tag{2.1}$$

$$e(mb) = 6.11 * 10^{\frac{7.5 * Tdp\,(°c)}{237.3 + Tdp\,(°c)}} \tag{2.2}$$

Where Tdp is the dew point temperature, T is the temperature, Dpd is the dew point depression and e is the water vapor pressure.

Fig. (2.6) shows the distribution of RS stations in and around Egypt with station number according to IGRA. Upper air stations usually launch twice observer balloons per day. Usually, the balloons launch is done at 00.00 12.00 UTC plus or minus some minutes. The first two or three KMs in altitude usually have problems in observing. Also, some balloons bursts

after 7 KMs more or less as stated before. As a result, not completed profiles are produced for these not completed missions. But most of upper observations reach more than 25 KMs. All ineffective missing data are made up using interpolation and extrapolation methods indicated before.

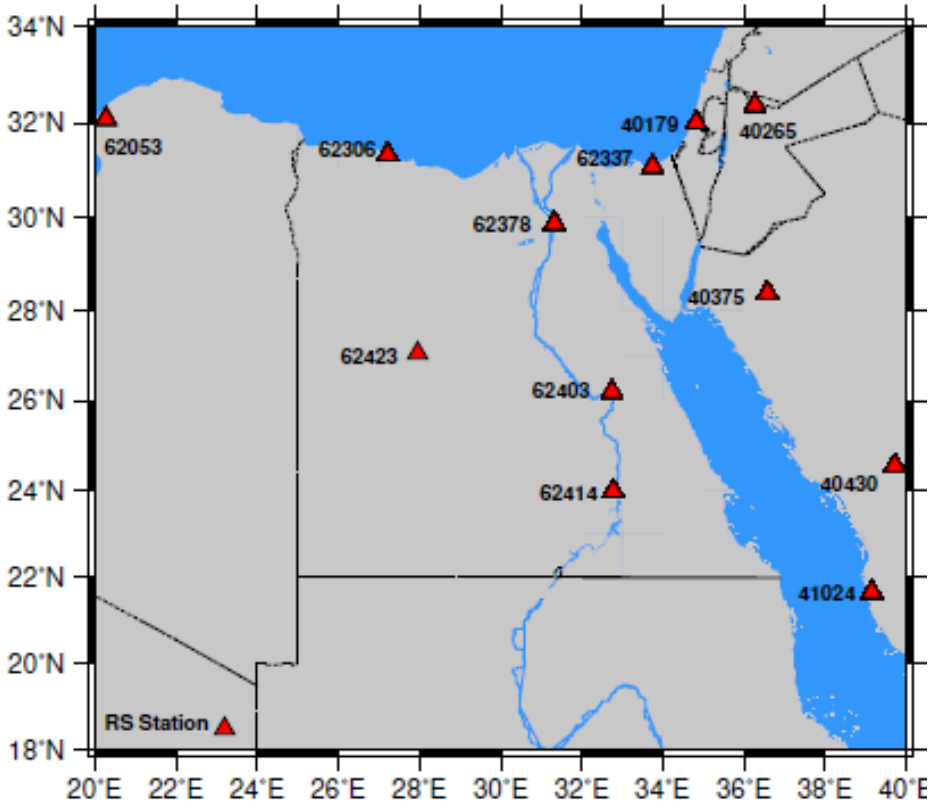

Fig. (2.6): Distribution of RS stations in Egypt.

2.5 GPS Observations

The Continuously Operating Reference Stations (CORS) are now widely spread all over the world. The ground-based dual-frequency GPS observations are affected severely by the troposphere. For all precise CORS applications which are supported by code observation data, existing code (or pseudorange) biases represent a non-negligible error source. This includes “time-oriented” applications such as high-precision GPS satellite clock estimation as well as time transfer among GPS observing stations. To accurately mitigate the ionospheric error effect on GPS solution, the

Differential Code Biases (DCB) need to be compensated (Dach et al., 2007).

Egyptian GPS observations are used to compare the RO-ZHD, RO-ZWD, RS-ZHD and RS-ZWD values with the results of GPS observations CSRS-PPP processing. Nine GPS stations from National Research Institute of Astronomy and Geophysics (NRIAG) network were used in the current research. Helwan (PHLW), Aswan (ASWN), Marsa Alam (ALAM), Marsa Matrouh (MRSA), Mansoura (MNSR), Assiut (ASUT), Hurghada (HURG), Suez (SUEZ) and Damietta (DMIT) are the selected stations. Data are collected using two different Trimble model receivers; Trimble 5700 and Trimble NETR5. Data was in Receiver INdependent EXchange format (RINEX) format with one second sampling rate. The elevation cut-off angle of 3° was used for the collected data.

To compare RO, RS and GPS-CSRS-PPP processing results, it was a must to find time and spatial synchronized observations. Check point is the point that has RO, RS and GPS observation in the same time and location. Through ten years of data (2010-2019), check points were chosen based on the time and location of each observation. A tolerance of 100 km in distance difference and of 60 minutes in time difference was fair to find adequate number of check points; however, lowering the temporal and spatial differences is preferable. But, to find a good number of check points, it was a must to use these spatial and temporal differences.

2.6 ECMWF Model Data

The ECMWF is an independent intergovernmental organization supported by 35 states. ECMWF is both a research institute and a 24/7 operational service, producing and disseminating numerical weather predictions. This data is fully available to the national meteorological

services in the Member States. The Centre also offers a catalogue of forecast data that can be purchased by businesses worldwide and other commercial customers. The supercomputer facility (and associated data archive) at ECMWF is one of the largest of its type in Europe and Member States can use 25% of its capacity for their own purposes (ecmwf.int/en/).

ECMWF model is used to determine the temporal and spatial changes in pressure, temperature, vapor pressure and refractivity values. The differences in meteorological parameters values between RO and RS were not justified. ECMWF is used to know the normal values for these differences. The pressure, temperature, vapor pressure and refractivity data were downloaded using the link (https://cds.climate.copernicus.eu/cdsapp-#!/dataset/reanalysis-era5-pressure-levels?tab=form) in different positions and epochs.

CHAPTER 3

DATA ANALYSIS

Chapter 3 : Data Analysis

In this chapter, Abel transform for refractivity derivation is discussed briefly. RO-RS single profile analysis will be clarified to show the methodology of comparing RO and RS single profiles. Also, analysis procedures of comparing a group of profiles will be demonstrated. ZPD calculation is discussed based on RO and RS data. Methodology of comparing RO-ZPD by its components (ZHD and ZWD) with RS-ZPD and GPS-PPP observations processing results will be presented also in this chapter. Besides, GPS-PPP processing methodology and results shape will be clarified. Finally, analysis of ZPD relations with time and other meteorological parameters is described.

3.1 Abel Transform Inversion

The technique, which has been widely used in the study of planetary atmospheres (e.g., Fjeldbo et al., 1971), is based on measuring how radio waves are bent by refractive index gradients in an atmosphere. It can be shown that by assuming spherical symmetry (e.g., Kursinski et al., 1997) this information can be inverted with an Abel transform to give a vertical profile of refractive index and subsequently temperature.

The theory of RO with a receiver in space has been described in detail by a number of authors (e.g., Melbourne et al., 1994; Kursinski et al., 1997; Rocken et al., 1997). Briefly, the RO technique is based on measuring how radio waves emitted by a GPS satellite are bent by refractive index gradients before being received by a LEO satellite. The geometry is shown in Fig. (3.1). The LEO is typically 500-900 km above the surface of the Earth, whereas the GPS satellite is around 22000 km above the Earth surface. The receiver on the LEO satellite measures the

phase and amplitude of the GPS signal. An excess phase delay is introduced because the neutral atmosphere refractive index is greater than unity and the ray path is curved. Both satellites are in motion, so the frequency of the received signal is Doppler shifted. The time derivative of the excess phase gives the additional Doppler shift introduced by the atmosphere, which arises because the ray bending modifies the angle of intersection at the satellites relative to the straight-line path (Healy et al., 2002).

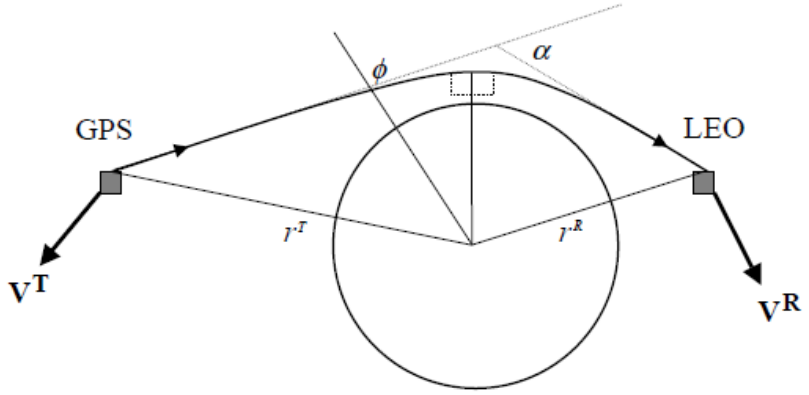

Fig. (3.1): The geometry of an RO measurement with a receiver on board a LEO satellite.

If the position and velocity vectors of the satellites are known accurately the excess Doppler shift can be inverted, assuming spherical symmetry, using Bouguer's formula (Born and Wolf, 1986), to yield bending angle α and impact parameter $a = n * r * sin\emptyset$ (which is constant along the ray path for a spherically symmetric atmosphere), where n is the refractive index value, r is the radius and $\emptyset$ is the angle between the ray vector and the radius vector. Deriving α and a requires an iterative approach and it is usually performed assuming the refractive index is unity at the satellites.

If the atmosphere is spherically symmetric the bending angle, α, can be written as in equation (3.1),

$$\alpha(a) = -2a\int_a^{\infty} \frac{\frac{d\ln n}{dx}}{(x^2+a^2)^{0.5}} \tag{3.1}$$

where $x = n * r$. It is a convention in RO to write the upper limit of this integral as infinity, but in practice if the refractive index at, and above, the receiver is effectively unity this can be replaced with r^R, the radius of receiver. The difference in the satellite radii is not important if there is no ray bending along sections of path where $r > r^R$. Note that the GPS satellite transmits at two frequencies (L1=1575.42 MHz and L2= 1227.6 MHz) and the bending due to ionospheric plasma is removed or "corrected", to first order, by taking a linear combination of the L1 and L2 bending angle values (Vorob'ev and Krasil'nikova, 1994). For a spherically symmetric atmosphere, the variation of the corrected bending angle with impact parameter can be inverted with an Abel transform (Phinney and Anderson, 1968; Fjeldbo et al., 1971) to recover the refractive index profile as indicated in equation (3.2),

$$n(x) = \exp\left(\frac{1}{\pi}\int_x^{\infty} \frac{\alpha(a)}{(a^2-x^2)^{0.5}} da\right) \tag{3.2}$$

which can be evaluated numerically. A useful substitution is $a = x\cosh\theta$. Once again, the upper limit of this integral could be replaced with r^R. The refractive index can be written as $n = 1 + 10^{-6}N$, where N is the refractivity by its two components, dry and wet refractivity. In the neutral atmosphere the refractivity is related to the temperature and the partial pressures of dry air and water vapor pressure, P and e through as indicated in equation (3.3),

$$N = \left(N_{dry}\right) + \left(N_{wet}\right) = \left(77.6\frac{Pd}{T}\right) + \left(64.79\frac{e}{T} + 3.776 * 10^5\frac{e}{T^2}\right) \tag{3.3}$$

Where: T is the temperature in Celsius, e is the water vapor pressure in millibar (mb), and Pd is the dry atmosphere pressure in mb. More

generally, the refractivity measurement contains both temperature and water vapour information and this is referred to as the "water vapour ambiguity". Water vapour can be derived from the refractivity using a priori temperature profile information (Kursinski and Hajj, 2001), but it is not advisable to derive a temperature profile with type of approach, because the uncertainty in the a priori water vapour can lead to large errors. Alternative methods for solving the water vapour ambiguity are based on statistically optimal inversion techniques (e.g. Healy and Eyre, 2000; Palmer et al., 2000).

3.2 Analysis of the Differences between RO and RS Profiles

The present research examines the RO profiles accuracy using RS data in Egypt. ROEs located in Egypt by all LEO satellites from 2010 to 2020 are examined. The downloaded RO & RS data location exceeds the Egyptian borders by two or three degrees in latitude and longitude in all directions. The available RO data are produced from GPS constellation in conjunction with the LEO satellites.

The average number of ROEs distributed in Egypt is 22 ROE/day in the period from 2010 to 2020. The nearest ROEs in time and location to the RS missions are chosen to compare with the RS atmosphere profiles. Ten years of GPS-RO and RS data are used in comparison. RO-RS comparison algorism is indicated in Fig. (3.2).

All LEO satellites and all upper air stations in or near Egypt are used in comparison. All data profiles vertical spacing is united using interpolation to 25 m in altitude difference. Many interpolation methods are tested to get the missed data and the best resolution of data by the most effective method. It was a must to interpolate data as the RS data is available in pressure levels only starting from 925 to 7 mb by not equal

difference and on the other hand, available RO meteorological variables are given per a fixed height (100 m). So, it was a must to unite the scale of comparison using interpolation.

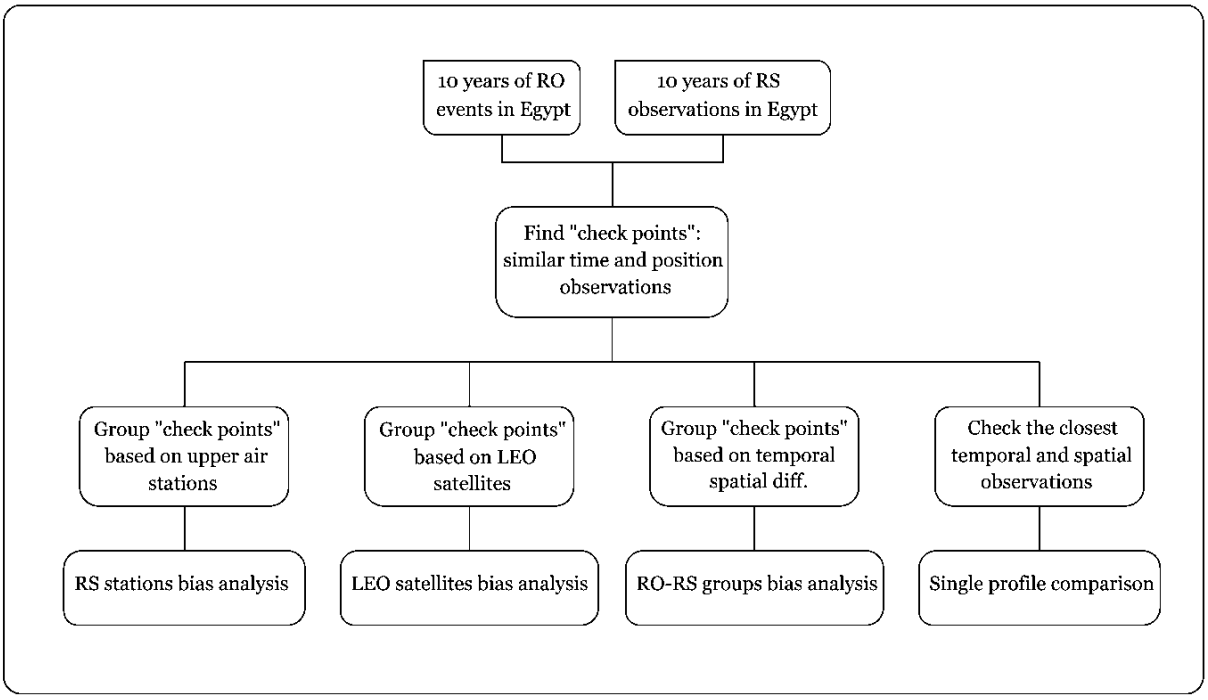

Fig. (3.2): RO-RS comparison methodology flow chart.

Fig. (3.3) shows the upper air station and the ROEs distribution on the day of Julian Date (JD) = 2456940. The number of ROEs in this day was 12 ROE where the average number of ROEs in 2010-2020 years is 20 ROE per day. This day was chosen as it has the ROE "C006-2014.282.23.48.G19" which matches in time and location other RS mission by difference of 14 minutes in time and 22 km in distance and called "point1". This point is considered the best point of judgment as it matches perfectly in time and location other RS mission for station 62378. "Points 2, 3" have difference of 19, 13 minutes and 33, 35 km in time and distance for the observations "C005-2013.005.00.21.G05" and "C005-2010.025.00.13.G26" matched with missions from station 62414, Mersa Matruh, respectively.

To judge the degree of significance for the meteorological parameters changes between the RO and RS methods, two statistical tests were carried out. A T-test and correlation were studied to find the degree of concurrence between two single RO and RS profiles. Also, T-test and correlation were studied to get the degree of significance of the pressure, temperature and WVP changes to the refractivity.

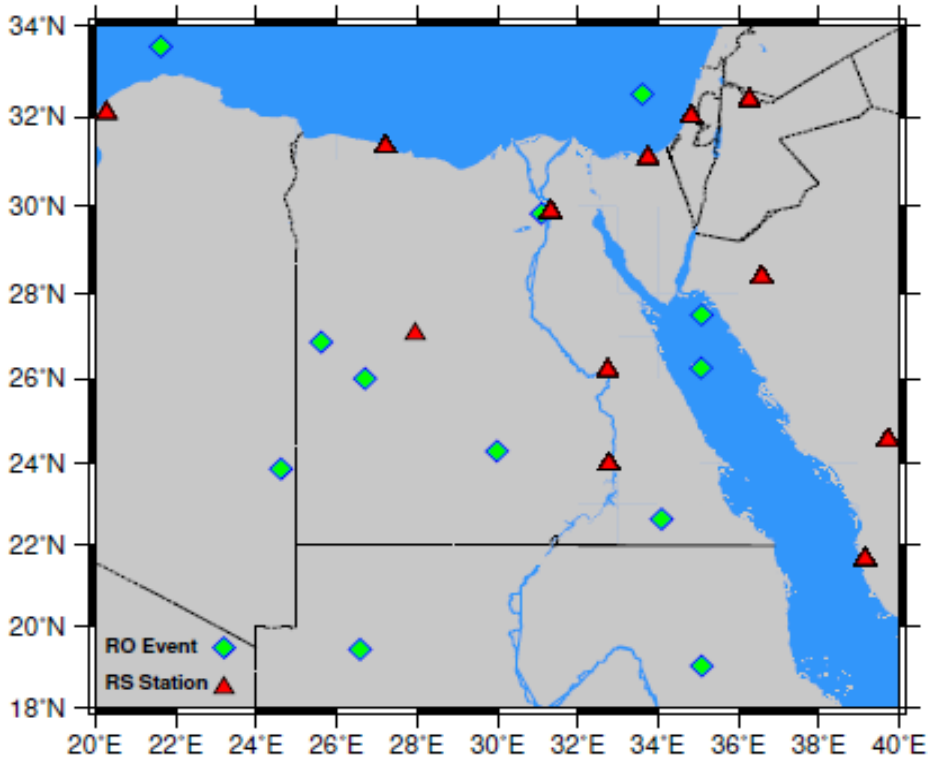

Fig. (3.3): Distribution of RS stations and ROEs in Egypt on JD = 2456940.

3.3 Zenith Delay Calculation

The troposphere causes a delay to the signal Δ^{PD} which can be expressed as an integral of the total refractivity N along the propagation path s from receiver r to the satellite w as indicated in equation (3.4) (e.g., Mendez Astudillo et al., 2018).

$$\Delta^{PD} = 10^{-6} \int_r^w N \, ds \tag{3.4}$$

The tropospheric delay can also be separated in the hydrostatic and

the wet component. Therefore, Equation (3.4) can be written as indicated in equation (3.5).

$$\Delta^{PD} = 10^{-6} \int_r^w N_{dry}\, ds + 10^{-6} \int_r^w N_{wet}\, ds \quad (3.5)$$

The total tropospheric delay in slant path delay can be mapped to the zenith direction, yielding the ZTD using mapping function depending on the elevation angle of the satellite as indicated in equation (3.6). The ZTD is defined as the addition of the Zenith Hydrostatic Delay (ZHD) and the Zenith Wet Delay (ZWD) as indicated in equation (3.7):

$$\Delta^{PD} = \mathrm{ZHD} * \mathrm{m_h(E)} + \mathrm{ZWD} * \mathrm{m_w(E)} \quad (3.6)$$

$$ZTD = ZHD + ZWD \quad (3.7)$$

where $mh(E)$ and $mw(E)$ are the hydrostatic and wet mapping functions depending on the elevation angle E. The ZTD can be determined as an integral of N in the zenith direction as indicated in equation (3.8) (e.g., Mendez Astudillo et al., 2018):

$$ZTD = 10^{-6} \int_0^{zenith\ path} N\, ds \quad (3.8)$$

3.4 Differences in ZPD between RO, RS and GPS-PPP

The present research estimates the ZHD, and ZWD using RO and RS and get the GPS-PPP processing results zenith path delay to inspect the ability of refinement delay estimation using precise observations. Besides RO-RS atmosphere profiles comparison, the zenith delay is compared to know the impress of using and integrating RO data in delay estimation.

3.4.1 RO ZPD

RO pressure, temperature, WVP and refractivity profiles data are

given for 40 km total height distance and every 100 m equal distances by a total number of 400 observations for each parameter profile. To enhance the accuracy, LAGRANGE interpolation method is used to interpolate pressure and WVP data every 25 m in height to be 1600 observations in each profile, also, linear interpolation is used in the other parameters. Because of lack of data in the first 1 to 3 km range, data extrapolation is used by the same methods.

Three types of refractivity are used in RO-ZPD calculation. Refractivity based on pressure, temperature and WVP using equation (3.3) which called "calculated refractivity". Analyzed and observed refractivity are offered in RO data files. Analyzed refractivity is based on the other meteorological parameters and the observed one is calculated directly from the GPS-LEO path delay.

Using the refractivity, the ZHD and the ZWD are calculated using general equation (3.7 and 3.8). To apply the integration using the RO refractivity observations every 25 m height, equation (3.9 and 3.10) is used to find the path delay values in the present research.

$$ZHD = \frac{10^{-6} * 25}{2}(N_{dry\,1} + N_{dry\,1600} + 2*(N_{dry\,2} + .. + N_{dry\,1599})) \qquad (3.9)$$

$$ZWD = \frac{10^{-6} * 25}{2}(N_{wet\,1} + N_{wet\,1600} + 2*(N_{wet\,2} + .. + N_{wet\,1599})) \qquad (3.10)$$

3.4.2 RS ZPD

Three differences between RO and RS data format which change analysis procedures. RS data file contains all RS stations for a certain period (one year), however, each observation profile in RO is in a single file. RS profile observations are not in equal distances but in equal pressure levels, so, interpolation methods mentioned before are used in

height data uniformity. WVP is not given directly; however, the dew point depression is given to calculate the WVP from using equation (2.1 and 2.2). After overcoming the differences mentioned before, RS refractivity is calculated using equation (3.3) and it becomes ready to calculate the ZHD and ZWD from it using the equations (3.9 and 3.10) using the calculated refractivity based on observed parameters.

3.4.3 GPS CSRS-PPP ZPD

PPP is a positioning technique that removes or models GNSS system errors to provide a high level of position accuracy from a single receiver. A PPP solution depends on GNSS satellite clock and orbit corrections, generated from a network of global reference stations. Once the corrections are calculated, they are delivered to the end user via satellite or over the Internet. These corrections are used by the receiver, resulting in decimeter-level or better positioning with no base station required.

GNSS data is widely used for positioning and navigation in mass-market and engineering applications and for altitude determination, moreover, it can also be used for monitoring the atmosphere. The electron content in the ionosphere and the air density in the electrically neutral atmosphere (troposphere) affect GNSS signals propagating through the atmosphere. The influence of the troposphere is described by the total refractivity N, which depends on pressure, temperature, and water vapor partial pressure. An example of the use of GNSS data for applications other than positioning and navigation is the integration of the GNSS-derived Path Delay with microwave radiometer measurements to find a precise wet tropospheric correction for altimetric products (e.g. Fernandes et al., 2015).

Another use of GNSS data is the remote sensing of the atmosphere, where GNSS signals can be used to measure physical variables such as atmospheric temperature, pressure and tropopause heights needed for weather and climate change monitoring. Other examples are the measurement of the amount of precipitable water in the atmosphere using GPS signals as in the experiment GPS/MET (Bevis et al., 1994).

The amount of precipitable water can be estimated from the amount of water vapor in the atmosphere which is proportional to the ZWD, which is relevant to weather forecasting and the study of extreme weather phenomena. Moreover, three-dimensional water vapor can be reconstructed from GNSS observations from different systems (Dong and Jin, 2018).

The ZWD and the ZHD comprise the ZTD that can be estimated with the PPP technique. PPP estimates the tropospheric delay, the position and clock offsets using precise ephemeris and the ionospheric-free combinations of dual-frequency GPS pseudorange and carrier-phase observations (Heroux and Kouba, 2001).

Given the increasing attention of PPP among the GNSS community, different software packages have been developed. The precision of the positioning results can be assessed, for example, the online PPP solution by the University of New Brunswick (GAPS) has been evaluated in terms of its achievable accuracy (Urquhart et al., 2014). An overview of GNSS data analysis capabilities that can be implemented in PPP software GAPS has been investigated (Leandro et al., 2011). Moreover, the analysis of the accuracy of the position determination using single-receiver GNSS measurements with different observing conditions using the online software CSRS-PPP has been investigated (Dawidowicz and Krzan, 2014).

In terms of the use of GNSS data for meteorology, the results of the Integrated Water Vapor (IWV) estimated from GPS and Galileo observables have been compared with the results obtained with a RS (Mendonca et al., 2016) and it was concluded that the Galileo-GPS IWV estimates are close to those of GPS-only at a level of 0.13 kg/m2 of perceptible water.

Studies about estimated ZTD with PPP are scarce, the results of estimated ZTD with the Automatic Precise Positioning Service (APPS), the GPS Analysis and Positioning Software, CSRS-PPP, and the Magic-PPP online PPP software have been compared to assess the quality of positioning estimation (Guo, 2015). The suitability of real-time ZTD estimates obtained from three different PPP software packages, the PPP wizard, developed by the University of Luxembourg, the Tefnut application developed by the Geodetic Observatory Pecny and the BKG Ntrip Client developed by the Bundesamt fuer Kartografie und Geodaesie, (all of them capable of performing PPP in real time) has been assessed by comparing them with the International GNSS Services (IGS) final troposphere product as well as with collocated RS observations. The motivation for such assessment was to find which precise ZTD estimates can be used in Numeric Weather Prediction models (Ahmed et al., 2014). However, there has been no assessment on the quality of ZTD-estimates using data from stations in different latitudes and in the four seasons using both, online and post-processing PPP software packages. Also, the quality of ZTD-estimates obtained with the software developed by the University of Nottingham (POINT) has not yet been assessed.

CSRS-PPP is an online application for GNSS data post-processing. It uses precise satellite orbit, clock and bias corrections derived from a

global network of receivers to determine accurate user positions anywhere on the globe, regardless of proximity to reference stations. Submit RINEX format observation data from single or dual-frequency receivers operating in static or kinematic mode over the Internet, and recover enhanced positioning precisions in the North American Datum of 1983 of NAD83-CSRS or the International Terrestrial Reference Frame (ITRF). By sending observation RINEX file to CSRS-PPP website, processing results directly sent to E-mail. Each observation solution contains five solution data files which have the following description besides the output description file and the pdf summary file. "SUM" file which contains the parameters and the results of the PPP processing. "POS" file which contains the positioning information for each epoch processed. "CSV" file which a comma-separated (.csv) format text file containing positioning and clock information for each epoch processed. "TRO" file which contains dry and wet zenith path delay and tropospheric gradient for each epoch processed. "CLK" file is a RINEX_CLOCK format file containing the receiver clock offset and the clock offset sigma (95%) for each epoch processed.

Troposphere zenith delay (TRO) file contains the following data: SITE which indicates the station name, "EPOCH" which indicates the Observation Date (yy:doy:ssss), "TRODRY" which indicates the dry zenith path delay [mm], "TROWET" which indicates the estimated wet zenith path delay [mm], "STDDEV*" which indicates the standard deviation (95%)of the estimated Wet zenith delay [mm], "TGNTOT" which indicates the estimated north tropospheric gradient [mm], "STDDEV" which indicates the standard deviation (95%) of TGNTOT [mm], "TGETOT" which indicates the estimated East tropospheric gradient [mm], "STDDEV*" which indicates the standard deviation (95%)of TGETOT [mm].

The CSRS-PPP uses a dynamic filter to estimate the station position in static or kinematic mode, the station-clock states, the local tropospheric zenith delays and the carrier-phase ambiguities. The approach used in CSRS-PPP for ZTD estimation is to smooth the estimates by a backward substitution with the final converged satellite ambiguity parameters held fixed for all epochs. This approach is implemented to obtain optimal station Zenith Path Delay time series based on all observations within the observation session. Precise corrections to orbits and clocks of satellites used are made available by the IGS. The mapping function used in CSRS-PPP is the Global Mapping function. As an input, single or dual-frequency GNSS data can be used. The user may choose NAD83 or ITRF2008 frame of reference to determine coordinates (Heroux and Kouba, 2001).

Functions that map slant measurements to the local zenith are used to estimate ZTD with good accuracy, a prime example being VMF1, the Vienna Mapping Function 1 (Dong and Jin, 2018). For high-accuracy PPP solutions, it is necessary to separate the ZHD and ZWD components due to the differences in hydrostatic and wet mapping functions at lower elevation angles. PPP software generally estimates and outputs ZTD and its two components, ZHD and ZWD. Typically, the more predictable ZHD values are modelled, while the remainder is estimated as ZWD. The separate estimation of ZWD parameters is valuable for numerical weather prediction (NWP) algorithms as it can be used to determine water vapour content in the troposphere above the receiver. The two-sigma accuracy estimates of IGS-derived ZTD values at IGS stations using continuous 24 h data segments are of the order of 2 mm to 8 mm and a function of various factors, e.g., regional satellite geometry and environmental obstructions at the station sites.

ZHD is about 90% of the delay; this part can be modeled using mathematical models. ZWD is unpredictable; it depends on water vapor and is typically less than 30 cm (Hofmann-Wellenhof et al., 2008). The reference system for the CSRS-PPP software is based on ITRF 2014; the obtained coordinates have Cartesians XYZ format and Ellipsoidal/Universal Transverse Mercator (UTM) system. The IGS final ephemerides are used during processing with a satellite orbit of a 15-min interval and a satellite clock of a 30-s interval.

The ionospheric delay is eliminated for dual-frequency data using the ionospheric-free linear combination, and the second-order errors are equally considered. For single-frequency data, the ionospheric delay is modeled using the final Global Ionospheric Maps (GIM) from IGS. Regarding the tropospheric delay, the processing tool that is based on the Global Pressure and Temperature (GPT) model uses the Davis model for the hydrostatic delay. For the wet part, the processing mechanism uses the Hopfield model that is based on the GPT model. In addition, the VMF1 is utilized (Boehm et al., 2006).

3.5 ZPD Relations with Time and Other Meteorological Parameters

Based on eleven years (2010-2020) of RO data, ZHD and ZWD relations with pressure, temperature and WVP are indicated. The corresponding meteorological data are charted with delays to find the relations, if exist. Each meteorological parameter is put on the independent axe with the delays in the dependent axe to study the regression. Finding the key parameters for ZTD model was the first idea but as mentioned before the ZWD represents a non-expectable parameter. So, the impact of each parameter on the delay values was preferred.

Pressure is one of the important parameters that has a great impact

on the delay values. Knowing the nature of the relation between pressure and delay values is very important matter. Finding and testing a linear regression equation between the pressure and delay values based on eleven years of data will contribute by a big share in understanding the pressure delays relations. Moreover, temperature and WVP impact on delay values is examined to get the key parameters affecting the delay values.

ZHD and ZWD trends, cycles and season time series are made using the RO data. Also, time series parameters are calculated for each meteorological parameter. Delay changes in time series values will be reasoned and commented. Meteorological changes though eleven years of data are studied to check the reason of each parameter change. Topographic maps for delay values and meteorological parameters are produced to know the 2D changes for each parameter on map. Easing and northing (represented in longitude and latitude) changes in delay values and meteorological parameters are studied through Egypt borders.

CHAPTER 4

RESULTS AND DISCCUSION

Chapter 4 : Results and Discussion

In this chapter, the results of the RO-RS profiles difference analysis will be represented and discussed. Additionally, the statistical analysis for the differences between the RO and the RS profiles will be demonstrated. Besides, ZPD components values for the RO, RS and the GPS-PPP will be compared. ZPD regression analysis results with the different meteorological parameters will be clarified also and tested. A model combining each meteorological parameter with delay values will be constructed, validated and verified. In addition, time series for ZPD and the other parameters is showed besides, the ZPD and meteorological parameters spatial distribution maps.

4.1 RO-RS Single Profile Comparison

This section shows the profiles comparison between the RO and the RS methods. Spatial and temporal differences are taken in consideration in profiles comparison. Fig. (4.1) shows the comparison profiles (3~25 km in altitude) between RO and RS data in pressure, refractivity, temperature and WVP for point (1, 2, and 3) indicated before (Fig. 3-3). Comparison profiles indicated that the difference in pressure, refractivity and temperature seems to be very small for the different methods. The three points of comparison pressure and refractivity profiles are very identical as indicated in Fig. (4.1a, 4.1b). Temperature profile also is so far identical except some portions don't exceed 3.4 km in altitude and approximately 1 degree in temperature difference as indicated in Fig. (4.1c). On the other hand, Figs. (4.1d ~ 4.1f) show the comparison profile of WVP in the points (1, 2, and 3), respectively. It showed that the WVP profile is not identical at most of the profile length. Although the difference does not exceed the unity, it is salient as the small values of WVP profiles.

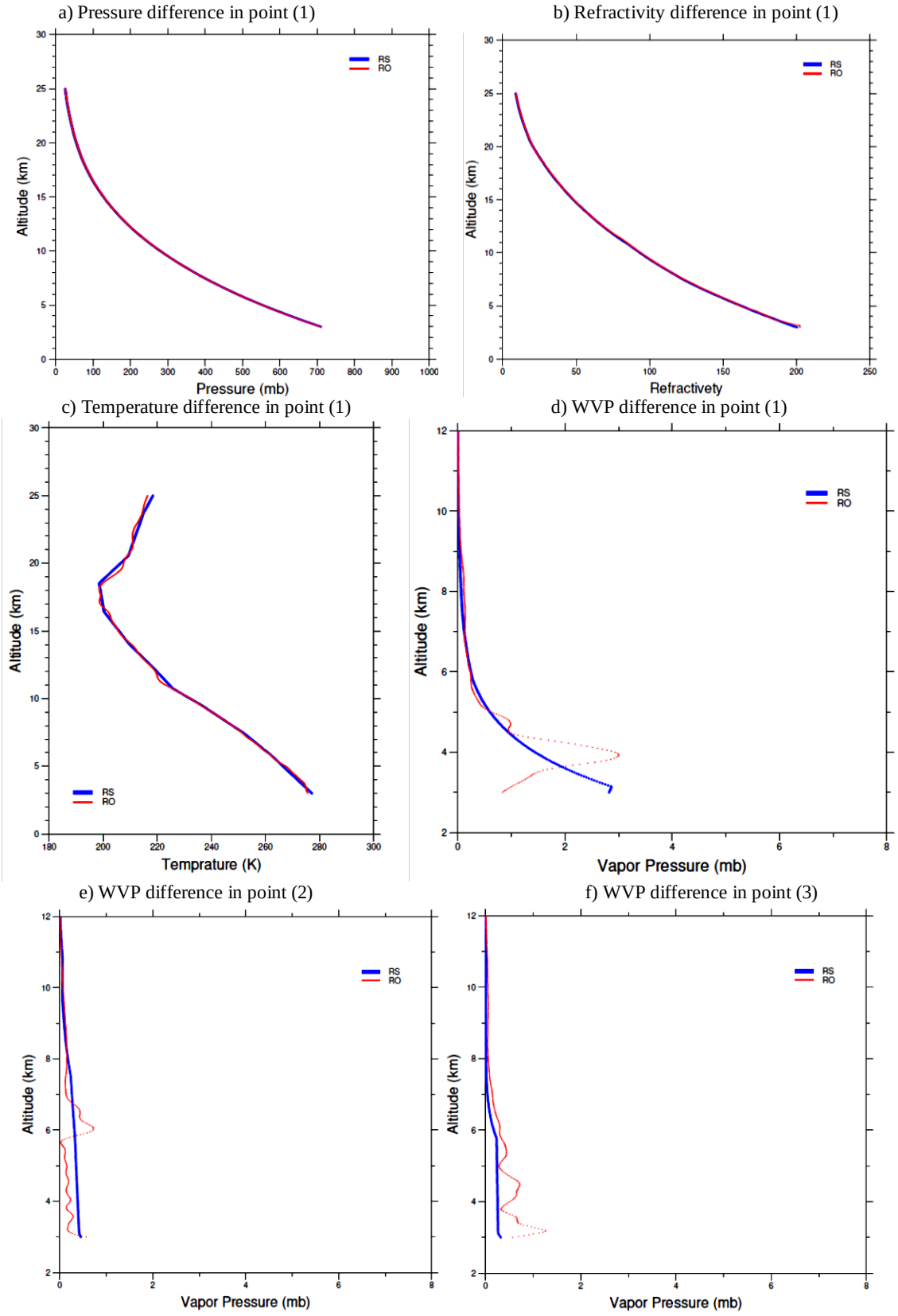

Fig. (4.1): Comparison profiles between RO and RS data.

Table (4.1) lists the mean and standard deviation (SD) for the absolute difference values along the RO-RS profiles for the three check points. The pressure, temperature, WVP and refractivity mean absolute difference and SD are insignificant except the WVP difference for the point 1. Mean absolute difference value of 0.139 mb and SD of 0.102 mb are considered big values comparing with the small values of WVP profiles.

Table (4.1): Mean absolute difference and St. Dev. for the three RO-RS check points.

Variable	Point1		Point2		Point3		Mean		Relative Error %
	Difference	SD	Difference	SD	Difference	SD	Difference	SD	
Pressure (mb)	0.708	0.025	0.651	0.014	0.433	0.009	0.60	0.016	0.3
Temperature (K)	0.527	0.015	1.153	0.047	0.697	0.021	0.79	0.028	1.7
WVP (mb)	0.139	0.102	0.073	0.04	0.095	0.007	0.10	0.050	62
Refractivity	0.556	0.052	0.479	0.015	0.392	0.019	0.48	0.029	0.7

According to the mean absolute difference for the three points, pressure, temperature, WVP and refractivity difference are 0.6 mb, 0.79 deg, 0.1 mb and 0.48 and these are considered small values. The mean difference for the three points is divided by the mean of the three points observations in pressure, temperature, WVP and refractivity as a relative error and showed as a percentage in table (4.1). The difference percentages are 0.3%, 1.7%, 0.7% in pressure, temperature and refractivity, respectively and these relative errors are considered small values. The difference percentage for the WVP is 62% and to justify this difference, an affirmative step was done using the ECMWF model. Pressure values don't have a big change by varying the easting or the northing up to 100 km or varying the time up to 6 hours. By changing the easting or the northing up to 25 km, the vapor pressure values change exceeding 1 mb especially at

low altitudes that affect the wet delay values.

Statistical correlation test was also done to check the correlation between the RS and the RO observations profiles and all observed correlation factors gave values not less than 0.99. All RO-RS profiles differences are in the reasonable range.

A T-test is made to check if there is a significant difference between each two RO-RS variable profiles or not. Two samples assuming equal variance T-test were made using a probability of 95% between each RO-RS pressure, temperature, WVP and refractivity profiles for each of the three check points. Using a significance level (α=0.05) and a two-tailed T-test, the t, P-value and the critical t-value are as listed in Table (4.2).

Table (4.2): T-test results for the three RO-RS check points.

Check Point	Variable	t value	P value	t Critical
Point (1)	**Pressure (mb)**	0.0340	0.9729	1.9613
	Temperature (K)	0.0023	0.9981	1.9613
	WVP (mb)	-0.1148	0.9087	1.9622
	Refractivity	0.0405	0.9677	1.9613
Point (2)	**Pressure (mb)**	-0.0653	0.9479	1.9613
	Temperature (K)	0.3281	0.7429	1.9613
	WVP (mb)	3.9667	0.0001	1.9622
	Refractivity	-0.0473	0.9623	1.9613
Point (3)	**Pressure (mb)**	0.0131	0.9895	1.9613
	Temperature (K)	-0.061	0.9514	1.9613
	WVP (mb)	8.2137	0.0000	1.9623
	Refractivity	0.1319	0.8951	1.9613

As listed in Table (4.2), all t values for all meteorological variables are less than t critical value except the WVP test for points (2 and 3) that insures privation of significant differences between RO-RS profiles in pressure, temperature, and refractivity. Moreover, the P value is more than 0.05 except the same tests. As mentioned before and as a reference to the ECMWF model, the WVP changes significantly with a spatial or temporal difference of the observations. As a result, the T-test results are accepted, reasonable and expected. For the WVP difference, although the mean absolute of point (1) difference gave a value bigger than points (2 and 3), the opposite happened in the T-test results as the mean in T-test taking the observations sign along the profile in consideration. So, pressure, temperature and refractivity difference are statistically insignificant. However, the difference in WVP is statistically significant.

4.2 RO-RS Data Difference Analysis

All RO-RS matched profiles in or around Egypt borders are analyzed in this section. Matched profiles are divided according to the distance between RO-RS observations and the difference in time between them. Difference refers to RS observations minus RO observations at the same altitude. Check points are divided to three groups depending on time and distance between RO and RS observations as indicated in Fig (6). Group (1) (G1) include difference between observations that have difference in time of 20 minutes and in distance of 20 km. G2, and G3 also have a difference of 40 Min, 60 km in time and distance, respectively. Orange, red, and blue points refer to G1, G2, and G3, respectively.

Pressure graph in Fig. (4.2) shows that the G1, G2, and G3 have an absolute difference not exceeds 4, 8, 10 mb. Pressure difference is directly proportional to the pressure values as at low altitudes, pressure difference

has larger values comparing with high altitudes. Higher than 20 km altitudes, the pressure difference of some profiles deviate because of the shortage in RS pressure profile at these profiles. Minimum difference values are at altitude of 20 km. Under 3 km, the pressure difference has values exceed 12 mb in G3 observations.

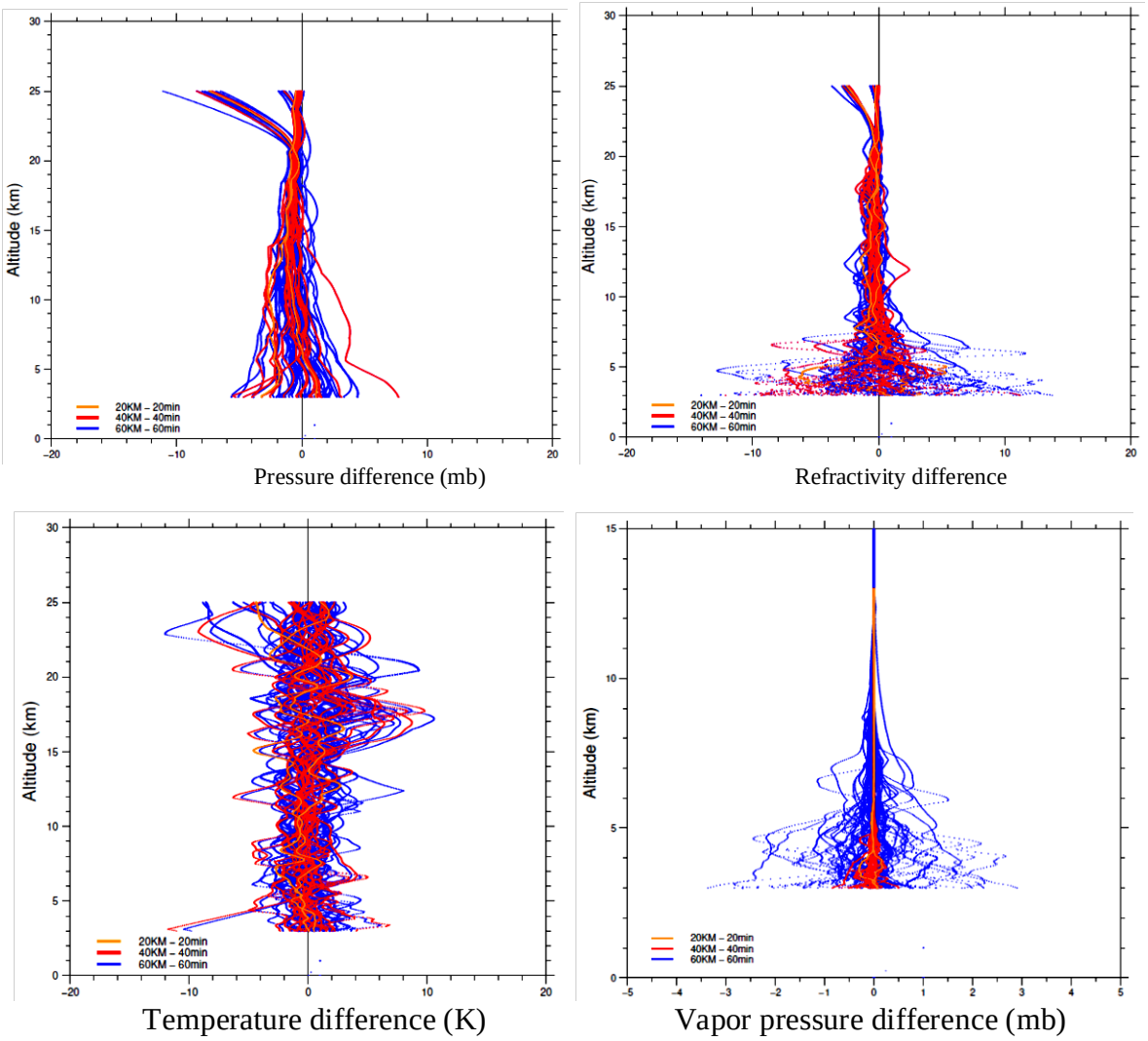

Fig. (4.2): RO-RS observations difference.

Unlike the other difference profiles, temperature differences do not decrease with altitude as indicated in temperature graph in Fig. (4.2). Some of its differences reach a value of 10 degrees but most of them do not exceed 6 degrees. G1, G2, and G3 absolute differences do not exceed 2, 8, 11 degrees, respectively. Under 5 km and above 20 km some of

difference profiles give large values resulted from the shortage in RS profiles in low and high altitudes and in RO profiles in low altitudes only. As well, WVP graph shows that the G1, G2, and G3 have an absolute difference not exceeds 0.5, 1, 3 mb.

Refractivity difference profiles include indirectly pressure difference and WVP difference. Refractivity graph in Fig. (4.2) shows that the G1, G2, and G3 have an absolute difference not exceeds 6, 8, 12 by an absolute average equal 1, 2, 4. Up to seven kilometers, refractivity difference has a big value as it depends on pressure and WVP difference at these altitudes and they have bigger values comparing to the remaining profiles.

Table (4.3) lists the mean of the absolute difference values, the Mean Standard Deviation (MSD) and the number of check points used in analysis for each group. The maximum means for the absolute difference values are 1.049 mb, 1.33 deg, 0.211mb and 0.796 for pressure, temperature, WVP and refractivity, respectively. Furthermore, the maximum MSD values shown in Table (4.3) are not considered small. It is perceived that the mean difference and the MSD are increasing directly with time and distance difference in most of meteorological variables.

Fig. (4.3) shows the Root Mean Square (RMS) and the absolute difference in a group of check points. It is calculated by taking the square root for the summation of the square of difference values for each variable. However, the absolute value is average for the difference values without sign. Check points that have a time difference did not exceed 20 minutes and a distance did not exceed 50 km between each RO and RS observation are shown in Fig. (4.3a). Fig. (4.3b) shows the difference between observations difference that did not exceed 40 minutes and 100 km in time

and distance, respectively.

According to Fig. (4.3a), RMS, Absolute graphs show the RMS, mean absolute value for 21 check points. The RMS, mean absolute values of the pressure, temperature and WVP decrease by going up except over 20 km. The profiles of RMS and mean absolute difference in temperature increase slightly by going up. According to Fig. (4.3-b), RMS, absolute graphs show the RMS, mean absolute value for 133 check points. On the other hand, the RMS, mean absolute values of the pressure, temperature and WVP decrease by going up except over 16 km it increases.

Table (4.3): Mean absolute difference, SD, and number of check points for each group.

Difference	Variable	Difference	St. Dev.	No. of Check Points
20 Min, 20 km	**Pressure (mb)**	1.020	0.018	2
	Temperature (K)	1.201	0.031	2
	WVP (mb)	0.196	0.011	2
	Refractivity	0.685	0.036	2
40 Min, 40 km	**Pressure (mb)**	1.049	0.023	18
	Temperature (K)	1.291	0.041	18
	WVP (mb)	0.202	0.011	18
	Refractivity	0.749	0.038	18
60 Min, 60 km	**Pressure (mb)**	1.023	0.026	58
	Temperature (K)	1.333	0.041	58
	WVP (mb)	0.211	0.011	58
	Refractivity	0.796	0.039	58

a) 20 min and 50 km

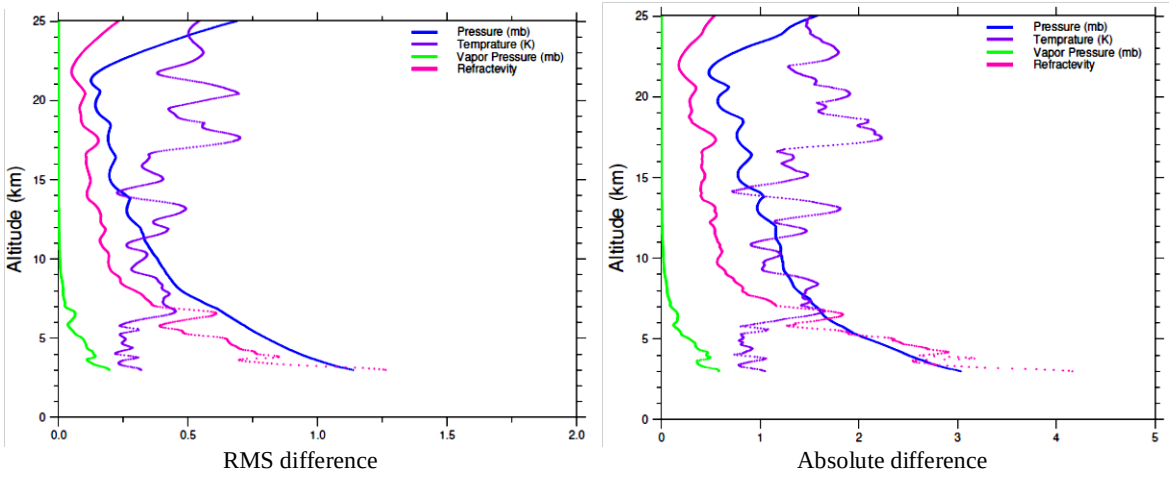

b) 40 min and 100 km

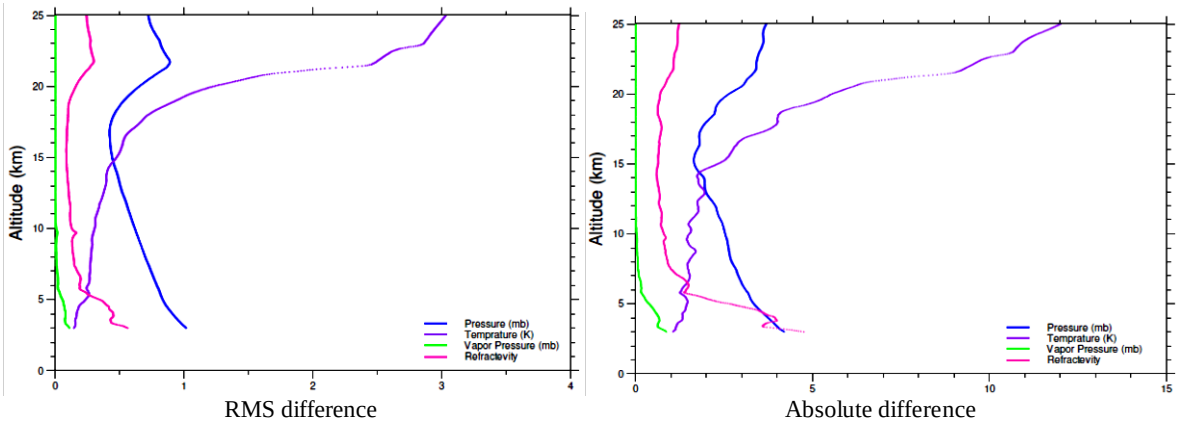

Fig. (4.3): RO-RS observations RMS and mean absolute Difference.

Only temperature RMS, mean absolute difference profile increase by going up. By increasing the time and distance difference in Fig. (4.3a, 4.3b), the difference profiles became smoother, difference values increased slightly comparing with the difference in time and distance. The temperature difference increased significantly above 15 km. The reason of increasing the temperature difference after 15 km is the big deviation in RS balloon path which reaches 100 km in some cases. Temperature and WVP are the parameters that may be affected directly by balloon deviation but the WVP profile observations not exceed 12 km height so the temperature is the only parameter that may be affected. All the difference

values mentioned in this section are reasonable and intelligible and as a result depending mainly on RO and RS data and making data integrating models in Egypt between them is a logic and applicable process.

Table (4.4) lists the mean absolute and the RMS for the difference values with a difference in time and distance of 20 Min, 50 km and 40 Min, 100 km. The mean absolute for 40 Min, 100 km check points have the maximum difference values and MSD for all meteorological variables. These difference values are 2.7 mb, 3.8 deg, 0.3 mb, 1.2 for pressure, temperature, WVP and refractivity, respectively. Besides the small values of MSD, the RMS is less than the mean absolute in all cases and this is another indicator of small differences between difference values as the difference is squared in the RMS that grow up the differences between difference values.

Table (4.4): Mean absolute difference, RMS, SD, and number of check points for each group.

	Difference	20 Min, 50 km		No. of Check Points	40 Min, 100 km		No. of Check Points
	Variable	Difference	St. Dev.		Difference	St. Dev.	
Mean absolute	Pressure (mb)	1.182	0.019	21	2.695	0.023	133
	Temperature (K)	1.397	0.012	21	3.842	0.112	133
	WVP (mb)	0.222	0.015	21	0.256	0.021	133
	Refractivity	0.796	0.026	21	1.153	0.029	133
RMS	Pressure (mb)	0.390	0.008	21	0.655	0.006	133
	Temperature (K)	0.412	0.004	21	0.888	0.031	133
	WVP (mb)	0.049	0.009	21	0.035	0.006	133
	Refractivity	0.237	0.007	21	0.183	0.004	133

To inspect the degree of significance in refractivity values resulted

from pressure, temperature and WVP difference, a T-test and the correlation were studied. The T-test results showed that changing 0.1 in pressure, temperature or WVP values (each by its unite) affect significantly the refractivity value. As well, there is a great correlation between each of atmospheric parameter difference and the refractivity. As a result, all of pressure, temperature and WVP differences mentioned above in this section are considered statistically significant to the refractivity.

Generally, the difference values in each of the single profile comparison and the spatial and temporal difference analysis may be due to spatial and temporal difference in observations, although, they are bit bigger than the normal rate. Also, the excess of the normal difference may be resulted from the row observation data interpolation and extrapolation in different portions in the different methods.

4.3 LEO Satellites Difference Analysis

As mentioned before, COSMIC, GRACE and C/NOFS are only the LEO missions that located observations fit to be a check point. Each satellite observations difference is inspected in this section to be able to analyze LEO mission differences in Egypt. The big differentiation in LEO difference profiles insures depending difference values on LEO mission. This section enables us to assess the LEO missions that have check points matches RS missions in time and distance like mission mentioned before.

Fig. (4.4) shows the RMS difference for the pressure and temperature. Pressure and temperature graphs show that GRACE2, 1 and COSMIC3 have the biggest difference values, respectively. COSMIC1, 2, 4, 5, 6 almost have the same and the best difference profile with slight

differences. GRACE2 pressure and temperature difference profile is the worst and as a result the degree of confidence in its data is very low comparing with the other missions. C/NOFS mission has data limitations as its difference profile changes significantly with altitude and temperature difference profile changes more significantly than the pressure one. Although COSMIC3 has a slight big value of pressure difference but being over 20 km decrease its impact. As a result, COSMIC by its six satellites data has the best degree of confidence compared with GRACE and C/NOFS satellites data. As it is mentioned above, temperature difference increases significantly with altitude on the contrary with pressure difference profiles.

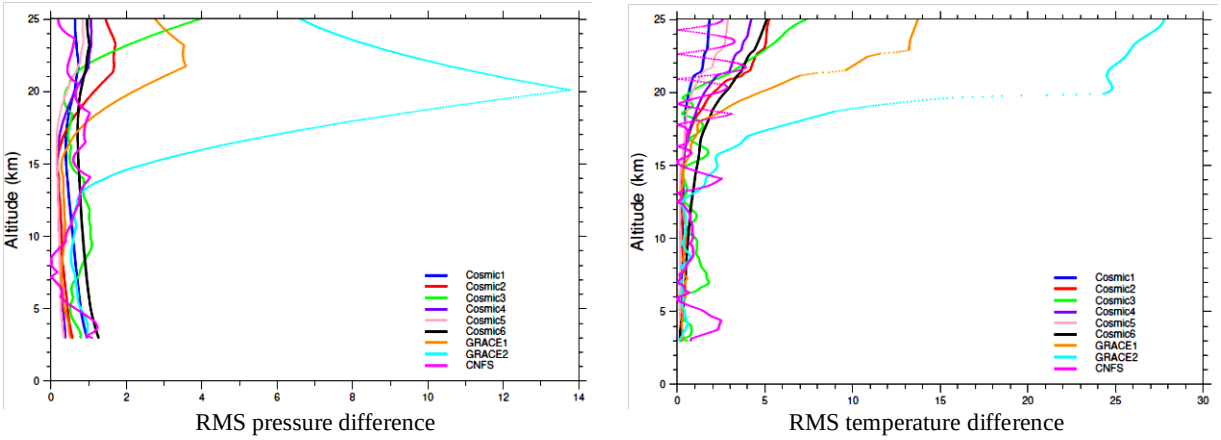

Fig. (4.4): RO-LEO mission observations difference.

All of cosmic and C/NOFS pressure RMS differences are less than the unit. Furthermore, the temperature RMS differences for them are less than two degrees that ensures the high accuracy of these mission and high capability of taking advantage of them in Egypt. COSMIC 3, 6 give little bigger RMS differences than the other COSMIC and C/NOFS satellites. Generally, GRACE 1, 2 gave little big RMS difference values in pressure and temperature and GRACE 2 is the bigger in RMS difference values so it is a must to be careful when using its data in Egypt. According to

relative error values, GRACE2 gave a relative error value of 1.96% in pressure and 16.26% in temperature and these are considered big relative errors especially for temperature. COSMIC 3, 6 and GRACE1 also gave temperature relative errors exceed 3% which considered big percentage.

4.4 Upper Air Stations Difference Analysis

To assess the difference values for each of RS stations, the RMS difference values are estimated for each upper air stations separately based on the check points match their missions time and location.

Fig. (4.5) shows the RMS difference values for each of RS station. Differentiation in RS RMS difference profiles insures the dependence of the difference values on the RS observations as well. Like other difference profiles, pressure and temperature difference values increase by going up. Difference profiles for all of RS stations located inside Egypt are not significantly big except South of Valley which has difference in temperature exceeded 10 degrees in an altitude more than 20 km. It is clear that Benina RS station has great difference values in pressure and temperature so it is a must to adjust the observation methods in it.

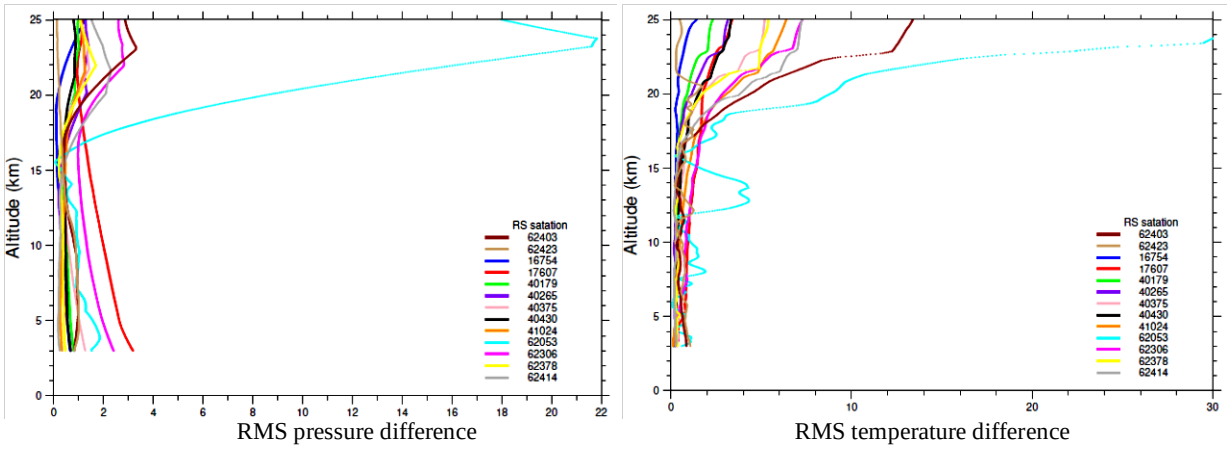

Fig. (4.5): RS stations observations difference.

Station Benina has the maximum RMS difference value and MSD in

pressure and temperature. Although the number of check points in this station is two check points only, it is still having a big difference value leads to data confidence degradation. Stations Athalasa, Mersa Matruh and South of Valley have the second level of confidence and the remained stations have the first degree as the difference values did not exceed the unity in pressure and 2 degrees in temperature. The pressure and temperature relative errors for station Benina are 2.3%, 12.58%, respectively. These are big relative errors. For the other stations, the pressure relative error is small but for the temperature, Athalasa, Mersa Matruh and South of Valley give bigger values. These big difference values for temperature may be caused by the observation temporal and spatial difference besides the deviations happening in balloons direction and RO profiles in the original cases.

4.5 ZPD Differences between RO, RS and PPP Data

Finding the delay values produced from RO and comparing with the RS and the GPS-PPP delay values ensure the validation of the RO method in atmosphere identifying. ZPD is calculated from the RO and RS observations and compared with each other and with PPP ZPD. Check points are chosen within temporal and spatial tolerance up to 60 minutes and 100 km, respectively.

Fig. (4.6) shows ZHD for 17 check points. Year, DOY, LEO satellite, RS station, RS/GPS station, spatial and temporal difference are indicated in a table under each check point. As indicated before, one delay value for RS data, three for RO data and one for PPP analysis. As the DOY is different for the different points, each point could be identified using its DOY. Point 2011.235 has a mistake in its RO analyzed refractivity profile which made a big difference in delay values. Also, for

the same point, the calculated and the observed refractivity have big differences from the RS and PPP delay values. This means big differences in observed refractivity, pressure, WVP and temperature. In addition, point 2014.337 has a mistake in its RS profile data which made a big difference in delay values.

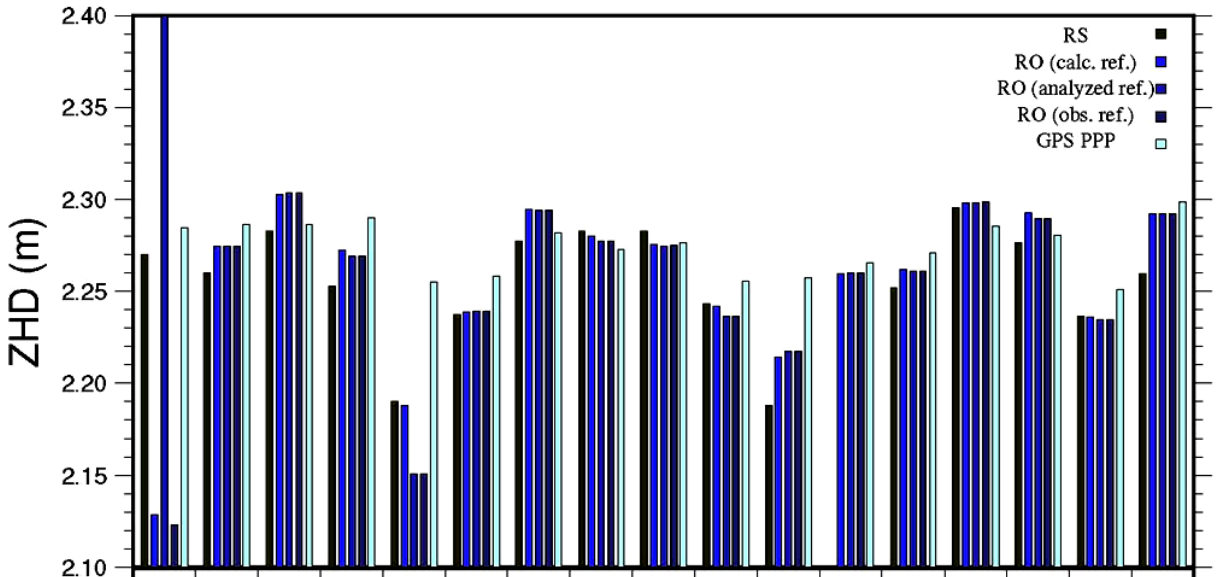

Year	2011	2011	2012	2012	2014	2014	2014	2014	2014	2014	2014	2014	2015	2015	2015	2015	2019
DOY	235	247	015	168	027	064	146	178	282	317	319	337	003	014	110	290	056
LEO Sat.	CMC6	CMC2	CMC5	CMC4	CMC4	CMC5	GRC1	CMC1	CMC6	GRC2	GRC2	GRC2	CMC1	CMC1	CMC5	CMC5	CMC6
RS/GPS St.	MRSA	MRSA	PHLW	PHLW	ASWN	ASWN	PHLW	PHLW	PHLW	ASWN	ASWN	ASWN	ASWN	PHLW	PHLW	ASWN	MRSA
Dist. (km)	97	66	93	97	62	87	91	92	22	98	65	73	89	56	65	68	26
DT (min)	36	28	2	52	34	34	57	46	14	35	32	51	59	56	25	42	32

Fig. (4.6): ZHD for RS, RO, and PPP.

Excluding these observations was discussed, but (as a random sample) this observation may express a lot. Points 2014.027 and 2014.319 have big mean difference values of 5.5 cm and 3.1 cm. As for RS/GPS station, both the two points are related to ASWN station. According to LEO satellite, they are related to CMC4 and GRC2, respectively.

Fig. 4.7 show the differences between the three methods in ZWD. It is easily seen that point 2014.337 has big difference value. Also, 2015.290 and 2014.319 have mean big difference value of 5.2 cm and 3.8 cm in

ZWD values respectively. These big differences may be due to the LEO satellite itself as the second point for GRACE2 which have untrustworthy results as mentioned before in section 4.3. The first point is resulted from COSMIC5 LEO satellite. The spatial and temporal differences which reach 100 km and 60 minutes, respectively, may cause such big differences. The diffraction of RO profile with the altitude may cause differences in results especially is it is in reverse of the observations spatial difference.

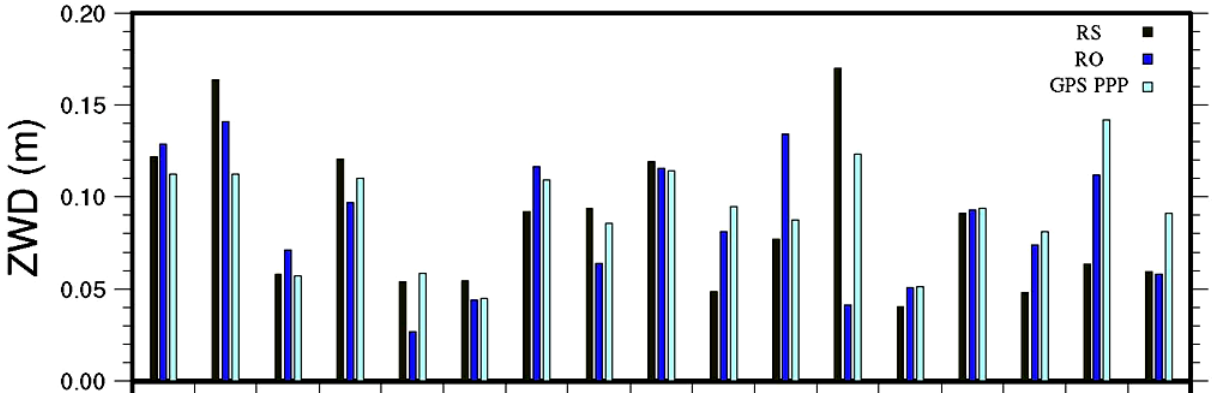

Year	2011	2011	2012	2012	2014	2014	2014	2014	2014	2014	2014	2014	2015	2015	2015	2015	2019
DOY	235	247	015	168	027	064	146	178	282	317	319	337	003	014	110	290	056
LEO Sat.	CMC6	CMC2	CMC5	CMC4	CMC4	CMC5	GRC1	CMC1	CMC6	GRC2	GRC2	GRC2	CMC1	CMC1	CMC5	CMC5	CMC6
RS/GPS St.	MRSA	MRSA	PHLW	PHLW	ASWN	ASWN	PHLW	PHLW	PHLW	ASWN	ASWN	ASWN	ASWN	PHLW	PHLW	ASWN	MRSA
Dist. (km)	97	66	93	97	62	87	91	92	22	98	65	73	89	56	65	68	26
DT (min)	36	28	2	52	34	34	57	46	14	35	32	51	59	56	25	42	32

Fig. (4.7): ZWD for RS, RO, and PPP.

Table (4.5) shows the differences between ZPD values for different methods. The table shows the results of a T-test which made to find the degree of correspondence between RO, RS, and PPP ZPD values.

Mean differences in analyzed RO ZHD have difference from the other methods reach 9-10 cm because of the out-of-range point mentioned before. By excluding the out-of-range observation, all differences related to analyzed RO decreased a lot. Differences between the analyzed RO and RS, PPP, and observed RO are decreased to 2.4 cm, 1.9 cm, and 4.0 mm, respectively. The RO observed ZHD has a minimum value of 4.0 mm

difference from the RO calculated ZHD. The other differences range from 2.1 to 3.1 cm in ZHD and ZWD. The calculated RO results give small difference values from the RS and PPP analysis results in both of ZHD and ZWD and this supports its stand against the other two RO refractivity methods.

Table (4.5): ZPD differences (m) and T-test results for RS, PPP, and RO data.

Variable 1	Variable 2	Difference		t value	p value	T critical
		Mean	St. Dev.			
RS-ZHD	**RO(calc.)-ZHD**	0.028	0.012	0.753	0.457	2.037
RS-ZHD	**RO(analyzed)-ZHD**	0.1	0.077	1.202	0.238	2.037
	By excluding out of range obs.	0.024	0.01			
RS-ZHD	**RO(obs.)-ZHD**	0.031	0.012	0.491	0.627	2.037
RS-ZHD	**PPP-ZHD**	0.031	0.01	2.783	0.009	2.037
PPP-ZHD	**RO(calc.)-ZHD**	0.025	0.009	1.652	0.108	2.037
PPP-ZHD	**RO(analyzed)-ZHD**	0.095	0.076	0.846	0.404	2.037
	By excluding out of range obs.	0.019	0.006			
PPP-ZHD	**RO(obs.)-ZHD**	0.028	0.01	1.868	0.071	2.037
RO(calc.)-ZHD	**RO(analyzed)-ZHD**	0.09	0.086	1.071	0.292	2.037
	By excluding out of range obs.	0.004	0.002			
RO(calc.)-ZHD	**RO(obs.)-ZHD**	0.004	0.002	0.229	0.82	2.037
RS-ZWD	**RO-ZWD**	0.028	0.007	0.123	0.9	2.037
RS-ZWD	**PPP-ZWD**	0.022	0.005	0.453	0.653	2.037
PPP-ZWD	**RO-ZWD**	0.021	0.005	0.64	0.527	2.037

The T-test results listed in the same table shows that all delay values have not significant differences except for the RS-ZHD with the PPP delay values. According to the T-test, RO ZPD values have good concurrence

with RS delays and PPP results. Furthermore, the RO delays with each other have good fitness.

4.6 ZPD Differences between RO and PPP Data

As the GPS stations observe permanently, RINEX files have total day observation data. This prevented temporal tolerance between RO and GPS observation. The remained difference now is the spatial difference. By using 10 km spatial difference tolerance in picking RO data synchronized with GPS observations, 15 points were resulted as check points. Fig. (4.8) shows the ZHD for these points indicating the year, DOY, LEO satellite and GPS station in the table under the figure. The differences in delay values are bit smaller than mentioned in the previous section as the temporal and spatial difference are almost eliminated.

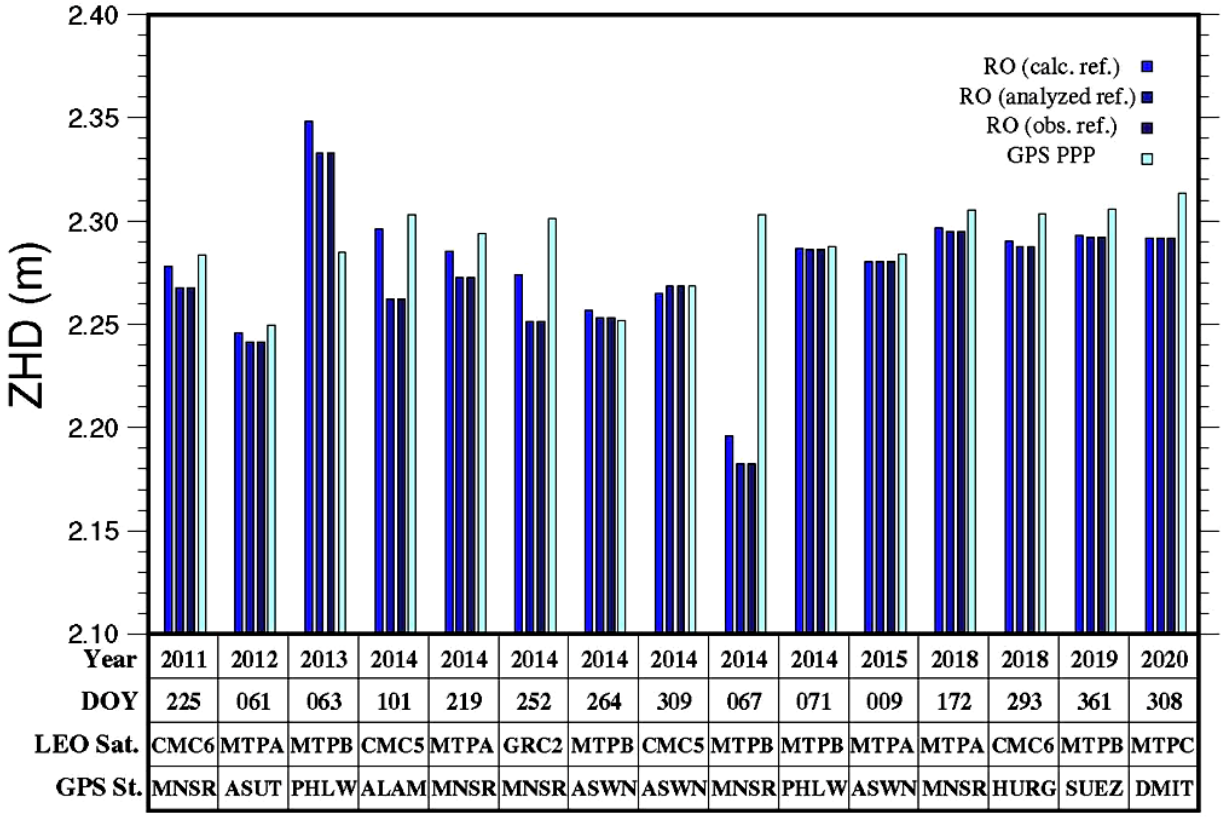

Year	2011	2012	2013	2014	2014	2014	2014	2014	2014	2014	2015	2018	2018	2019	2020
DOY	225	061	063	101	219	252	264	309	067	071	009	172	293	361	308
LEO Sat.	CMC6	MTPA	MTPB	CMC5	MTPA	GRC2	MTPB	CMC5	MTPB	MTPB	MTPA	MTPA	CMC6	MTPB	MTPC
GPS St.	MNSR	ASUT	PHLW	ALAM	MNSR	MNSR	ASWN	ASWN	MNSR	PHLW	ASWN	MNSR	HURG	SUEZ	DMIT

Fig. (4.8): ZHD for RO, and PPP.

Point 2014.067 has big differences in ZHD by a 7.5 cm mean

difference. Points 2014.252, 2014.101 and 2013.063 have bit smaller differences in ZHD than point 2014.067 by 3.5 cm, 3.1 cm, and 3.8 cm mean differences, respectively. As for GPS station, the three points are related to MNSR, ALAM and PHLW, respectively. According to LEO satellite, they are related to MTPB, GRC2, CMC5 and MTPB.

Fig. (4.9) shows the ZWD for check points indicating the year, DOY, LEO satellite and GPS station in the table under the figure. Points 2014.252, 2014.067 and 2018.172 have big difference values by 6.0 cm, 5.1 cm, and 3.6 cm, respectively. The difference values in the remained check points are under 3 cm.

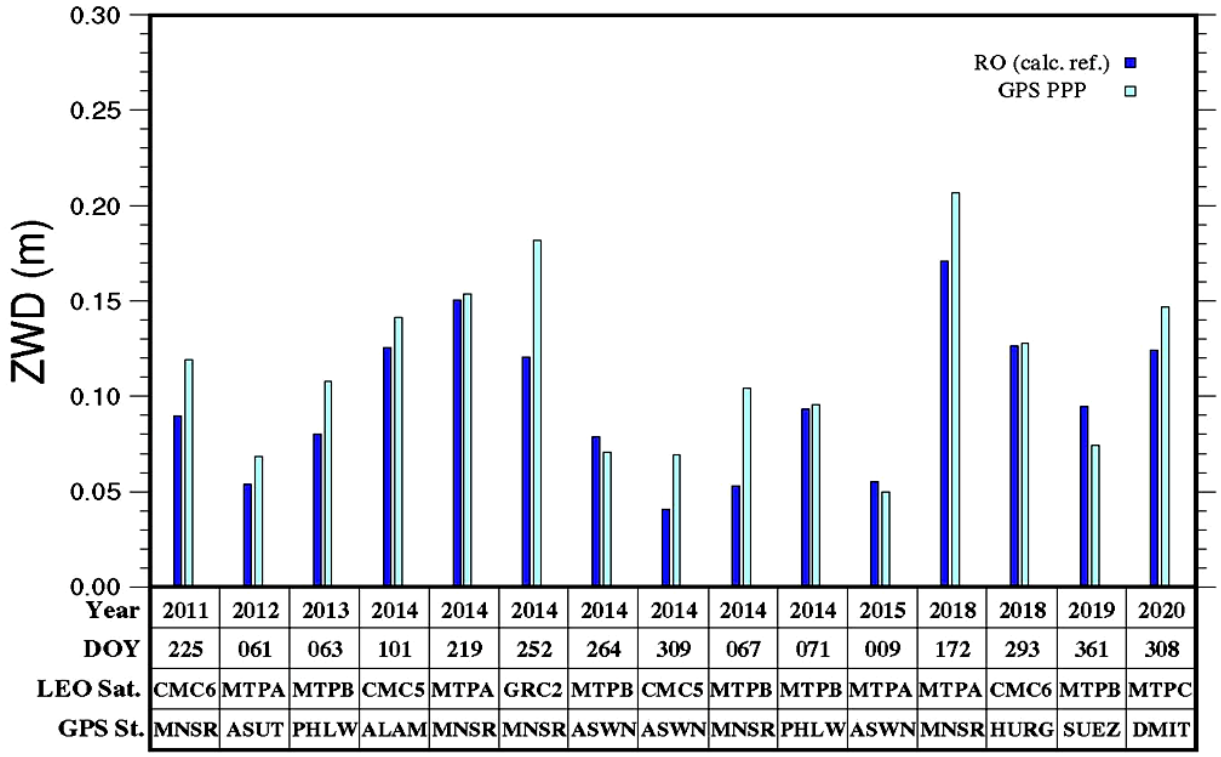

Year	2011	2012	2013	2014	2014	2014	2014	2014	2014	2014	2015	2018	2018	2019	2020
DOY	225	061	063	101	219	252	264	309	067	071	009	172	293	361	308
LEO Sat.	CMC6	MTPA	MTPB	CMC5	MTPA	GRC2	MTPB	CMC5	MTPB	MTPB	MTPA	MTPA	CMC6	MTPB	MTPC
GPS St.	MNSR	ASUT	PHLW	ALAM	MNSR	MNSR	ASWN	ASWN	MNSR	PHLW	ASWN	MNSR	HURG	SUEZ	DMIT

Fig. (4.9): ZWD for RO and PPP.

Table (4.6) indicates the differences between ZPD values for RO and PPP analysis. The table shows the results of a T-test which made to find the degree of correspondence between RO and PPP ZPD values. Calculated RO ZHD deviates from the PPP analysis result by 1.9 cm. The

analyzed and the observed ones deviate by 2.5 cm from the PPP analysis result. Here also, the calculated RO results give small difference values from the RS and PPP analysis results in both of ZHD and ZWD and this supports its stand against the other two RO refractivity methods.

Table (4.6): ZPD differences (m) and T-test results for PPP, and RO data.

Variable 1	Variable 2	Difference		t value	p value	T critical
		Mean	St. Dev.			
PPP-ZHD	**RO(calc.)-ZHD**	0.019	0.007	1.008	0.322	2.048
PPP-ZHD	**RO(analyzed)-ZHD**	0.025	0.008	1.643	0.112	2.048
PPP-ZHD	**RO(obs.)-ZHD**	0.025	0.008	1.64	0.112	2.048
RO(calc.)-ZHD	**RO(analyzed)-ZHD**	0.009	0.002	0.567	0.575	2.048
RO(calc.)-ZHD	**RO(obs.)-ZHD**	0.008	0.003	0.565	0.577	2.048
PPP-ZWD	**RO-ZWD**	0.022	0.005	1.149	0.26	2.048

4.7 Relation Between ZPD and Meteorological Parameters

To study the relation between the ZPD and pressure, temperature and WVP, regression analysis is the convenient statistical process. ZPD is acting as the response variable and the other meteorological parameters as the predictors. More than 14600 RO observations for 11 years of data are used to find the relations between each meteorological parameter and ZPD values. About 11600 observations (80% of data from 2010 to 2017) are used in linear regression to find the relation equation between ZPD and the meteorological parameters. The remaining observations (2018-2020) are used for the verification of the resulting linear regression equation. The significance F value will identify the validity for model construction. The T-test will verify the model parameters using the remaining 20% of data that don't participate in model construction.

Fig. (4.10) shows the relation between the atmosphere surface pressure as an independent variable with ZHD as a dependant variable. It is clearly seen from the figure that increasing the air pressure cause ZHD accretion however, the correlation between the pressure and the ZHD is considered strong by a correlation factor of 0.87. Using ANOVA test, the significance F is 0.00 which is less than 0.05. This indicates that the pressure has a statistically significant association with ZHD using the constructed model. Equation (4.1) shows the intercept and the pressure factor for the model of ZHD and air pressure observations. By applying T-test on the remain 20% of data to verify the model, the T-value is 1.64 and less than the T-critical which is 1.96 which insure the model success.

$$ZHD = 0.224 + 0.002 * P \tag{4.1}$$

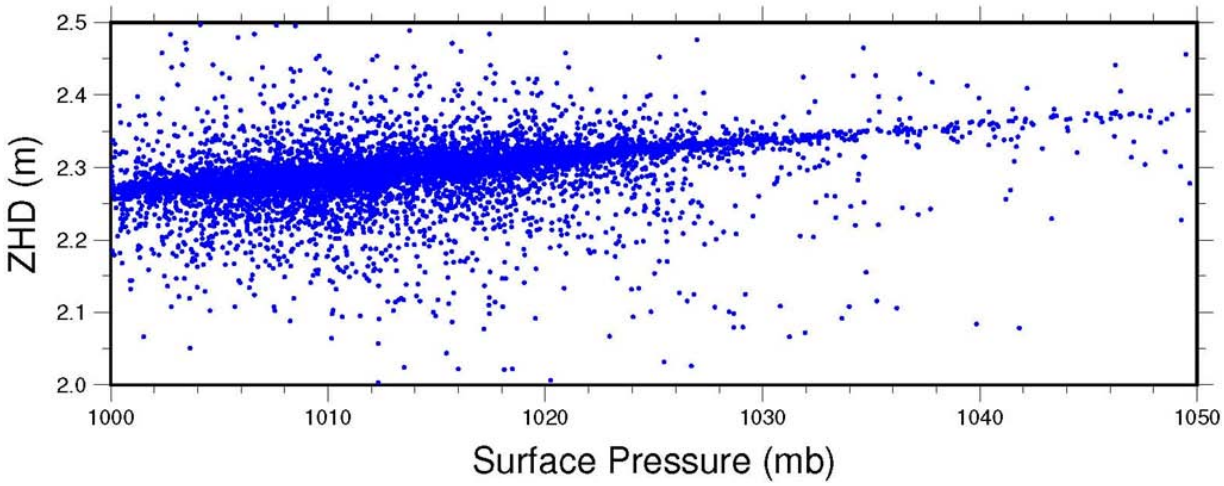

Fig. (4.10): Surface Pressure with ZHD.

Fig. (4.11) shows the relation between the atmosphere surface pressure as an independent variable with ZWD as a dependant variable. The figure shows that the general trend for the ZWD is decreasing by increasing the pressure; however, the correlation between the pressure and the ZWD is weak by a correlation factor of 0.263. Using ANOVA test, the significance F is 0.00 which is less than 0.05 and this indicates that the

pressure has a statistically significant association with ZWD using the constructed model. Equation (4.2) indicates the intercept and the pressure factor for the model of ZWD and air pressure observations. By applying T-test on the remain 20% of data to verify the model, the T-value is equal 1.22 which less than the T-critical which equal 1.96 and that ensure the model success.

$$ZWD = 4.71 - 0.0045 * P \tag{4.2}$$

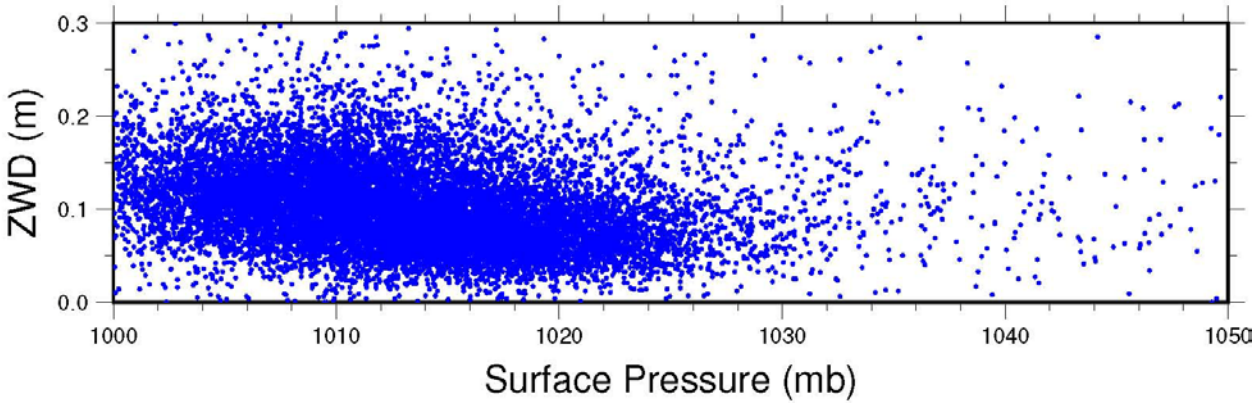

Fig. (4.11): Surface Pressure with ZWD.

Fig. (4.12) shows the relation between the atmosphere surface temperature as an independent variable with ZHD as a dependant variable. It is easily seen from this figure that the general trend for the ZHD is decreasing by increasing the temperature; however, the correlation between the temperature and the ZHD is moderate by a correlation factor of 0.55. Using ANOVA test, the significance F is 0.00 which is less than 0.05 and this indicates that the temperature has a statistically significant association with ZHD using the constructed model. Equation (4.3) shows the intercept and the temperature factor for the model of ZHD and air temperature observations. By applying T-test on the remain 20% of data to verify the model, the T-value is equal 0.596 which less than the T-critical which equal 1.96 and that ensure the model success.

$$ZHD = 2.35 - 0.002 * T \quad (4.3)$$

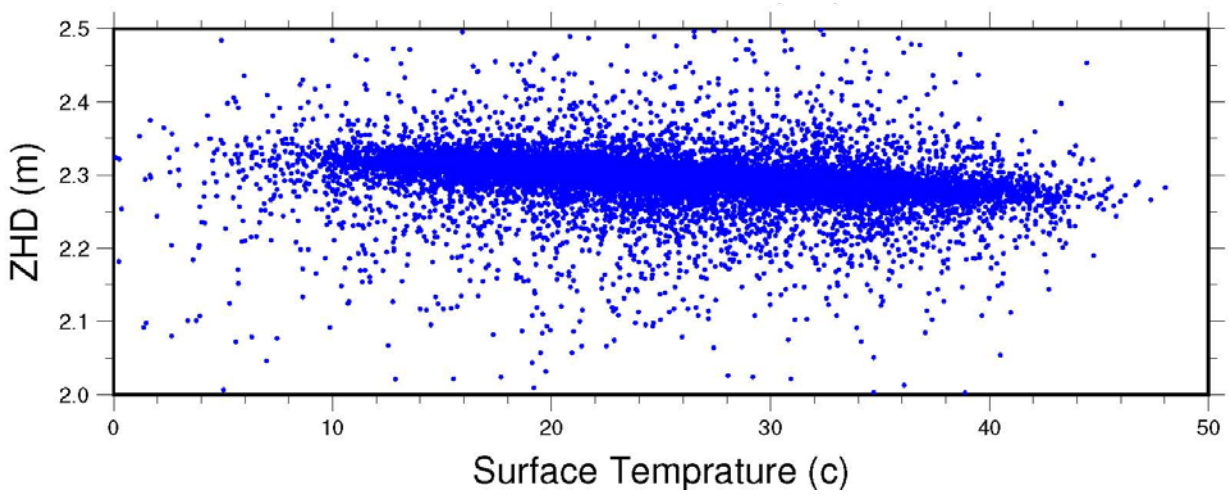

Fig. (4.12): Surface temperature with ZHD.

Fig. (4.13) demonstrates the relation between the atmosphere surface temperature as an independent variable with ZWD as a dependant variable. The figure shows that the general trend for the ZWD is increasing by increasing the temperature however, the correlation between the temperature and the ZWD is very weak by a correlation factor of 0.02 in other words, there is no correlation also between the ZWD and temperature. Using ANOVA test, the significance F is 0.02 which is less than 0.05 and this indicates that the temperature has a statistically significant association with ZWD using the constructed model. Equation (4.4) shows the intercept and the temperature factor for the model of ZWD and air temperature observations. By applying T-test on the remained 20% of data to verify the model, the T-value is equal 1.238 which less than the T-critical which equal 1.96 and that ensure the model success.

$$ZWD = 0.072 + 0.0014 * T \quad (4.4)$$

Fig. (4.14) illustrates the relation between the atmosphere surface WVP as an independent variable with ZHD as a dependent variable. The figure shows that the general trend for the ZHD is decreasing by

increasing the WVP however, the correlation between the WVP and the ZHD is considered weak by a correlation factor of 0.25. Using ANOVA test, the significance F is 0.92 which is more than 0.05 and this indicates that the WVP not has a statistically significant association with ZHD using the constructed model. So, it is not statistically valid to construct a model for ZHD based on WVP.

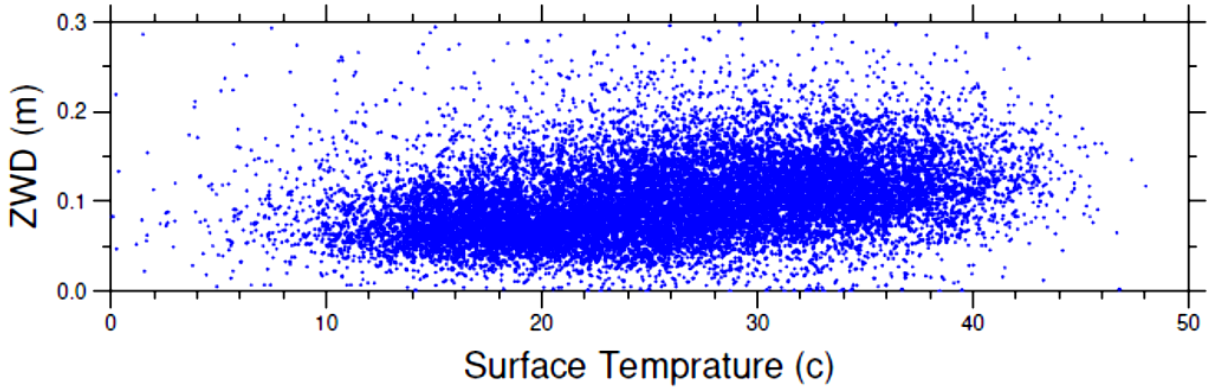

Fig. (4.13): Surface temperature with ZWD.

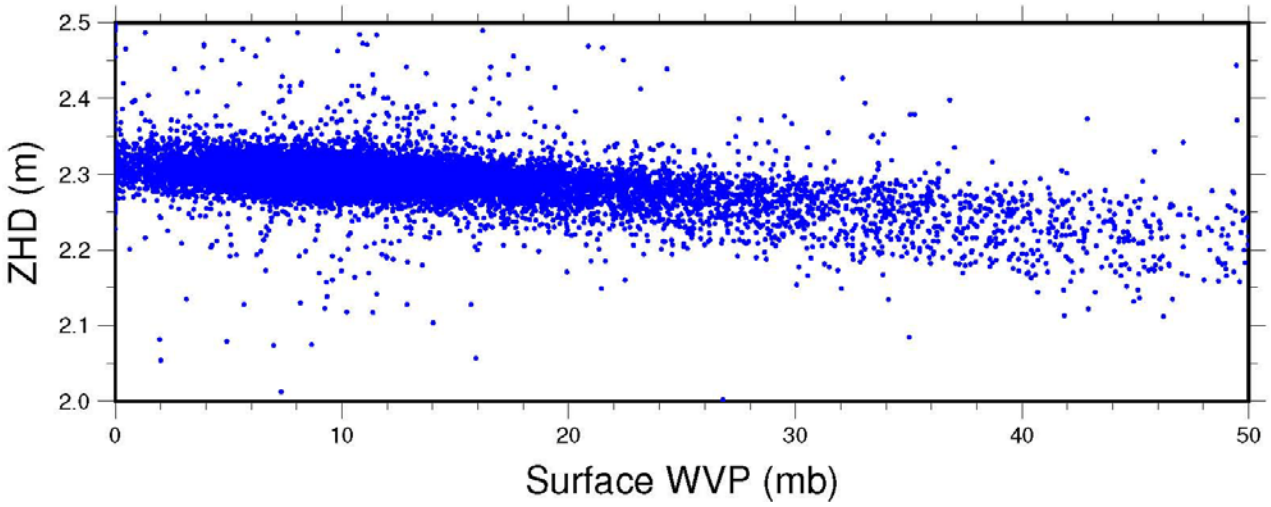

Fig. (4.14): Surface WVP with ZHD.

Fig. (4.15) demonstrates the relation between the atmosphere surface WVP as an independent variable with ZWD as a dependent variable. The figure shows that the general trend for the ZWD is increasing by WVP increase. However, the correlation between the WVP and the

ZWD is very weak by a correlation factor of 0.123. Using ANOVA test, the significance F is 0.00 which is less than 0.05 and this indicates that the WVP has a statistically significant association with ZWD using the constructed model. Equation (4.5) shows the intercept and the WVP factor for the model of ZWD and air WVP observations. Using T-test for the remained 20% of data to verify the model, the T-value is equal 1.26 which less than the T-critical that equal 1.96.

$$ZWD = 0.0197 + 0.0051 * e \tag{4.5}$$

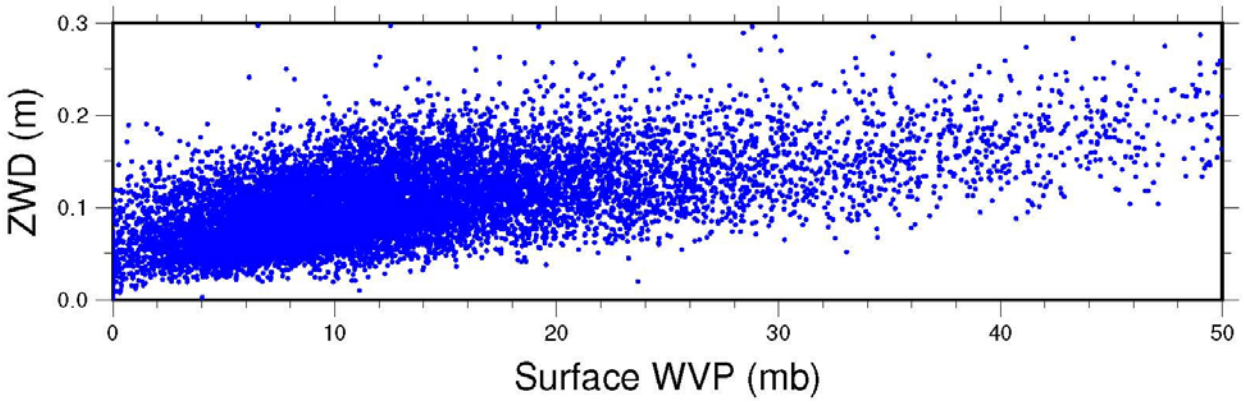

Fig. (4.15): Surface WVP with ZWD.

4.8 Relation between ZPD and Latitude and Longitude

To examine if the latitude and longitude change affects the ZHD or ZWD, linear regression process is made. The same procedures in the previous section are executed to identify the relation between latitude and longitude and delay values. About 80% of data are used in model construction and the remained for the judgment. Significance F value is used in model validation and T-test for model verification.

Fig. (4.16) illustrates the relation between the ZHD and the latitude in Egypt. Red, blue, orange, green and grey color points refer to observations located in longitude ranges from 25-28, 28-30, 30-32, 32-34, and 34-37, respectively. It seems from this figure that the general trend is

not in a definite direction. The trend line seems to be horizontal. The correlation coefficient is equal to 0.007 and this pointing to a very weak correlation between the latitude and the ZHD. The significance F value is equal to 0.429 and this insures the incapability of model construction combine the ZHD and the latitude.

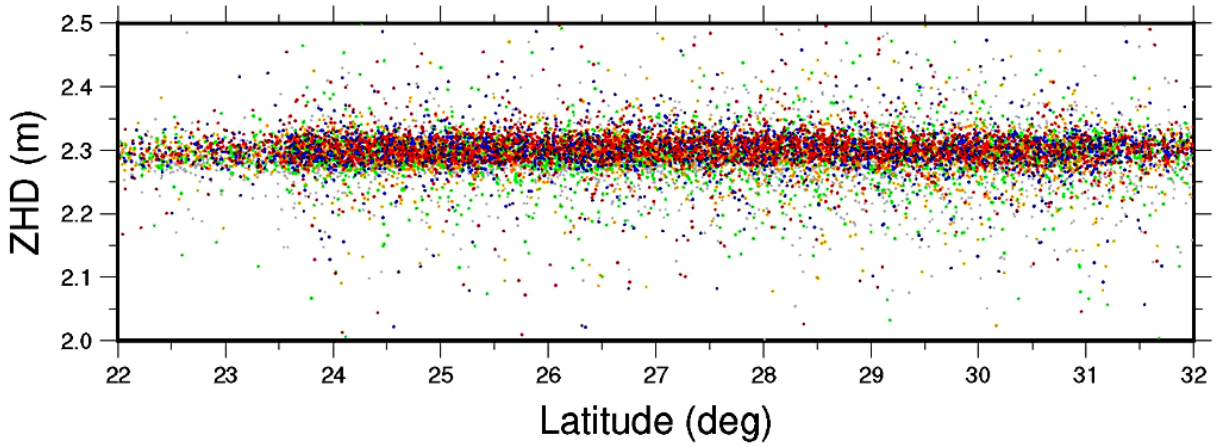

Fig. (4.16): ZHD change with latitude.

Fig. (4.17) shows the relation between the ZWD and the latitude in Egypt. Red, blue, orange, green and grey color points refer to observations located in longitude ranges from 25-28, 28-30, 30-32, 32-34, and 34-37, respectively. It seems from the figure that the general trend for the ZWD values is slightly increasing with latitude increasing. The correlation coefficient is equal to 0.000 and this indicating to correlation privation between the latitude and the ZWD. The significance F value is equal to 0.946 and this also, ensures the incapability of constructing a model combines the ZWD and the latitude.

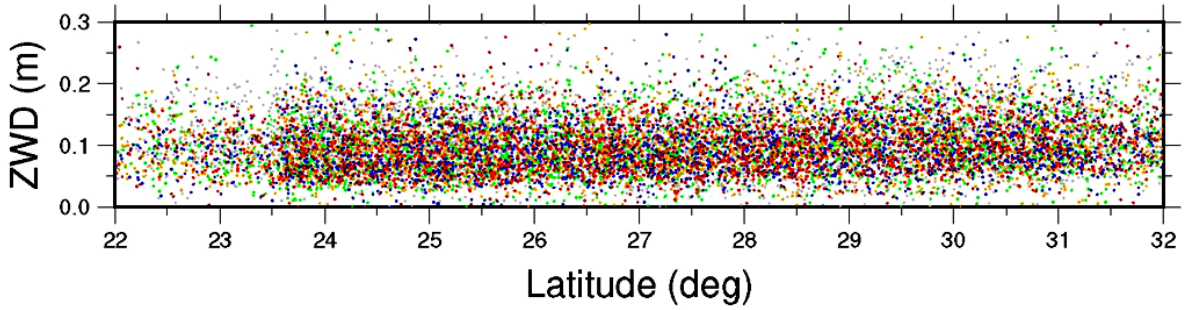

Fig. (4.17): ZWD change with latitude.

Fig. (4.18) demonstrates the relation between the ZHD and the

longitude in Egypt. Red, blue, orange, green and grey color points refer to observations located in latitude ranges from 22-24, 24-26, 26-28, 28-30, and 30-32, respectively. It seems from the figure that the general trend for the ZHD values is slightly decreasing with longitude increasing. The correlation coefficient is equal to 0.16 and this pointing to a weak correlation between the longitude and the ZHD. The significance F value is equal to 0.012 and this confirms the validity of the constructed model to represent the relation for the ZHD with the longitude.

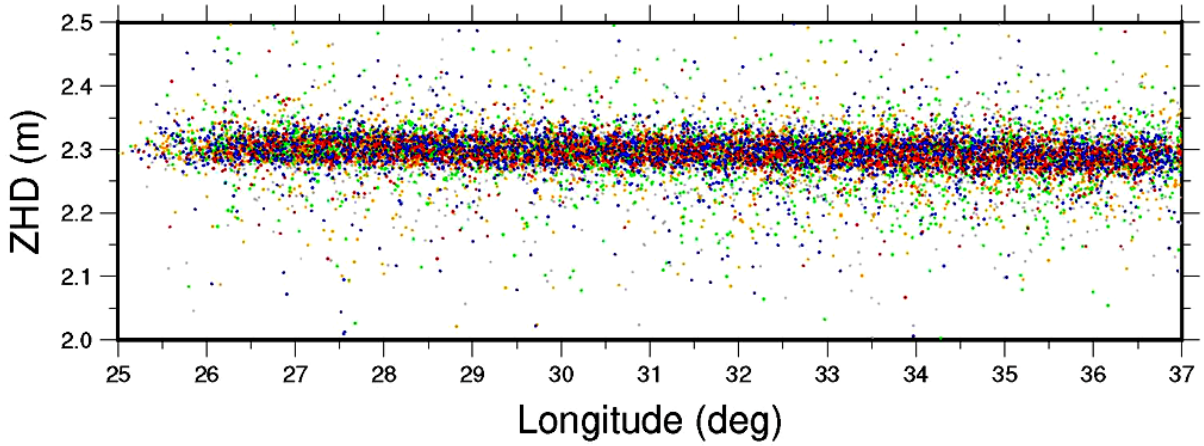

Fig. (4.18): ZHD change with longitude.

Equation (4.6) demonstrates the intercept and the longitude factor for the model of ZHD and longitude value in Egypt. By applying T-test on the remained 20% of data to verify the model, the T-value is equal 0.043 which less than the T-critical that equal 1.96.

$$ZHD = 2.4 - 0.0033 * \lambda \qquad (4.6)$$

where λ is the longitude value.

Fig. (4.19) illustrates the relation between the ZWD and the longitude in Egypt. Red, blue, orange, green and grey color points refer to observations located in latitude ranges from 22-24, 24-26, 26-28, 28-30, and 30-32, respectively. It is clearly seen from the figure that the general

trend for the ZWD values is slightly increasing with longitude increasing. The correlation coefficient is equal to 0.013 and this indicating to a very weak correlation between the latitude and the ZWD. The significance F value is equal to 0.172 and this also, insures the incapability of constructing a model combines the ZWD and the latitude.

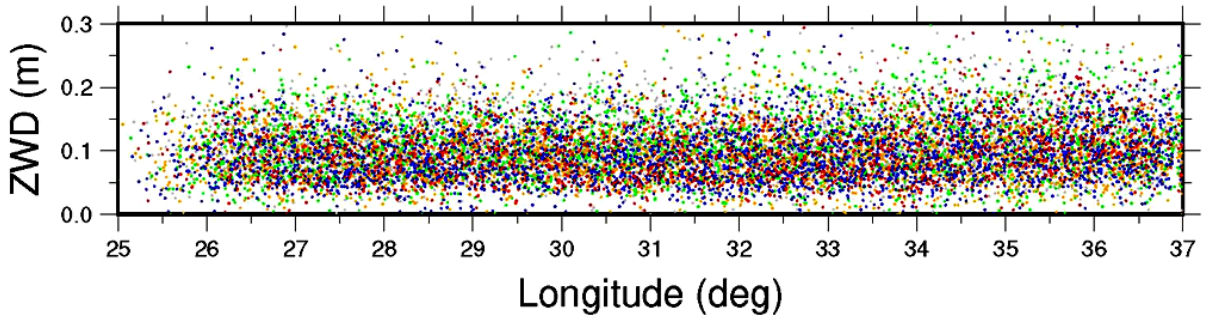

Fig. (4.19): ZWD change with longitude.

4.9 Delay Time Series

One of the present research objectives is to draw the time series for ZHD and ZWD. As mentioned above, ZHD is related to pressure and temperature and ZWD is related to pressure, temperature and WVP. The changes in the meteorological parameters through the year days affect the delay values so there is a relation between the delay values and the DOY.

Fig. (4.20) illustrates the time series of the ZHD through the study period. Red, blue, orange, green and grey color points refer to observations located in longitude ranges from 25-28, 28-30, 30-32, 32-34, and 34-37, respectively. It is clear that ZHD starts the year by a value reaches to 2.34 m. By the year days, ZHD reaches its minimum values in August to be about 2.25 m. Fig. (4.21) shows the delay values through the year months for all study period years. It is obviously that, changes in ZHD values along the year don't seem to be big. To find the relation between the ZHD and the DOY, a linear regression is made to get the statistical judgment.

The correlation coefficient is 0.11 between the ZHD and the DOY number so the correlation is considered weak between the ZHD and year days represented in DOY. By doing the regression, the significance F value is found to be equal 0.75 which insure incapability of constructing a model gather the ZHD with the DOY. So, there is no relation between the ZHD and the DOY. It is obvious for the two figures that red points are located bit higher than the other colors. Also, grey points are located bit.

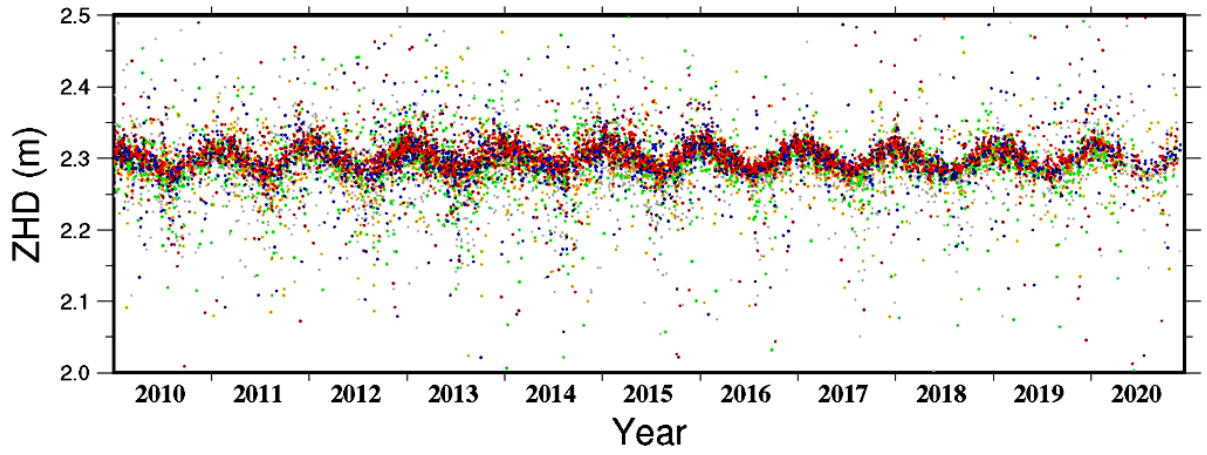

Fig. (4.20): ZHD time series through the study period.

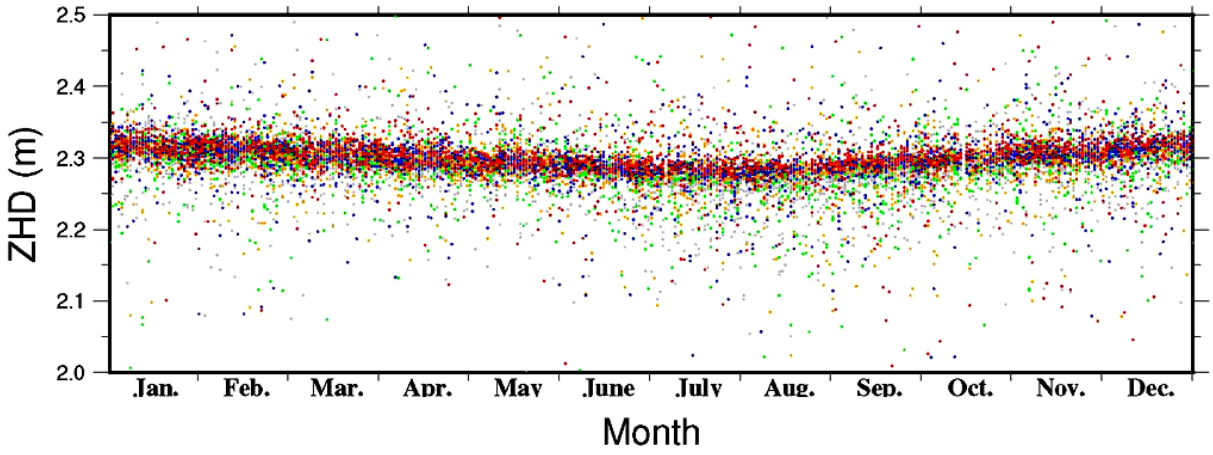

Fig. (4.21): ZHD time series through the years.

Figs. (4.22 and 4.23) show the time series of the ZHD through the study period and the study years, respectively. According to the first figure, it is clear that the ZWD starts the year by a value equal about 0.075 m. By the year days, the ZWD reaches its minimum values in February to be about 0.04 m. Then, the ZWD

reaches its maximum values in August to be about 0.20 m. To find the relation between the ZWD and the DOY, a linear regression is made to get the statistical posture. The correlation coefficient is 0.05 between the ZWD and the DOY number. So, there is a very weak correlation between the ZHD and the DOY numbers. By doing the regression, the significance F value is found to be equal 0.000 which insure the capability of constructing a model gather the ZWD with the DOY and insure also that there is a relation between the ZWD and the DOY.

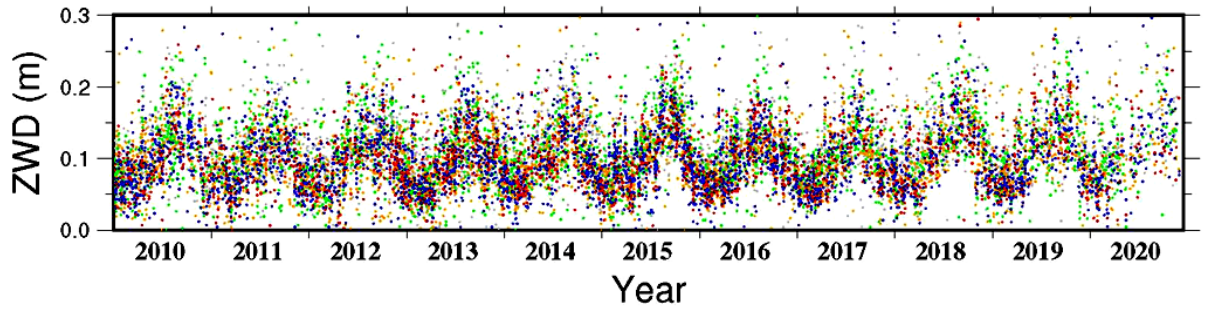

Fig. (4.22): ZWD time series through the study period.

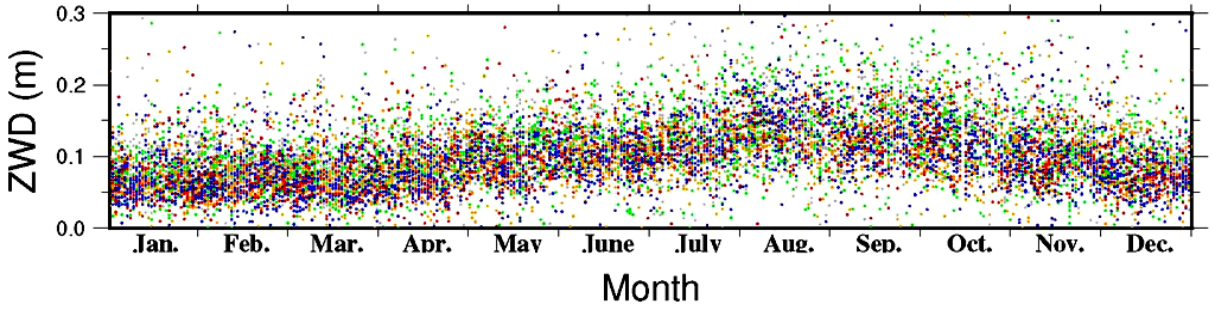

Fig. (4.23): ZWD time series through the years.

Equation (4.7) indicates the intercept and the DOY factor for the model of ZWD and DOY number. By applying T-test on the remained 20% of data to verify the model, the T-value is equal 1.24 which less than the T-critical that equal 1.96.

$$ZWD = 0.07 + 0.0002 * DOY \tag{4.7}$$

4.10 ZHD and ZWD Models

As mentioned before, the ZHD depends on pressure, temperature and longitude and ZWD depends on pressure, temperature, WVP and DOY. By applying a multi-linear regression in ZHD and ZWD as dependent variables and their predictors, multi-variable models are constructed for ZHD and ZWD prediction. As stated above, statistically, there is no way to construct a model combines ZHD with WVP, DOY or latitude and also for the ZWD with latitude or longitude as the significance F for the statistical regression process for each of them is more than 0.05.

By doing a multiple regression analysis for the ZHD with the pressure, temperature and longitude in Egypt, the multiple correlation coefficient is found to be 0.126. Although the correlation coefficient represents a weak correlation, the significance F for the regression is found to be 0.000 that ensure the validity of constructing a model between the variables. Equation (4.8) illustrates the terms of the ZHD model. About 11600 observations are used in ZHD model construction. To verify the model, other 3000 (the remained 20% of data) observations are used in model verification using T-test. The resulted T-value and T-critical are found to be 1.945 and 1.96, respectively. As a result, the model is valid and verified to predict the ZHD. The model average error based on the out-layer observations, not involved in model construction, is 1.0 cm and this is a good indicator. The coefficient of determination (R^2) for the ZHD is 0.85, 0.25 and 0.08 for each of pressure, temperature and longitude.

$$ZHD = 0.3615 + 0.002P - 0.0014T - 0.0024\lambda \tag{4.8}$$

Additionally, by doing a multiple regression analysis for the ZWD with the pressure, temperature, WVP and DOY, the multiple correlation coefficient is found to be 0.289. Furthermore, the correlation coefficient

represents a weak correlation however, the significance F for the regression is found to be 0.000 that ensure the validity of constructing a model between the variables. Equation (4.9) demonstrates the terms of the ZWD model. The same percentage of data is used in model verification using T-test. The resulted T-value and T-critical are 1.25 1.96, respectively. Consequence, the model is valid and verified to predict the ZWD. The ZWD model average error based on the out-layer observations, not involved in model construction, is 3.7 cm and this is a not very good indicator because this error is considered high comparing to the ZWD small values. The coefficient of determination (R^2) for the ZWD is 0.66, 0.03, 0.30 and 0.08 for each of pressure, temperature, WVP and DOY.

$$ZWD = 4.613 - 0.004P - 0.0015T + 0.005e + 0.0001DOY \quad (4.9)$$

Summing up, ZPD models based on RO data is featured by high accuracy and adequate number of observations that add the realism and credibility to the constructed models. Statistical testing for model validation and verification insures the model feasibility as well. Actually, the linear regression could produce a good outcome. But, studying higher and various types of mathematical functions, surly, will participate in more model realism.

4.11 ZPD and Meteorological Parameters Spatial Distribution Maps

Here, the spatial distribution of ZHD and ZWD are drawn to get a more details about their distribution on the Egypt map. The following figures show the spatial distribution of each parameter in 2010 and 2019. The distribution of each year uses all data located in Egypt through the whole year days. Additionally, images for two years represent the start, and the end of the study period were shown in the following figures. Year

2020 data was not used because cosmic data for it was not released in CDAAC web site till soon date.

Fig. (4.24) shows the ZHD spatial distribution over Egypt for years 2010 and 2019. Most of Egypt area gets green color which represents the ZHD range from 2.28 to 2.31 m. Note that, the year 2010 have 1356 RO observations. The average ZHD through 2010 is 2.2946 m with standard deviation of 0.0008 m. On the other side, there 1050 observations were located in Egypt through 2019. The average ZHD through 2019 is found to be 2.2944 m with standard deviation of 0.0033 m. Blue color is not big in both of maps but red colors cover bigger area. The figure also shows that, 2019 map has disturbances in ZHD more than that of 2010 map. This might be due to the rapid changes in pressure and temperature values as the standard deviation for both of them are increased in this period. In addition, satellite types represent a number in this equation as COSMIC and MetOp data has a number of out-of-range data less than it for the other types of satellites and data recently depended on various types of satellites.

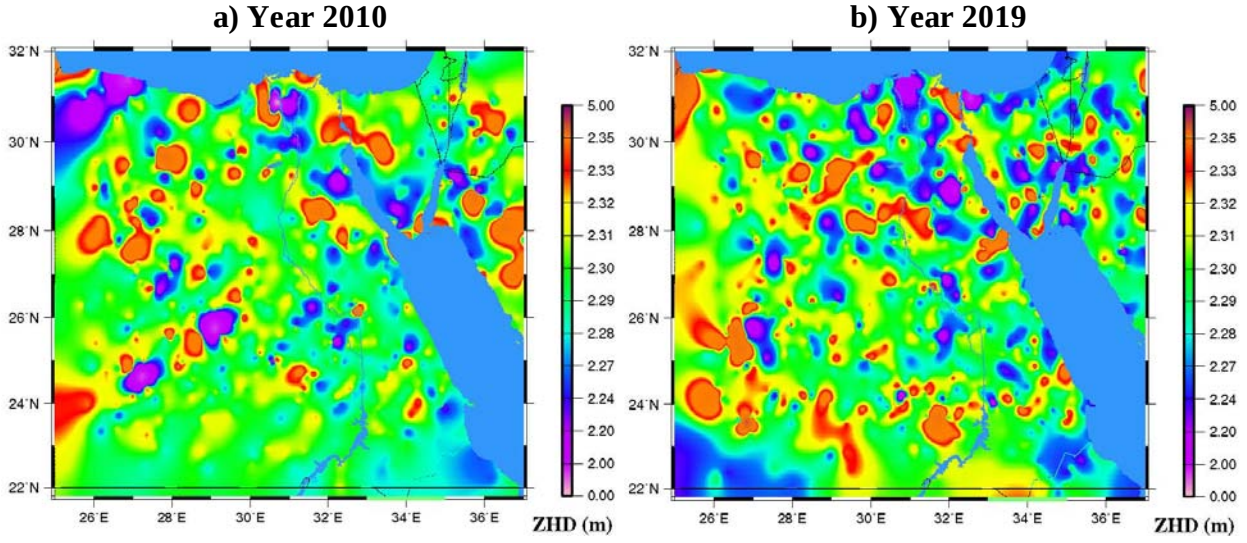

Fig. (4.24): ZHD distribution on Egypt map.

Fig. (4.25) shows the spatial distribution of ZWD for Egypt over

years 2010 and 2019. Green color represents the prevalent color despite the blue upsets. The prevalent range for the ZWD over both of years is from 10.0 cm to 16.0 cm however, there are big ups and downs. For the same number of observations for both years, the average ZWD through 2010 is 11.7 cm with standard deviation of 1.5 mm. The average ZWD through 2019 is found to be 14.85 cm with standard deviation of 3.6 cm. ZWD value and its standard deviation are manifestly got big growth from 2010 to 2019. Surly, the pressure growth must accompany delay growth by its two components. Disturbances appeared in both of years map but only in the SD of year 2019. It is clear that, blue areas are diffused all over both of maps, but the red areas are in the southern region in 2010 map and in northern, western, and southern regions in 2019 map. The up and down disturbances represent almost the same percentage in both of maps.

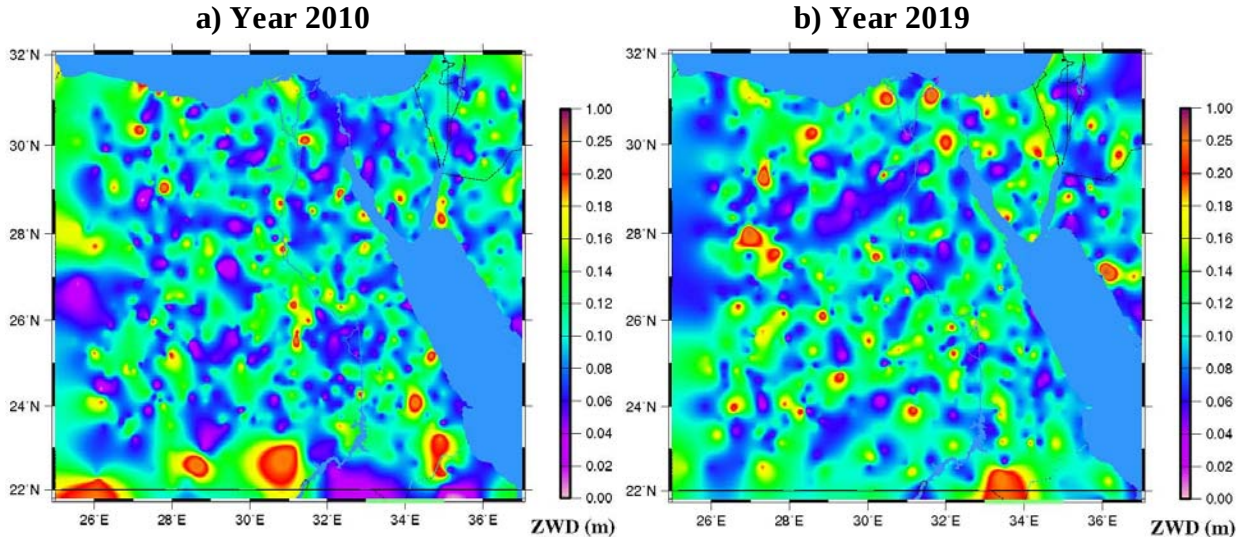

Fig. (4.25): ZWD distribution on Egypt map.

Fig. (4.26) shows the pressure distribution for Egypt over years 2010 and 2019. It is clear that, zonal differences in pressure bigger in 2019 than 2010. Most of zones in 2010 pressure map are under 1025 mb. The mean of pressure observations through 2010 is 1016.25 mb with SD of 0.19 mb. The mean of pressure observations through 2019 is 1013.46 mb

with SD of 1.21 mb. Despite the mean pressure for 2019 is smaller than it for 2010, the SD is bigger, and this represents the disturbances appears on map. Pressure disturbances in 2019-year map have its impact obviously on ZHD map disturbances in 2019.

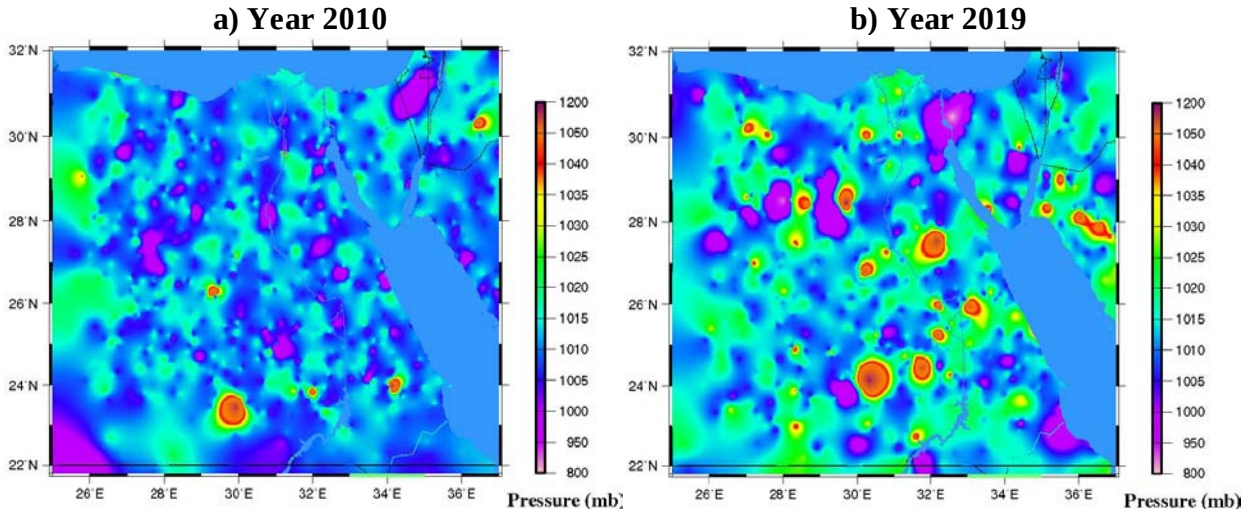

Fig. (4.26): Pressure distribution on Egypt map.

Fig. (4.27) shows the WVP distribution for Egypt over years 2010 and 2019. It is easily seen that, zonal differences in WVP bigger in 2010 than 2019. The mean of WVP observations through 2010 is 18.79 mb with SD of 0.33 mb. The mean of WVP observations through 2019 is 14.82 mb with SD of 0.28 mb.

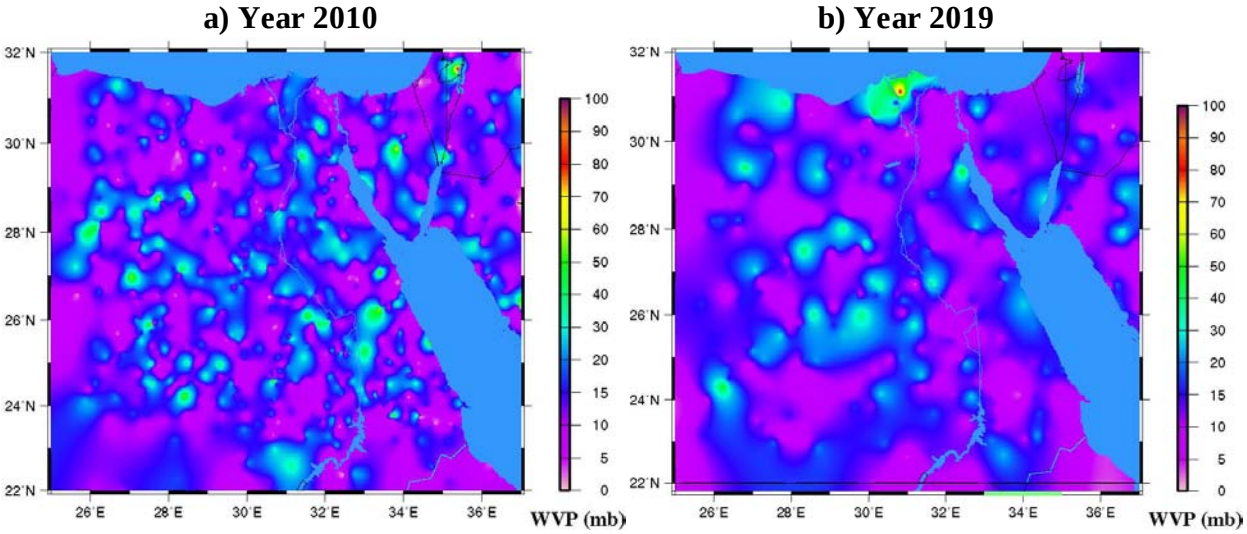

Fig. (4.27): WVP distribution on Egypt map.

The mean WVP for 2019 is smaller than it for 2010 and the SD also is smaller. Although, the WVP and its SD in 2010 is more than that of 2019, the ZWD and its SD in 2019 is more than it for 2010. Finally, Fig. (4.28) shows the spatial distribution of temperature for Egypt in 2010 and 2019 years. Although, the disturbances in 2010 appear to be more than that of 2019, the other years maps (2011-2018) are slightly different from 2019. The mean temperature in 2010 is 27.53°c with SD of 0.19°c. The mean temperature in 2019 is 25.92°c with SD of 0.24°c. By drawing the temperature spatial distribution of other years, 2010 has big disturbances than the other recent years. In 2010 and 2019, the southern Egypt has big temperature values than the northern region. This might be due to getting closer to the Equator area.

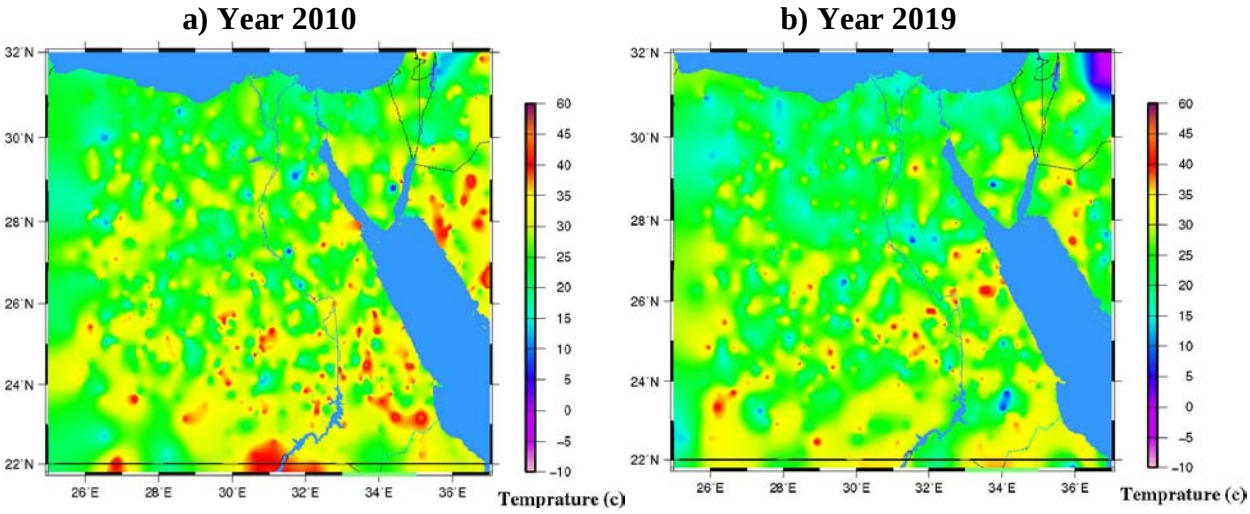

Fig. (4.28): Temperature distribution on Egypt map.

CHAPTER 5

COCLUSIONS AND RECOMMENDATIONS

Chapter 5 : Conclusions and Recommendations

In the present chapter, a brief summary of the research and the most important conclusions drawn from the study, which could be obtained as a result of analyzing and discussing the results of the present research and some recommendations are represented.

5.1 Summary

Troposphere delay in Egypt is studied using the RO method. RO data is downloaded for the study period (year 2010 to 2020) from CDAAC web site. Only the profiles located in Egypt are included for all LEO satellites. Shortage in data was interpolated using LAGRANGE method to find the missed observations in each profile. CDAAC provides various netcdf files types containing different types of data. The file used in the present research is "wetprf" file which provides atmosphere total profile containing observation height, pressure, temperature, WVP, analyzed and observed refractivity besides other parameters which not used in our research.

RS data is downloaded for the years 2010 to 2019 in netcdf files also to study the differences between the RO and RS profiles. Processing is executed using bash scripts and FORTRAN subroutines. RO and RS netcdf files are read using a FORTRAN program constructed mainly for data reading and preprocessing preparation. RO-RS single profile comparison is done to check the rapprochement between the two profiles. A T-test is made and provided results favored the profiles similarity. Multi-profiles statistical differences are studied to compare the RO profiles and to check the integration of the two techniques observations. The height from 3 to 40 km is used in RO and RS data comparison as under the 3 km

altitude there are many data shortages in RO and RS profiles.

Results of multi-profiles comparison between RO and RS profiles showed that pressure, temperature, WVP and refractivity mean difference values are 0.6 mb, 0.79 deg, 0.1 mb, 0.48, respectively. However, refractivity values are significantly affected by small difference in the other parameters. Rendering to LEO satellites difference analysis, GRACE2 gave maximum difference values of 4.3±0.15 mb in pressure and 7.8±0.35 deg in temperature. COSMIC 3 & 6 and GRACE1 gave minimum difference values, and the other missions gave small difference values but all of these differences are considered statistically significant. As for upper air stations difference analysis, station Benina gave big difference values of 5.1±0.23 mb in pressure and 6±0.3 deg in temperature. Stations Mersa Matruh, Athalasa, South of Valley, and the other stations gave small difference values. However, all of stations differences are found to be statistically significant.

Delay components for RO, RS, and PPP processing are compared to check statistically the degree of likeness in delay results. A T-test has been executed for the ZHD and ZWD for the delay values resulted from the three techniques. The T-test averred that there is no significant difference in delay components between each of the three methods except for the RS with the PPP.

ZHD and ZWD relations with meteorological parameters, spatial vectors and time variations are studied to understand their influence on both of delay components. Results affirmed that pressure, temperature, and longitude impact on ZHD. However, pressure, temperature, WVP and DOY impact on ZWD. Additionally, ZHD and ZWD models based on linear regression are developed to predict accurately both of them.

Finally, the spatial distribution of ZHD, ZWD, pressure, WVP and temperature observations has been dedicated for Egypt through each year of study

period. Variables distribution on maps provides the degree of spatial stability for each variable and the changes occurred in each variable distribution.

5.2 Conclusions

RS and RO meteorological profiles are compared and difference analysis has been done to insure the applicability of integration RO and RS data in Egypt. Single pressure, temperature and refractivity profiles are same in RO and RS for observations time and distance variation of 40 min and 20 km, respectively. The WVP profiles vary between the two methods according to the charts, the T-test, and the mean absolute difference values. However, the correlation factors were not less than 0.99 for the four variables. Variation reached 1.0 mb, mean absolute difference reached 0.14 mb in the first check point and the T-test indicated that there is a significant difference between WVP profiles in the other two check points. By checking the difference of WVP values with ECMWF model, these variations seem to be reasonable in case of varying the time and distance.

Pressure, temperature, WVP and refractivity mean difference values are 0.6 mb, 0.79 deg, 0.1 mb, 0.48, respectively. The difference percentage per observations values for the four parameters are 0.3%, 1.7%, 62% and 0.7%, respectively. Generally, those difference values and percentage for different meteorological variables are not significant except for the WVP profiles.

Difference analysis used in this study indicated that, the difference values increase mostly with time and distance difference. All difference values found to be statistically significant for all meteorological variables for refractivity. All absolute difference values for pressure, temperature

and refractivity don't exceed 2 and this is small difference however, it is statistically significant. All difference means and RMS difference and MSD values were small comparing to the big observation values except for WVP. Time and spatial difference affect significantly the WVP difference values, so it is reasonable to find big difference values in WVP profiles.

LEO mission's data located in Egypt have been assessed using difference analysis for pressure and temperature profiles. GRACE2 data gave big difference values and MSD with relative error of 1.96%, 16.26%, respectively. However, both of them are considered statistically significant to the refractivity. GRACE1, COSMIC 3 & 6 gave biggest difference values and MSD. COSMIC 1, 2, 4, 5 and C/NOFS gave small difference values and MSD but all of them were considered statistically significant to the refractivity. By analyzing the RS stations data separately, station Benina gave a big difference in values and MSD. Stations Mersa Matruh, Athalasa, South of Valley, and other stations indicated small difference values and MSD nonetheless, they are statically significant.

Because of the increasing precision requirements of GPS applications, it is important to establish a precise tropospheric correction model for GPS surveying. To check the integration of the RO method with the other methods, delay values by its two components are calculated using RO, RS and PPP processing. The average differences between the RO and RS in ZHD and ZWD are 2.7 cm and 2.8 cm, respectively. The average differences between the RO and PPP processing results in ZHD and ZWD are 2.4 cm and 2.1 cm, respectively. To check the correspondence between the results for the three methods, a T-test is used. The T-test shows that all delay values have not significant differences

except for the RS-ZHD with the PPP delay. The differences between the RO and PPP results were also studied for the same time and with spatial difference and was found not exceeding 10 km. The average differences between the RO and PPP processing results in ZHD and ZWD were 2.3 cm and 2.2 cm, respectively.

The single and multiple linear regression between the meteorological parameters, spatial parameters, and DOY with delay components were applied. It indicated that the ZHD depends on pressure, temperature, and longitude. Moreover, ZWD depends on pressure, temperature, WVP and DOY. In the ZHD model, besides the constant, longitude number has the biggest negative effect by a factor -0.0024 then the pressure but in positive by a factor of 0.002 and the temperature by a factor of -0.0014. WVP has the big share in ZWD model by a factor of 0.005, besides the constant, then the pressure and temperature by a factor of -0.004 and -0.0015, respectively. In addition, the DOY contributed to ZWD model by a small positive effect with a factor reached 0.0001. The models average errors in ZHD and ZWD estimated based on the data not used in model creation were 1.0 cm and 3.7 cm, respectively.

In the end, spatial distribution of delay components and the other meteorological parameters were studied for more details about their distribution on Egypt. The results of spatial distribution indicated that: (1) The averages of ZHD through 2010 and 2019 for Egypt are 2.2946 and 2.2944 m with standard deviation of 0.0008 and 0.0033 m, respectively. (2) The averages of ZWD through 2010 and 2019 are found to be 11.7 and 14.85 cm with standard deviation of 0.15 and 3.6 cm, respectively. (3) The means of pressure observations through 2010 and 2019 are 1016.25 and 1013.46 mb with SD of 0.19 and 1.21 mb, respectively. (4) The means of

WVP observations through 2010 and 2019 are 18.79 and 14.82 mb with SD of 0.33 and 0.28 mb, respectively. (5) The means of temperature observations in 2010 and 2019 are 27.53 and 25.92°c with SD of 0.19 and 0.24°c, respectively.

5.3 Recommendations

- RO technique could be used in Egypt atmosphere identification properly.
- RO profiles accuracy is sufficient to be integrated with the other atmosphere identification methods.
- In RO-RS profiles comparison, GRACE1, COSMIC 3 & 6 gave biggest difference values and MSD. COSMIC 1, 2, 4, 5 and C/NOFS gave small difference values and MSD. So, it is preferable to use the observations of LEO satellites that give lower differences from the other methods observations.
- By analyzing the RO-RS observations differences based on RS stations, stations Mersa Matruh, Athalasa, South of Valley and Benina give big relative errors comparing to the other RS stations in or around Egypt.
- It is recommended to use the estimated ZHD and ZWD models in this study for hydrostatic and wet delay calculation.

As a future work,

- All LEO satellites observations will be assessed based on RS stations data all over the world to rate LEO satellites and upper air stations data.
- LEO data files available on CDAAC such as total electronic content observations might be studied in Egypt to understand properly the

spatial distribution of atmosphere for Egypt.

- Higher polynomial degrees in delay models will be studied to predict more accurate delay components from the surface meteorological data.
- Study applying the constructed models in Egypt region troposphere delay estimation in PPP processing programs and universal websites.

REFERENCES

References

Abdelfatah, M., Mousa, A. and El-Fiky, G., (2015). Precise troposphere delay model for Egypt, as derived from radiosonde data. NRIAG Journal of Astronomy and Geophysics, 31, 10.1016.

Ahmed, F., Vaclavovic, P., Teferle, F. N., Dousa, J., Bingley, R. and Laurichesse, D., (2014). Comparative analysis of real-time precise point positioning zenith total delay estimates. GPS Solution, 20, 187–199.

Ahmed, I. F., Mohamed, A. A. E., Mousa, A. E. and El-Fiky, G., (2022). Analysis of the differences between GPS radio occultation and radiosonde atmosphere profiles in Egypt, The Egyptian Journal of Remote Sensing and Space Science, 25, 2, 2022, 491-500.

Anthes, R. A., (2011). Exploring Earth's atmosphere with radio occultation: Contributions to weather. climate and space weather, Atmos. Meas. Tech. Discuss., 4, 135–212, doi:10.5194/amtd-4-135-2011.

Bevis, M., Businger, S., Chiswell, S., Herring, T. A., Anthes, R. A., Rocken, C. and Ware, R. H., (1994). GPS Meteorology: Mapping Zenith Wet Delays onto Precipitable Water, Journal of Applied Meteorology and Climatology, 33(3), 379-386.

Black, H. D., (1978). An easily implemented algorithm for the tropospheric range correction. J. Geophys. Res.: Solid Earth (1978–2012) 83, 1825–1828.

Boehm, J., Kouba, J. and Schuh, H., (2009). Forecast Vienna Mapping Functions 1 for real-time analysis of space geodetic observations. J. Geod. 83 (5), 397–401.

Boehm, J., Niell, A. E., Tregoning, P. and Schuh, H., (2006). Global Mapping Function (GMF): A new empirical mapping function based on numerical weather model data. Schuh Geophys. Res. Lett., 33(7), https://doi.org/10.1029/ 2005GL025546

Bohm, J., Moller, G., Schindelegger, M., Pain, G. and Weber, R., (2015). Development of an improved empirical model for slant delays in the

troposphere (gpt2w). GPS Solut. 19(3), 433–441.

Born, M. and Wolf, E., (1986). Principles of Optics. Pergamon Press, 6th Edition, 121–124, 1986.

Chang, L., Guo, L., Feng, G., Wu, X., Gao, G., Zhang, Y. and Zhang, Y., (2018). Comparison of the Arctic upper-air temperatures from radiosonde and radio occultation observations. Acta Oceanol, Sin. 37, 30–39, https://doi.org/ 10.1007/s 13131-018-1156-x.

Collins J. P.; and Langley R. B. (1997): A Tropospheric Delay Model for the User of the Wide Area Augmentation System. Final contract report prepared for Nav Canada, Department of Geodesy and Geomatics Engineering Technical Report No.187, University of New Brunswick, Fredericton, N.B., Canada.

Connolly, M., Connolly, R., Soon, W., Velasco Herrera, V. M., Cionco, R. G. and Quaranta, N. E., (2021). Analyzing Atmospheric Circulation Patterns Using Mass Fluxes Calculated from Weather Balloon Measurements: North Atlantic Region as a Case Study. Atmosphere 2021, 12, 1439, https://doi.org/10.3390/ atmos12111439.

Dach R., Hugentobler, U., Fridez, P. and Meindl, M., (2007), User manual of the Bernese GPS Software Version 5.0. AIUB Astronomical Institute, University of Bern.

Dawidowicz, K. and Krzan, G., (2014). Coordinate estimation accuracy of static precise point positioning using on-line PPP service, a case study. Acta Geodaetica et Geophysica Hungarica, 4937–55.

Dong, Z. and Jin, S., (2018). 3-D water vapor tomography in Wuhan from GPS, BDS and GLONASS observations. Remote Sens., 2018, 10, 62.

Durre, I., Vose, R. S. and Wuertz, D. B., (2006). Overview of the Integrated Global Radiosonde Archive. Journal of Climate, 19(1), 53-68.

ECMWF, Climate Data Store (Dataset: ERA5 hourly data on pressure levels from 1959 to present), (2022). [Online]. Available: https://cds.climate.copernicus-.eu/cdsapp-#!/dataset/reanalysis-era5-pressure-levels?tab=form [Accessed 24-1-2022].

ECMWF, European Centre for Medium-Range Weather Forecasts, (2022). [Online]. Available: www.ecmwf.int/en/. [Accessed 25-4-2022].

EOPortal, European Space Agency, (2022). [Online]. Available: earth-.esa.int/web/eoportal/satellite-missions/ [Accessed 25-4-2022].

ESA, European Space Agency, (2022). Earth Online. (2022). Available: earth.esa.int-/eogateway/missions/paz [Accessed 25-4-2022].

Eyre, J. R., (1994). Assimilation of radio occultation measurements into a numerical weather prediction system, Tech. Memo 199, 22 pp., Eur. Cent. For Medium-Range Weather Forecasts, Reading, England.

Fernandes, M.J., Lazaro, C., Ablain, M. and Pires, N., (2015). Improved wet path delays for all ESA and reference altimetric missions. Remote Sens. Environ., 2015, 169, 50–74.

Fjeldbo, G., Kliore, J., and Eshleman, V., (1971). The neutral atmosphere of Venus as studied with the Mariner V radio occultation experiments, The Astronomical Journal, 76, 123-140.

Ghoniem, I. F., Mousa, A. E. and El-Fiky, G., (2020). GNSS-RO LEO satellite orbit optimization for Egypt and the Middle East region. Alexandria Engineering Journal, 59, 1, 389-397.

Ghoniem, I., Mousa, A. E. and El-Fiky, G., (2017). Distribution of the GNSS-LEO occultation events over Egypt. NRIAG Journal of Astronomy and Geophysics, 6, 97-103.

Guo, Q., (2015). Precision comparison and analysis of four online free PPP services in station positioning and tropospheric delay estimation. GPS Solut., 2015, 19, 537–544.

Healy, S. B., and Eyre, J. R., (2000). Retrieving temperature, water vapour and surface pressure information from refractive-index profiles derived by radio occultation: A simulation study, Q.J.R. Meteorol. Soc., 126: 1661-1683.

Healy, S. B., Haase, J. and Lesne, O., (2002). Letter to the EditorAbel transform inversion of radio occultation measurements made with a receiver inside the

Earth’s atmosphere. Annales Geophysicae, European Geosciences Union, 2002, 20 (8), pp.1253-1256. ffhal-00329269.

Heroux, P., Kouba, J., (2001). GPS precise point positioning using IGS orbit products. Phys. Chem. Earth 2001, 26, 573–578.

Hofmann-Wellenhof, B., LIchtenegger, H. and Wasle, E., (2008). GNSS-Global Navigation Satellite Systems GPS, Glonass, Galileo and More. Springer: Vienna, Austria, 2008.

Hopfield, H., (1963). The effect of tropospheric refraction on the Doppler shift of a satellite signal. J. Geophys. Res., 68, 5157–5168.

Hopfield, H., (1969). Two-quadratic tropospheric refractivity profile for correcting satellite data. J. Geophys. Res., 7, 4487–4499.

InterMet, International Met Systems, (2022), [online]. Available: www.intermet-systems.com/products/Introduction-to-Radiosondes-and-Atmospheric Soundings/ [Accessed 15-5-2022].

JetStream, The National Weather Service, (2022), [online]. Available: www.weather.gov/jetstream/radiosondes [Accessed 15-5-2022].

Kuo, Y.-H., Schreiner, W. S., Wang, J., Rossiter, D. L. and Zhang, Y., (2005). Comparison of GPS radio occultation soundings with radiosondes. Geophys. Res. Lett., 32, L05817, doi:10.1029/2004GL-0214-43.

Kursinski, E. R., Hajj, G. A., Hardy, K. R., Schofield, J. T. and Linfield, R., (1997). Observing Earth’s atmosphere with radio occultation measurement using the Global Positioning System. J. Geophys. Res., 102, 23429–23465.

Kursinski, E.R., Hajj, G.A., (2001). A comparison of water vapor derived from GPS occultations and global weather analyses, Journal of Geophysical Research 106 (D1), 1113–1138.

Leandro, R. F., Santos, M. C. and Langley, R. G., (2011). Analyzing GNSS data in precise point positioning software. GPS Solut., 2011, 15, 1–13.

Li, W., Yuan, Y., Ou, J., Li, H. and Li, Z., (2012). A new global zenith tropospheric delay model IGGtrop for GNSS applications. Chin. Sci. Bull.,

57, 2132–2139.

Melbourne, W. G., Davis, E. S., Duncan, C. B., Hajj, G. A., Hardy, K. R., Kursinski, T. K. Meehan, E. R., Young, L. E. and Yunck, T. P., (1994). The application of spaceborne GPS to atmospheric limb sounding and global change monitoring, JPL-Publication 94-18, Jet Propulsion Laboratory, California Institute of Technology, Pasadena, California.

Mendez Astudillo, J., Lau, L., Tang, Y.-T. and Moore, T., (2018). Analysing the Zenith Tropospheric Delay Estimates in On-line Precise Point Positioning (PPP) Services and PPP Software Packages. Sensors 2018, 18, 580.

Mendonca, M., White, R. M., Santos, M. C. and Langley, R.B., (2016). Assessing GPS + Galileo precise point positioning capability for integrated water vapor estimation. International Symposium on Earth and Environmental Sciences for Future Generations, International Association of Geodesy Symposia, 147.

Mousa, A., Aoyama, Y. and Tsuda, T., (2006). A simulation analysis to optimize orbits for a tropical GPS radio occultation mission. Earth Planets Space, 58, 919–925.

NASA, The National Aeronautics and Space Administration (Goddard Space Flight Center), (2022). [Online]. Available: www.nasa.gov/centers/goddard/ [Accessed 25-4-2022].

Niell, A.E., (1996). Global mapping functions for the atmosphere delay at radio wavelengths. J. Geophys. Res., Solid Earth, 101, (B2), 3227–3246.

NOAA, National Oceanic and Atmospheric Administration, (2022). [Online]. Available: www.ncdc.noaa.-gov [Accessed 1-5-2022].

NOAA, National Oceanic and Atmospheric Administration, and Global Systems Laboratory (GSL), (2022). [Online]. Available: www.ruc.noaa.-gov/raobs [Accessed 1-5-2022].

Norman, R., Le Marshall, J., Zhang, K, Wang, C. S., Carter, B. A., Rohm, W., Manning, T., Gordon, S. and Li, Y., (2014). Comparing GPS Radio Occultation Observations with Radiosonde Measurements in the Australian

Region. In Earth on the Edge: Science for a Sustainable Planet (pp. 51-57), Springer, Berlin, Heidelberg.

Padullés, R., Cardellach, E., Wang, K.-N., Ao, C. O., Turk, F. J. and de la Torre-Juárez, M., (2018). Assessment of global navigation satellite system (GNSS) radio occultation refractivity under heavy precipitation, Atmos. Chem. Phys., 18, 11697–11708.

Palmer, P. I., Barnett, J. J., Eyre, J. R. and Healy, S. B., (2000). A nonlinear optimal estimation method for radio occultation measurements of temperature. humidity and surface pressure, J. Geophys. Res., 105, D13, 17 513–17 526, 2000 .

Penna, N., Dodson, A. and Chen, W., (2001). Assessment of EGNOS tropospheric correction model. J. Navig., 54, 37–55.

Phinney, R. A. and Anderson, D. L., (1968) On the radio occultation method for studying planetary atmospheres. J. Geophys. Res., 73, 5, 1819–1827, 1968.

PODAAC, Jet Propulsion Laboratory (California Institute of Technology), (2022). [Online]. Available: podaac.jpl.nasa.gov/GRACE [Accessed 3-4-2022].

Rocken C., Anthes, R., Exner, M., Hunt, D., Sokilovskiy, S., Ware, R., Gorbunov, M., Schreiner, W., Feng, D., Herman, B., Kuo, Y. H., and Zou, X., (1997). Analysis and validation of GPS/MET data in the neutral atmosphere. J. Geophys. Res., 102, D25, 29 849– 29 866, 1997.

Rocken, C., Kuo, Y.-H., Schreiner, W., Hunt, D., Sokolovskiy, S. and McCormick, C., (2000). COSMIC system description. Terr Atmos Oceanic Sci., 11(1), 21–52.

Saastamoinen, J., (1972). Atmospheric correction for the troposphere and stratosphere in radio ranging satellites. Use Artif. Satellites Geod., 2, 247–251.

Sievert, T., (2019). GNSS Radio Occultation Inversion Methods and Reflection Observations in the Lower Troposphere. Licentiate dissertation, Karlskrona.

UCAR, Constellation Observing System for Meteorology Ionosphere And Climate,

(2022), [Online]. Available: www.cosmic.ucar.edu [Accessed 25-4-2022].

Urquhart, L., Santos, M. C., Garcia, C. A., Langley, R. and Leandro, R. F., (2014). Global assessment of UNB's online precise point positioning software. Earth on the Edge: Science for a Sustainable Planet, International Association of Geodesy Symposia 139.

Vorob'ev, V. V. and Krasil'nikova, T. G., (1994). Estimation of the accuracy of the atmospheric refractive index recovery from Doppler shift measurements at frequencies used in the NAVSTAR system. Physics of Atmosphere and Ocean, 29, 5, 602–609, 1994.

Wickert, J., Beyerle, G., Konig, R., Heise, S., Grunwaldt, L., Michalak, G., Reigber, C., and Schmidt, T., (2005). GPS radio occultation with CHAMP and GRACE: A first look at a new and promising satellite configuration for global atmospheric sounding, Ann. Geophys., 23, 653–658.

XU, X. and Zou, X., (2020). Estimating GPS radio occultation observation error standard deviations over China using the three-cornered hat method, Royal Meteorological Society (RMetS), 147, 734, 647-659.

Yao, Y., Chang-Yong, H., Bao, Z. and Chao-Qian, X., (2013). A new global zenith tropospheric delay model GZTD. Chin. J. Geophys.-Chin. Ed., 56, 2218–2227.

Yao, Y., Xu, C., Shi, J., Cao, N., Zhang, B. and Yang, J., (2015). ITG: A New Global GNSS Tropospheric Correction Model. Sci Rep 5, 10273, doi: 10.1038/srep10273.

Yue, X., Schreiner, W. S., Hunt, D. C., Rocken, C. and Kuo Y.-H., (2011). Quantitative evaluation of the low Earth orbit satellite based slant total electron content determination. Space Weather, 9, S09001, doi:10.1029/2011SW000687.

Yue, X., Schreiner, W., Kuo, Y., Hunt, D. and Rocken, C., (2013). GNSS Radio Occultation Technique and Space Weather Monitoring. 26th International Technical Meeting of the Satellite Division of the Institute of Navigation, ION, GNSS, 2013, 3.

وكذلك طريقة تحليل البيانات للمقارنة بين قيم التباطؤ الجاف والرطب الناتج من الطرق المختلفة لتعريف الغلاف الجوي ومقارنته مع نتائج تحليل ارصاد النظام العالمي لتحديد الاحداثيات.

الباب الرابع: يتضمن هذا الباب عرض ومناقشة كآفة نتائج الدراسة حيث يتم مناقشة نتائج المقارنة بين ارصاد الطرق المختلفة لتعريف الغلاف الجوي وكذلك نتائج المقارنة بين التباطؤ للطرق المختلفة لتعريف الغلاف الجوي مع بعضها ومع نتائج تحليل ارصاد النظام العالمي لتحديد المواقع واخيرا قيم الثوابت لكل من النموذج الجاف والرطب لحساب التباطؤ في التروبوسفير مع تقييم كل منهم.

الباب الخامس: يتضمن هذا الباب ملخص للبحث وأهم الاستنتاجات المستخلصة من الدراسة ويشتمل كذلك علي بعض التوصيات للدراسات المستقبلية.

هذه الفروق لها تأثير احصائي ملحوظ على الانكسارية. وبدراسة الفروق بالنسبة لمحطات بالونات الارصاد الجوية تبين وجود فروق كبيرة في محطة بنينا وفروق اقل في محطات جامعة جنوب الوادي ومرسى مطروح ومحطة Athalasa وجميع هذه الفروق أيضاً لها تأثير ملحوظ على قيم الانكسارية.

بعد ذلك تم دراسة العلاقة الخطية بين قيم التباطؤ الرأسي لإشارات اقمار النظم العالمية لتحديد المواقع بمكونيها الجاف والرطب ومعاملات الغلاف الجوي والتغيرات الزمانية والمكانية وتبين ان التباطؤ الرأسي الجاف يعتمد على الضغط الجوي والحرارة وتغير خط الطول وتبين أيضا ان التباطؤ الرأسي الرطب يعتمد على الضغط الجوي وضغط بخار الماء والحرارة وتاريخ رصد البيانات. وأخيراً تم عمل نموذج خطي لكل من التباطؤ الرأسي الجاف والرطب مع المعاملات المؤثرة عليهما لزيادة دقة حساب تباطؤ اشارات النظم العالمية لتحديد المواقع في مصر. ووجد ان ثابت النموذج الخطي لحساب التباطؤ الجاف يساوي ٠,٣٦ وقيمة معامل الضغط ٠,٠٠٢ وقيمة معامل خط الطول يساوي -٠,٠٠٢٤ وقيمة معامل درجة الحرارة يساوي -٠,٠٠١٤. ووجد ايضا ان ثابت النموذج الخطي لحساب التباطؤ الرطب يساوي ٤,٦ وقيمة معامل الضغط -٠,٠٠٤ وقيمة معامل ضغط بخار الماء يساوي ٠,٠٠٥ وقيمة معامل درجة الحرارة يساوي -٠,٠٠١٥. وبحساب قيمة الفرق بين قيم التباطؤ الناتجة من النماذج والحقيقية لنسبة ٢٠% من البيانات الغير داخلة في تكوين النماذج وجد ان متوسط قيم الفروق في النموذج الجاف تساوي ١سم وفي الرطب تساوي ٣,٧سم.

محتوى ابواب الرسالة:

تم إعداد هذه الدراسة في خمسة أبواب بالإضافة إلى قائمة المراجع والملخص العربي والإنجليزي:

الباب الاول: وهو عبارة عن مقدمة عامة عن طريقة استتار اقمار النظام العالمي لتحديد المواقع ومقدمة ايضا عن طريقة بالونات الارصاد الجوية ثم تعريف عن النقطة البحثية والمشكلة البحثية واهداف ومنهجية البحث.

الباب الثاني: يستعرض هذا الباب البيانات المستخدمة في الدراسة الحالية وكيفية الحصول عليها والخطوات التفصيلية المستخدمة في معالجه هذه البيانات ويحتوي كذلك على مسح علمي شامل عن الأبحاث السابقة والمتعلقة بموضوع البحث حيث تم ذكر الابحاث السابقة في مقارنة ارصاد طريقة استتار اقمار الملاحة مع ارصاد طريقة بالونات الارصاد الجوية وكذلك عرض سريع للنماذج السابقة في حساب التباطؤ في الغلاف الجوي.

الباب الثالث: يحتوي هذا الباب على طريقة وكيفية تحليل البيانات المستخدمة في البحث للوصول الى اهداف البحث حيث تم عرض منهجية مقارنة ارصاد الطرق المختلفة لتعريف الغلاف الجوي

أقمار النظم العالمية لتحديد المواقع في صورة ملفات بأنواع ومسميات مختلفة بناء على البيانات التي يقدمها كل ملف. الملف المستخدم في البحث الحالي مسمى بـ wetprf ويقدم بيانات طبقة التروبوسفير من ضغط جوي وضغط بخار الماء ودرجة الحرارة وانكسارية الوسط للإشارات بالإضافة الى بيانات اخرى مثل سرعة الرياح وغيرها مضافاً اليها ارتفاع وزاوية خط الطول ودائرة العرض والزمن المرصود فيه هذه البيانات. جميع اقمار الـ LEO المتوفر لها بيانات على الموقع خلال الفترة من ٢٠١٠ الى ٢٠٢٠ والواقعة في مصر وعددهم ١٧ قمر تم استخدامها في البحث الحالي. بالإضافة لهذا فإن جميع اقمار النظام العالمي لتحديد المواقع تم استخدامها في البحث وعددهم ٣٢ قمر. عدد النقاط المستخدمة في البحث هي ١٤٧٠٠ نقطة على الرغم من توفر أكثر من ضعف هذا الرقم على الموقع الا انه تم وضع شروط لقبول البيانات واستخدامها في البحث مثل اكتمال الارصاد على كامل الارتفاعات واكتمالها الى مسافة ٣ كم من سطح الارض وهو ما ادى الى العدد المذكور والذي استخدم فعليا في البحث. والارصاد المستخدمة في البحث موزعة على كامل ايام فترة الدراسة وعلى كامل موقع الدراسة (تغطي كامل القطر المصري). باختلاف وضع اقمار الـ LEO بالنسبة لأقمار النظام العالمي لتحديد المواقع وبالنسبة لموقع منطقة الدراسة يختلف عدد وتوزيع النقاط بمنطقة الدراسة وبناء علية فان عدد النقاط الواقعة في كل يوم من ايام الدراسة يتراوح من ٧ الى ٢٥ نقطة يومياً وموزعة بشكل عشوائي على منطقة الدراسة بناء على وضع الاقمار. تم تحميل ايضا ارصاد محطات بالونات الارصاد الجوية والمتمثلة في بيانات الضغط الجوي ودرجة الحرارة وضغط بخار الماء لمقارنتها بأرصاد طريقة استتار اقمار الانظمة العالمية لتحديد المواقع.

لدراسة تباطؤ اشارات النظام العالمي لتحديد المواقع في طبقة التروبوسفير باستخدام طريقة استتار الاقمار الاصطناعية في مصر، في البداية تمت مقارنة بيانات الغلاف الجوي كالضغط ودرجة الحرارة وضغط بخار الماء وانكسارية الاشارات في طبقة التروبوسفير لطريقة استتار اقمار النظم العالمية لتحديد المواقع بنفس البيانات لطريقة بالونات الارصاد الجوية. المقارنة تمت من خلال طريقتين إحداهما هي مقارنة بيانات رصدة واحدة لكل من الطريقتين وتبين عدم وجود فروق ملحوظة في ارصاد الضغط والحرارة والانكسارية الا انه وجد فروق ملحوظة في ارصاد ضغط بخار الماء وارجعت هذه الفروق الملحوظة الى وجود فروق في الزمان والمكان بين ارصاد الطريقتين. الطريقة الثانية هي دراسة قيم الفروق كمتوسط وانحراف معياري لمجموعة من ارصاد الطريقتين لهما نفس مكان وزمن الرصد. وأشارت نتائج الطريقة الثانية إلى أن قيم الفروق وصلت لـ ٠,٦ ملي بار للضغط الجوي، ٠,٧٩ درجة للحرارة، ٠,١ ملي بار في لضغط بخار الماء، ٠,٤٨ لانكسارية الوسط للإشارات. وعلى الرغم من أن قيم الفروق صغيرة نسبيا الا ان كلها لها تأثير احصائي ملحوظ على الانكسارية.

من ناحية أخرى تمت دراسة الفروق بالنسبة للأقمار منخفضة الارتفاع و تبين وجود فروق كبيرة نسبياً في ارصاد قمر GRACE2 وتبين وجود فروق اقل في اقمار COSMIC3, 6, GRACE1 وتبين ان كل

الملخص العربي

"استخدام ظاهرة استتار أقمار الملاحة العالمية لدراسة التباطؤ في طبقة التروبوسفير في مصر"

الحمد لله رب العالمين، وصل اللهم وسلم على سيدنا محمد وعلى آله وصحبه وأجمعين ،،،،،

تعتبر النظم العالمية لتحديد المواقع (GNSS) أداه هامة وفعالة من حيث الدقة والتكلفة لتحديد الإحداثيات. ومن المعلوم أن الإشارات القادمة من الأقمار الإصطناعية الخاصة بتلك النظم الى المستقبلات الأرضية تتأثر بالعديد من العوامل التي تؤدي الى حدوث أخطاء في حساب إحداثيات النقاط الأرضية، ومن أهم هذه الأخطاء التي لا يمكن حلها بصورة دقيقة هو الخطأ الناتج من طبقة التروبوسفير والمسمى بخطأ التروبوسفير. وتهدف هذه الرسالة إلى دراسة تباطؤ اشارات النظم العالمية لتحديد المواقع في طبقة التروبوسفير باستخدام طريقة استتار الاقمار الاصطناعية.

إن طريقة استخدام موجات الاقمار المستترة هي طريقه حديثه تعطى نموذج كامل عن طبقات الغلاف الجوي بدقه عالية عند النقاط المختلفة من سطح الارض. تتضمن هذه الطريقة استخدام الاقمار الاصطناعية التي اطلقت من مختلف دول العالم وتدور في مدارات منخفضة الارتفاع علي سطح الارض والمسماة بالأقمار الاصطناعية المنخفضة (LEO) والأقمار الاصطناعية المخصصة للنظم العالمية لتحديد المواقع (GNSS) والتي تستخدم في ارسال الاشارات لأجهزة الاستقبال لتحديد مواقع النقاط والزمن بدقة، وبالحصول على بيانات المدارات لكل من النوعين السابقين من الاقمار الاصطناعية وبوجود مستقبل مثبت علي اقمار (LEO) يستقبل الاشارة من اقمار النظم العالمية لتحديد المواقع، يمكن استنتاج مسار تلك الإشارات وتحليلها ومن ثم اسقاط نقاط (الاستتار) على سطح الكرة الارضية (نقطة لكل مسار)، حيث تعتبر هذه النقاط هي اماكن الاستفادة من تلك الطريقة على مدار اليوم ويتم عندها استنتاج معاملات دقيقة للغلاف الجوي ومن ثم نماذج توصيف دقيقة لطبقات الغلاف الجوي المختلفة. كل مجموعة من نقاط الاستتار المتتالية لنفس الاقمار تكون على ارتفاعات مختلفة ومتتالية من سطح الارض وهو ما يقدم بيانات لكامل ارتفاع طبقة التروبوسفير عند نقطة واحدة على الارض تقريبا وهو ما يسمى Radio Occultation Event (ROE).

تتوفر بيانات طريقة استتار الاقمار الاصطناعية على الموقع الالكتروني الخاص بـ University Corporation for Atmospheric Research وهو اتحاد يضم اكثر من ١١٥ كلية وجامعة في الولايات المتحدة الامريكية ويهتم بالبحث في علوم الارض. وتتوافر جميع البيانات الناتجة من تحليل اشارة

جامعة الزقازيق
كلية الهندسة
قسم هندسة التشييد والمرافق

استخدام ظاهرة استتار أقمار الملاحة العالمية لدراسة التباطؤ في طبقة التروبوسفير في مصر

رســـالة مقدمة

للحصول على درجة دكتوراه الفلسفة في العلوم الهندسية

في هندسة التشييد والمرافق

من

المهندس/ إبراهيم فؤاد إبراهيم أحمد

مدرس مساعد بقسم هندسة التشييد والمرافق - كلية الهندسة - جامعة الزقازيق

إشـراف

الأستاذ الدكتور/ جمال صابر الفقى
أستاذ المساحة والجيوديسيا
بقسم هندسة التشييد والمرافق - كلية الهندسة
جامعة الزقازيق

الأستاذ الدكتور/ أشرف القطب موسى
أستاذ المساحة والجيوديسيا بالمعهد
القومي للبحوث الفلكية والجيوفيزيقية
حلوان القاهرة

الدكتور/ محمد أمين عبد الفتاح
مدرس بقسم هندسة التشييد والمرافق - كلية الهندسة
جامعة الزقازيق

2022